Nanomechanical and Nanoelectromechanical Phenomena in 2D-Atomic Crystals: A Scanning Probe Microscopy Approach

Nicholas D. Kay

MPhys: Physics (Lancaster University)

Physics

Department of Physics

Lancaster University

September 2016

A thesis submitted to Lancaster University for the degree of Doctor of Philosophy in the Faculty of Science and Technology

Abstract

In this thesis we probe the morphological, nanomechanical and nanoelectromechanical properties of 2D materials: graphene, MoS_2 and h-BN. Throughout this study we extensively use scanning probe techniques of ultrasonic force microscopy (UFM), direct-contact electrostatic force microscopy (DC-EFM) and heterodyne force microscopy (HFM). With the use of these techniques we report the observation of a Moirè patterns when graphene is aligned on h-BN and propose that the imaging with atomic force microscopy of such a sample is partly due to variance in both sample adhesion and mechanical stiffness. In addition to this we probe the ability for UFM to detect the subsurface mechanical properties in 2D materials and confirm that the anisotropy present effectively enhances the resolution. We apply this knowledge of UFM and 2D materials to detect the decoupling of graphene, grown on $4H$-SiC, from the substrate through the intercalation with hydrogen. In the final part of this thesis we discuss the electromechanical phenomena observable in 2D materials and related devices. Through the electrostatic actuation of graphene resonator-type devices we are able to probe the electrostatic environment beneath the graphene, information that is unavailable to non-contact mode techniques. We then develop this method of DC-EFM to incorporate a sensitivity to the time-dependent properties by introducing the heterodyne mixing principle. This new technique developed, called electrostatic heterodyne force microscopy (E-HFM) is sensitive in the nano-second time domain whilst maintaining the nanoscale lateral and vertical resolution typical of an atomic force microscope. We propose that E-HFM will prove to be a valuable tool in characterising the behaviour of high-frequency small-scale nanoelectromechanical systems

(NEMS) currently beyond the reach of conventional characterisation techniques. Finally we show the future directions of this work where we discuss the use of flexoelectricity in creating NEMS based on h-BN where the behaviour of such devices is currently unknown.

To my family.

Acknowledgements

I would firstly like to thank my family, particularly my parents Michael and Melanie, whose support has been unquestionable not only throughout my PhD but at all times. And to Chrissie for being patient and providing plenty of encouragement.

I owe a lot to my supervisor, Oleg Kolosov and also to Ben Robinson, for all the invaluable help and guidance over the course of my PhD and for allowing me the intellectual freedom to study what I found most interesting.

Thank you to everyone else in the AFM group who I worked with: Alex, Jean, Charalambos, Riccardo, Pete, Claire and Ghazi for many useful discussions and the company in the lab/office.

Declaration

This thesis is my own work and no portion of the work referred to in this thesis has been submitted in support of an application for another degree or qualification at this or any other institute of learning.

'To be is to do'

Socrates.

'To do is to be'

Sartre.

'Do be do be do'

Sinatra.

Contents

List of Figures

List of Tables

Commonly Used Acronyms

- AFM = Atomic Force Microscope
- CVD = Chemcial vapour deposition
- DC-EFM = Direct contact Electrostatic Force Microscopy
- E-HFM = Electrostatic Heterodyne Force Microscopy
- EFM = Electrostatic Force Microscopy
- FFM = Frictional Force Microscopy
- FIB = Focused ion beam
- FIDT = Focused interdigitated transducer
- FMF = Free Molecule Flow
- FMM = Force Modulation Microscopy
- HFM = Heterodyne Force Microscopy
- IDT = Interdigitated transducer
- LP = Linear Polariser
- MEMS = Micro Electromechanical Systems
- MFP = Mean Free Path
- MLG = Multi-Layered Graphene

- NEMS = Nano Electromechanical Systems
- NPBS = Non Polarising Beam-Splitter
- PD = Photodiode
- QFS = Quasi Free-Standing
- RIE = Reactive ion etching
- SAW = Surface acoustic wave
- SPM = Scanning Probe Microscopy
- UFM = Ultrasonic Force Microscopy
- vdW = van der Waals
- WP = Wollaston Prism

List of Symbols

- α_C = Deflection angle of the cantilever from the distributed load acting on the cantilever (deg)
- α_z = Deflection angle of the cantilever from the vertical displacement of the tip (deg)
- α = Deflection angle of the cantilever to external stimulus (deg)
- β = Angle made between the cantilever and the horizontal (deg)
- Γ = Tension present in the beam (N)
- δ = Deflection of the NEMS resonator (m)
- δ_c = Deflection at the end of the cantilever (m)
- ϵ_r = Relative permittivity of a material
- η = Electrostatic force per unit length (Nm^{-1})
- θ = Angle made by the cantilever cone (deg)
- ι = Air molecule diameter (m)
- κ = Clamping coefficient for a doubly-clamped beam, given as 1.03
- λ = Wavelength (m)
- ν_{13} = Interlayer Poisson ratio
- ν_{12} = Poisson ratio in-plane

- Π = Dimensionless parameter defining beam of membrane behaviour
- ρ = Density (kg m^{-}3)
- ω = Angular frequency (rads^{-}1)
- a = Radius of suspended circular membrane (m)
- A = Area (m^{-3})
- C = Capacitance (F)
- d_n = Thickness of optical medium (m)
- E_1 = Elastic modulus in-plane (GPa)
- E_3 = Elastic modulus out-of-plane (GPa)
- F = Load applied (N)
- g = Effective contact radius (nm)
- G_{23} = Shear modulus between layers (GPa)
- h_t = Height of the tip/cone (m)
- h = Thickness of the MLG or 2D material (m)
- I = Area moment of inertia (m^4)
- k = Spring constant of membrane to a distributed load (Nm^{-1})
- k' = Spring constant of membrane to a point load (Nm^{-1})
- k_c = Spring constant of the cantilever (Nm^{-1})
- Kn = Knudsen number
- l = Characteristic length of the NEMS device (m)
- L = Length of suspended region or beam (m)
- m = Mass (kg)

- n = Refractive index
- p = Pressure (Pa)
- Q = Q-factor
- r_n = Relative refraction coefficient
- r = Radial coordinate (m)
- R = 8.31 Gas constant (J mol^{-1} K^{-1})
- t = Time (s)
- T = Temperature (K)
- V_{DC} = DC voltage applied between the back gate and the cantilever (V)
- V_{AC} = AC voltage applied between the back gate and the cantilever (V)
- w = Width of beam or resonator (m)
- z = Coordinate axis normal to the plane of the 2D material sheet (m)

Chapter 1

Introduction

Atomically thin crystals were once thought to be unstable in ambient conditions[1]. Despite this, the structure of graphite has long been known to be hexagonal with weakly bound cleavage planes[2]. However it was not until 1934 that the true van der Waals nature of these bonds in graphite was realised[3] and 1972 for MoS_2[4]. The final step in the realisation of devices from atomic crystals came much later in 2004 with the isolation of a single stable layer of graphite/graphene at the University of Manchester[5]. Here the extremely attractive electrical properties were revealed for the first time, resulting in the award of the 2010 Nobel prize for Physics. The isolation of graphene has since lead to further study of a class of materials coined 'the van der Waals solids', where planes of atomic or a few atomic layers thick are weakly bound through van der Waals (vdW) forces alone. Within this group of vdW solids are materials such as graphene and hexagonal boron nitride (h-BN) and the transition metal dichalcogenides (TMD's), all possessing a plethora of desirable electrical, optical, thermal and mechanical properties. Therefore it is possible to create new devices from this library of materials by stacking them together to form heterostructures, like traditional semiconductor heterostructures but atomically thin by nature.

In the fabrication of traditional semiconductor heterostructures careful attention has be made to the lattice constants in order to either avoid or tailor specifically the strain present in the sample, which is known to affect the electronic behaviour of such devices. Even though heterostructures of 2D materials are not

technically bonded to one another, the structures of any two layers in contact with one another will still affect the properties of the whole device. The clearest example of this is graphene on h-BN. As both of these materials are hexagonal in nature with a small discrepancy in lattice constants, a Moirè pattern is formed, the observation of which has lead to interesting new physics [6, 7, 8, 9]. The size and shape of this pattern depends on the difference in lattice constants of the two materials, the structure of the materials and the rotation with respect to one another. By studying these patterns for perfectly aligned samples we are able to infer information about the local variations in the adhesion at the surface through experimental results. This may have implications in the variation of the electronic properties of devices where graphene is stacked upon an insulating layer of h-BN.

Whilst the advantageous electrical properties of graphene have been realised for a number of years there are still obstacles obstructing the path to commercial success. One of these is the problem of economical high-quality methods of producing graphene. Many attempts have been made through chemical vapour deposition on various substrates with success to varying degrees[10, 11]. The problem however is the transfer from these usually expensive and conductive materials to a substrate for device fabrication. One possible solution is the thermally induced growth of graphene on SiC substrates[12]. Whilst this substrate is still rather expensive it is insulating and can be integrated into conventional wafer processing techniques, unlike CVD substrates. However, the graphene produced is of a much lower quality owing to the chemical bonds still present between the graphene and the substrate. To counter this, researchers have used hydrogen as an intercalation element to effectively remove the bonds between the graphene and the substrate, greatly improving the electrical qualities, closer to that of pristine graphene[13]. In this thesis we probe the mechanical properties of such a system to understand the level of substrate interaction and the mechanical integrity of the graphene. In doing this we find that, whilst the electronic properties are well decoupled from the substrate, there is still a good degree of mechanical support present, an ideal situation for electronic devices. It is also proposed that mechanical contact with the substrate may behave as a heat sink, ideal for high power and high switching rate nanoelectronic devices.

As devices and heterostructures made from 2D materials increase in complexity over time the number of layers involved also usually increases. Some of these devices realised to date such as LED structures are composed of >15 layers[14] giving an overall thickness above 5 nm, however the number of layers one can use is limitless. To improve the performance of these devices it is important to ensure that all surfaces are clean upon deposition and that there are no defects between the layers. One way to assess the quality of the heterostructure is to take a cross-section with a focused ion beam cutter (FIB) and image the layers directly from the side with transmission electron microscopy (TEM)[14], however this involves the destruction of the device and only allows the imaging on a thin cross section. As a way of imaging the mechanical integrity of these heterostructures, and therefore the quality, we propose the use of ultrasonic force microscopy (UFM). UFM is already known for its sensitivity to subsurface defects and objects in traditional semiconductor materials[15, 16, 17]. We therefore study further the role in which the layered nature of 2D materials affects the mechanical properties and therefore the UFM's ability to observe subsurface structures such as voids and cavities in vdW's heterostructures. Through both theoretical and experimental results we show the role of sample anisotropy on the UFM signal. Due to the fact that 2D materials are transversely isotropic (i.e. different in plane and out of plane properties) we see that the stress field beneath the AFM tip is confined almost entirely beneath the tip and reaching far into the sample. This effectively lends 2D materials and their heterostructures to subsurface imaging with UFM and other ultrasonic techniques such as heterodyne force microscopy (HFM). Finally we show that sample flexing is often the dominating feature in UFM stiffness maps and may drown out other signals from nanoparticles buried deep beneath suspended structure.

Whilst much attention is given to the application of graphene in electronic devices there are a wealth of other opportunities in which it may be implemented to great advantage. The use of atomically thin crystals, particularly graphene, in nanoelectromechanical systems (NEMS) is one of these areas that we now turn our attention to. Graphene's extremely high tensile strength[18] coupled with a low density make it an ideal candidate for high sensitivity force/mass sensing. Masses as low as 2.5×10^{-18}g have been detected with graphene beam-like

resonators[19, 20]. There are however certain phenomena of graphene resonators that do not apply to their conventional silicon counterparts, which can be detrimental to their overall performance. Due to the high surface area to mass ratio, the devices fabricated from graphene are prone to adhesion to the surrounding materials through van der Waals interaction. As a result, adhesion of the graphene to the trench or cavity substrate can result in highly non-uniform stress distributions[21] and therefore can be detrimental to the device operation. It is therefore important to be able to study these devices with a high level of spatial resolution. So far a majority of techniques have measured only the averaged properties of the system such as amplitude of vibration, either averaged across the whole device through electrical readout or with optical resolution, limited by the wavelength of light. This presents a problem as devices shrink in size to the hundreds of nm regime where the characterisation difficulty increases vastly with optical techniques. Atomic force microscopy can be used To solve this problem with it's few-nanometre lateral resolution, however only a handful of studies have taken this approach to tackle the problem[21, 22]. The use of AFM to map the performance of MEMS has thus far only be used to either map low-frequency systems, where the cantilever can respond directly to the actuation of the system [22], or high frequency systems where only an average of the high-frequency behaviour has been imaged [21]. As devices decrease in size the characteristic frequency increases, reaching into the GHz region. Therefore it is imperative that the high frequency behaviour is understood, with a resolution reaching down to below the nanosecond regime. For this, current applications of SPM fall somewhat short. In this study we propose a solution where we apply the principle of heterodyne mixing, similar to Heterodyne Force Microscopy (HFM)[23], where the non-linear tip-sample interaction is the mixing element. By using the heterodyne principle and mixing mechanical and electrical actions between the AFM tip and the NEMS we preserve information about the amplitude and phase of the electromechanical phenomena, crucial to detecting time-dependent phenomena. We call this method Electrostatic Heterodyne Force Microscopy (E-HFM). Using E-HFM we demonstrate that it is possible to detect the behaviour of nano electromechanical resonators with a nm spatial resolution, a vertical displacement

resolution of approximately 10 pm and on a time-scale of ns with the potential to probe pico-second regime phenomena in the future.

Whilst AFM has a fantastic vertical resolution, in the region of 10's of pm, this may still not be good enough for probing properties of small resonator-type devices where low-temperature thermal vibrations or even zero-point fluctuations are to be measured. For this, various optical techniques have been applied varying in complexity from a relatively simple 'point and shoot'[24] laser system which makes use of the underlying substrate to create an 'on-chip' interferometer, to systems which make use of near-field optical coupling techniques[25]. The problem with such techniques is that to obtain the best resolution one has to consider the thickness of the flake, the underlying oxide thickness as well as laser noise/mode-hopping and other vibrational noise present in the system. We present an improvement to current techniques through the use of a differential interferometer, previously used to detect small movements on an AFM cantilever[26]. We present a theoretical approach and lay out the steps to study graphene NEMS using this interferometer. We also demonstrate the resolution by measuring the thermal resonant modes in an ambient environment where the resolution was below 1 pm.

In this thesis we first discuss the morphology of 2D materials and their related heterostructures such as graphene on h-BN Moirè patterns. Here we are able to show, through the use of Ultrasonic force microscopy (UFM), that there is both a variation in the mechanical stiffness and adhesion over the period of the Moirè superlattice. We then build on this by studying the way in which ultrasonic probe techniques such as UFM and HFM are able to measure the subsurface properties of samples. From a theoretical analysis backed up with experimental evidence we show that the difference between the in-plane and out of plane mechanical properties of stacked 2D materials effectively enhances both the depth and lateral resolution of such methods. Hereby showing that these methods have a great potential in helping to advance the field of 2D heterstructures. Using this evidence we apply our new knowledge of the UFM contrast in 2D materials to study graphene grown on $4H$-SiC. Here we are able to measure the level of coupling between the graphene and the substrate and how the intercalation with hydrogen is effective in greatly reducing this, a step forward for the large-scale

manufacturing of graphene. Finally we turn our attention to the electromechanical properties of graphene resonator type devices. In this final chapter we are able to measure the level of charge trapping beneath graphene through the detection of the electrostatic actuation of the graphene membrane by use of an AFM probe, allowing us to measure the otherwise hidden and detrimental interactions between the substrate and graphene NEMS. We then advance this method one stage further to incorporate time-dependent processes through the heterodyne mixing principle, building on the high spatial resolution of AFM by adding a nanosecond time-scale resolution and creating a new sub-method called E-HFM. The implications of which allow one to study both the electrostatic properties of the sample whilst measuring the amplitude response and the time-dependent behaviour of such samples. This technique is the only method thus far capable of measuring both the amplitude and temporal responses of NEMS with a 10 nm and <1 ns resolution. This high spatial and temporal resolution may prove invaluable as devices are developed on an ever decreasing scale with extremely high operating frequencies.

Chapter 2

Background

2.1 2D Materials

Since the initial isolation of graphene there have been many successful attempts to observe 2D allotropes of other materials such as boron nitride and MoS_2. As the layers of atoms in these materials are bound weakly to one another through van der Waals interaction it is possible to easily isolate and study them in their own right. Whilst all of these materials form two-dimensional films, and in many cases have similar atomic structures, they exhibit a wide range of behaviours. This wide range of behaviours allow atomic devices to be constructed that are only a few nm thick, here we study the basic properties of the three main vdW solids studied in this thesis; graphene, h-BN and MoS_2.

2.1.1 Graphene

Graphene is a two-dimensional hexagonal structure, formed from the combinations of the s and $p_{x,y}$ orbitals to form a hybrid σ bond between three other carbon atoms leaving the p_z or π orbitals out of plane. It is these out of plane orbitals that form a basis for the electronic and chemical behaviour of graphene. An illustration of these bonds and the stacking structure of graphene is shown in Fig. 2.1

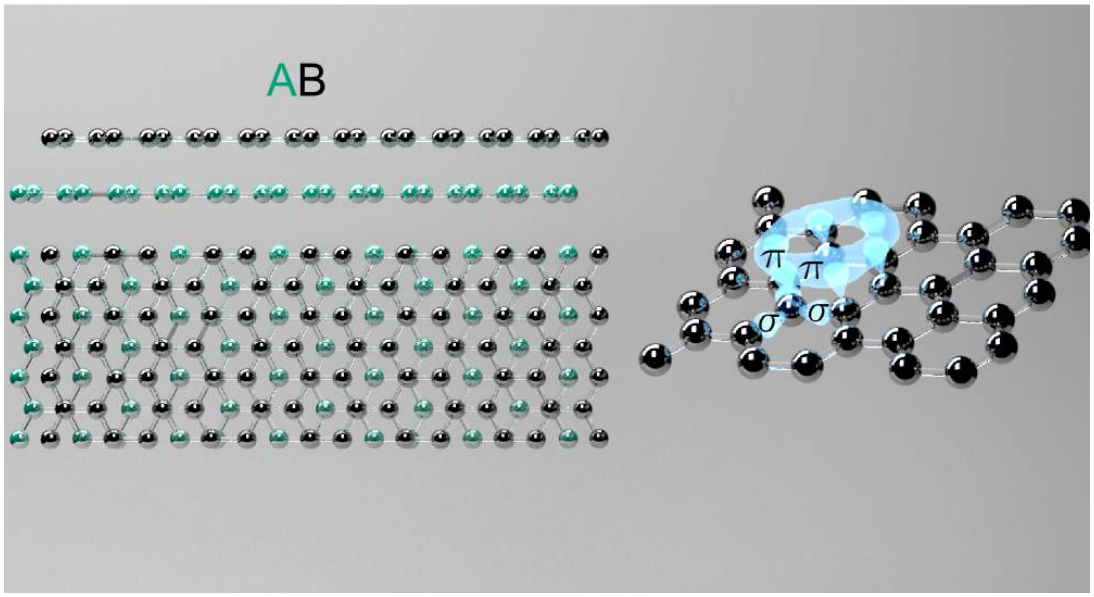

Figure 2.1: The atomic and stacking structure of graphene where the preferred stacking is AB. The nature of the bonds in graphene is also shown where the hybrid, in-plane, σ bonds provide the strength of graphene and the π bonds allow for its great electrical conductivity. We show the bottom layer as light green and the top layer as black to more easily discern the stacking structure.

2.1.1.1 Mechanical Properties

The Young's modulus E of graphene has been determined theoretically [18, 27, 28, 29] and found experimentally [30, 31] to have a value of approximately 1 TPa. There have been other studies that have found the Young's modulus of graphene to be less than the widely accepted value of 1 TPa [32]. However the value presented for E from that case is inferred by fitting experimental data to the expected behaviour of a doubly-clamped beam, where the assumptions made may present a significant source of error.

The Young's modulus of a material, that is its stiffness in the elastic limit, is only one way of characterising its mechanical properties. To understand at what point a material begins plastic deformation one must consider the yield strength. For graphene this has been estimated [33] to be between 80-90 GPa. Beyond the yield strength is the ultimate tensile strength, which is the maximum stress the material can sustain before failure. The ultimate tensile strength for graphene has been calculated to be approximately 120 GPa for a perfect monolayer[33, 34], this translates into roughly 10% of the Young's modulus and is one of the highest ever observed.

2.1.1.2 Optical Properties

Monolayer graphene has been found to absorb 2.3 % of red light [35] and 2.6 % of green light [36], a surprisingly high absorbance for a material which is only one atom thick. The difference in these figures was expected to be due to some experimental uncertainty as the absorbance of graphene depends only on the fine structure constant, i.e. how light interacts with electrons [35]. By increasing the number of graphene layers one adds 2-3 % of to the optical absorption each time. The absorption coefficient has also been found to change depending on the intensity of light incident on graphene. This effect is known as saturable absorption. The threshold for saturable absorption has been measured experimentally and calculated theoretically where a wide range of values have been found. In some experimental studies of monolayer and multilayer graphene the threshold was found to be as low as 0.53 MW/cm^2[37] for 100 fs pulses and as high as 250$\pm$80 MW cm^{-2} [38]. Taking the minimum value of 0.53 MW cm^{-2} for a spot

size of ≈1 μm diameter we see that this translates to a threshold laser power of P_{th}=5.3 mW, above any values of laser power incident on graphene used in our experiments by a factor of approximately 8, therefore saturation is not expected to be an issue. The refractive index for graphene is independent of the wavelength in the visible range, we therefore quote the value for λ=635 nm (RI=2.73-1.35i [39]) as this is the laser wavelength used in this study. Graphite has also been found to exhibit optical birefringence, that is, a difference in the refractive indices in the in-plane and out-of-plane directions [40].

2.1.1.3 Electrical Properties

Graphene is known to be a semi-metal [5], that is the valence and conduction bands touch with no overlap. This point of zero overlap is called the Dirac point and at this point in k-space we see a wealth of interesting and useful physical phenomena. The density of states at the Dirac point is 0 therefore for pristine graphene where there are no sources of doping the Fermi level will sit in this zero density of states region and the conductivity will be extremely low. In practice this is not the case as there is always some source of doping whether it is intentional, e.g. through a back-gate voltage, or accidental, e.g. by interaction with the substrate and any electrostatic charge present. For this reason in our experiments we model graphene as a metal. It should also be noted that due to the linear dispersion, relation electrons and holes in monolayer graphene behave as massless Fermions at the Dirac point thus greatly increasing the electron/hole mobility.

2.1.2 Hexagonal Boron Nitride (h-BN)

Boron nitride has many allotropes just like carbon, including a two-dimensional layered structure similar to graphene called hexagonal boron nitride (h-BN). In this hexagonal formation each nitrogen atom is bonded to 3 other boron atoms and vice versa. However, as with graphene these bonds are purely covalent and the boron-nitrogen bonds form a partly covalent, partly ionic bond [41]. The bond lengths have been measured to be 1.421Å in graphene and 1.446Å in h-BN [42], a

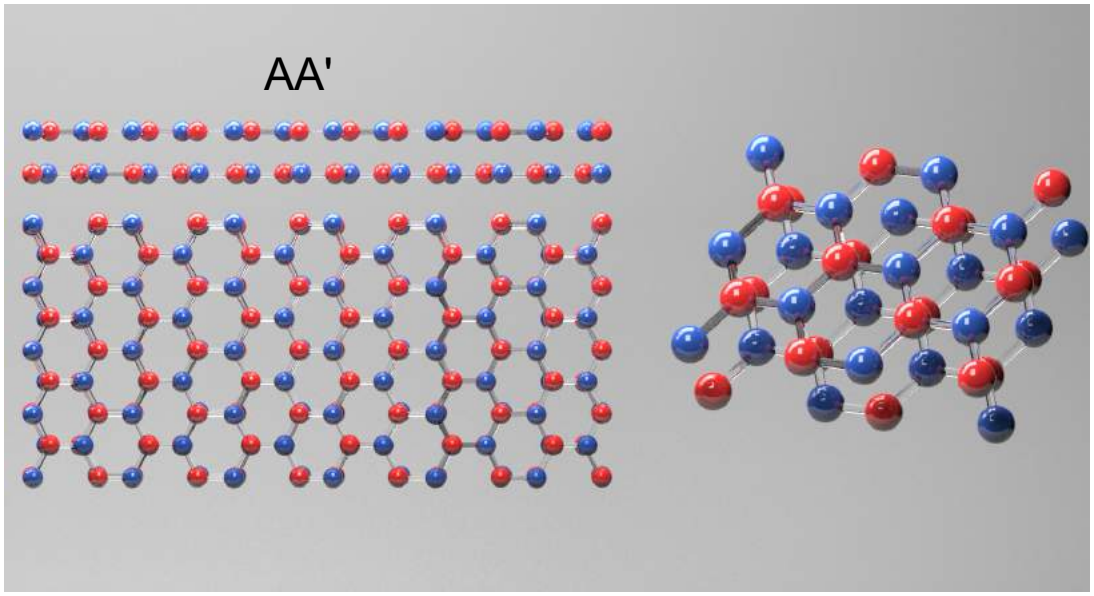

Figure 2.2: The atomic and stacking structure of h-BN. Here we show the most stable stacking structure, AA', where a boron atom sits directly on a nitrogen atom and vice versa.

difference of approximately 1.7 %. This slight discrepancy between the two lattice constants is what leads to the Moirè pattern formation when graphene is aligned on a h-BN substrate, a topic which is discussed in more detail in succeeding sections and 4.2. The most stable form of h-BN is believed to be the AA' [43] stacking which means that each boron has a nitrogen above and below it as can be seen in Fig. 2.2

2.1.2.1 Mechanical Properties

Being of a similar structure to graphene, hexagonal boron nitride also exhibits high mechanical stiffness. The values found for the in-plane elastic modulus of h-BN are 716 GPa[33] and 811 GPa [44], comparable to that of graphene. The Poisson ratio for h-BN was also found to be similar to that of graphene (ν_{h-BN}=0.18[45] and ν_{gr}=0.194[46]). We also quote the yield strength and ultimate tensile strength for monolayer h-BN as 70-85 GPa (estimate)[33] and 88-120 GPa [33, 47] respectively.

Whilst there is much focus on the high in-plane stiffness of graphene and

h-BN it is also worth mentioning the out-of-plane elastic properties. The out-of-plane elastic constants will play a role when the sample is much thicker than a monolayer and beam bending becomes the dominating behaviour, not membrane behaviour (i.e. stretching). The out of plane elastic modulus E_3 for h-BN, again similar to that of graphene, is calculated as E_3=38 GPa[45].

2.1.2.2 Electrical Properties

Whilst graphene is a direct zero-gap semiconductor or semi-metal, h-BN has a large, indirect band-gap of 5.955 eV for indirect excitons and 6.08 eV for single particles[48]. Therefore under most experimental conditions h-BN will be electrically insulating. This insulating behaviour has made h-BN an attractive substrate, encapsulating and dielectric material for graphene and other 2D-material based devices[49, 50, 51].

2.1.2.3 Optical Properties

Whilst there is not a wealth of literature on the refractive index of h-BN perpendicular to the plane, we report several values for n in the visible range, unless otherwise stated, of approximately 2.2[52], 1.91-2.05(λ=110-550μm)[53], 1.22[54] and 1.85[55]. The imaginary part of the refractive index or extinction coefficient k approaches 0 in all of the above studies. Like graphene, h-BN also exhibits some degree of birefringence where the refractive index parallel to the layers: between 2.00-2.16(λ=110-550μm)[53]. In addition to this the refractive index was calculated theoretically in the visible range[54] and was found to vary from 1.22 to approximately 1.5 between the out of plane and in-plane indices.

2.1.3 Molybdenum Disulphide MoS_2

Molybdenum disulphide is a part of the family of van der Waals solids like graphene and h-BN and, like graphene and h-BN, has long been used as a solid lubricant because of these weak interlayer vdW bonds[56]. Whilst MoS2 belongs to the family of vdW solids it also belongs to another sub-group called the transition metal dichalcogenides (TMD's) which take the format of TX_2 where T is a

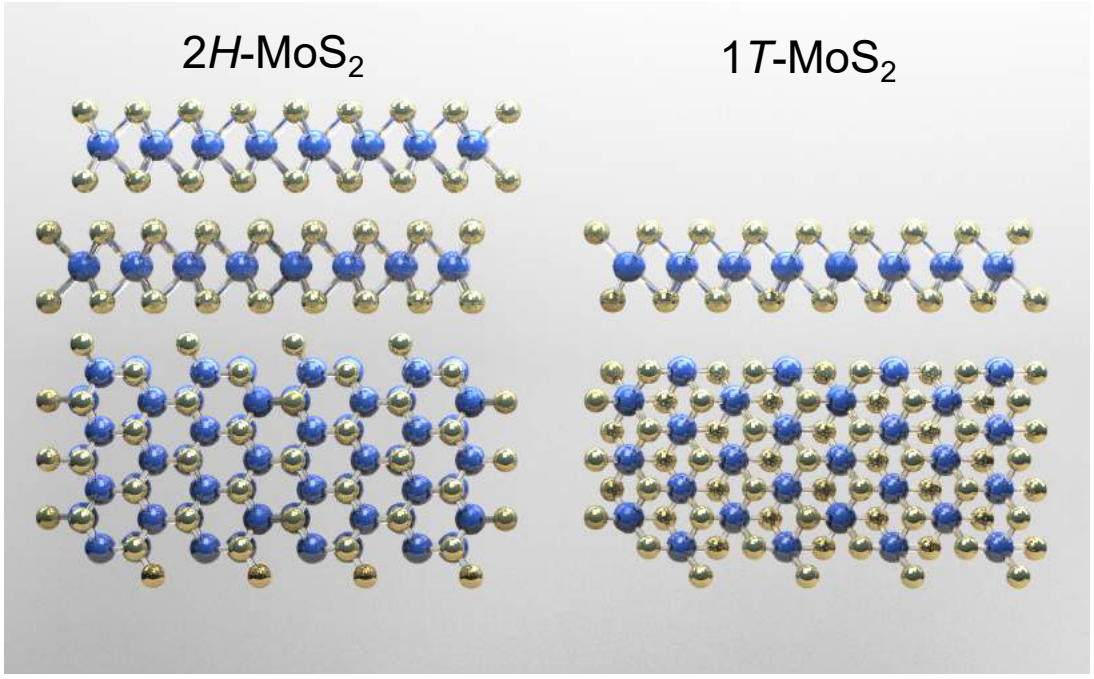

Figure 2.3: The structures of $2H$ and $1T$ MoS_2. The stacking of $2H$ MoS_2 is such that Mo atoms sit only directly above S atoms and vice versa. The stacking of $1T$ has a simple AA stacking so each layer is directly above and below other layers.

transition metal and X is either sulphur, selenium or tellurium. The TMD's are different in that the atoms are not arranged in a purely two-dimensional plane, as a result there are different possible arrangements of the atoms. For MoS_2 there are a number of phases, however we consider two called $1T$ and $2H$ MoS_2, seen in Fig. 2.3. The two exhibit different electrical properties with $1T$ being metallic and $2H$ being a direct-gap semiconductor in monolayer form[57]. The phase of MoS_2 that we shall refer to in the rest of this thesis is the semiconducting phase, $2H$.

2.1.3.1 Mechanical Properties

The in-plane elastic modulus of MoS_2 has been measured experimentally at a value of 330±70 GPa [58], 270±100 [59],210 GPa [60] and calculated theoretically at a range of values from 128.75 GPa [61]. Values reported for the ultimate tensile

strength have been given as an average of 23 GPa or approximately 10%[59]. No data on the yield strength was found in the literature.

Whilst MoS_2 has a relatively high in-plane stifness, although not as high as graphene or h-BN, it also has a much higher out of plane stiffness than either graphene or h-BN, measured at a value of approximately 160 GPa[45]. This is roughly 4 times higher than that of graphene or h-BN and may be due to a higher vdW bonding strength between the layers.

2.1.3.2 Electrical Properties

As mentioned in previous sections $2H$-MoS_2 is a direct band-gap semiconductor as a monolayer but transitions to an indirect gap semiconductor for thicknesses greater than this. The band-gap in the monolayer regime is approximately 1.8 eV[62] and for bulk MoS_2 the indirect band-gap is 1.29 eV[63]

2.1.3.3 Optical Properties

Experimental studies into the value of the refractive index n and the extinction coefficients k of thin MoS_2 have shown that n varies between 5-7 over the visible range whereas the extinction coefficient k varies between 0-3, being higher at shorter wavelength and approaching 0 for red light [64]. Therefore to model the optical properties of MoS_2 the refractive index will need to be considered as wavelength dependent.

2.1.4 Optical Visibility of 2D Materials

Whilst only an atom or a few atoms thick, the class of 2D materials are surprisingly easy to identify with optical microscopy, even with the naked eye for large flakes. One trick to increase the optical contrast of these atomic layers is through using a specific thickness of substrate on which the flake is to be placed. By selecting a thickness of SiO_2 on top of Si such that the conditions for inteference of the incoming light are affected most by the additional path length provided by the 2D material, the optical contrast can be maximised.

There have been several studies on the affects of substrate on the optical visibility of graphene and other 2D materials, varying in complexity [64, 65, 66, 67, 68]. The simplest treatment that describes the visibility of graphene and other 2D materials on an Si/SiO_2 substrate is through analysing the Fresnel interference from a beam of light incident on the graphene and normal to the surface. This approach was first performed by H. Anders[69]. The Fresnel interference approach assumes light incident normal to the plane so that light reflected will be along the same path.

The equation produced by H. Anders[69] is shown below to give the portion of light reflected from an SiO_2/Si substrate

$$r_{SiO_2}e^{i\epsilon_{SiO_2}} = \frac{r_4 + r_3e^{-i\Delta_2}}{1 + r_4r_3e^{-i\Delta_2}} \tag{2.1}$$

Where r_4=$(n_0 - n_1)/(n_0 + n_1)$ is the relative refraction constant between air (n_0) and SiO_2 (n_2). Here r_3 is the relative refraction between the SiO_2 and the silicon beneath. The symbol $\Delta_n = 4\pi n_n d_n/\lambda$ represents the additional path the beam takes passing through a medium with refractive index n and back. Here λ is the wavelength of light used and d_n is the thickness of the medium.

To calculate the portion of reflected light for the case of SiO_2 on Si, as Eq. 2.1, with the addition of a thin layer of additional material, such as graphene or other 2D material, the equation becomes rather more complex. However through a clever technique devised by both [70] and [71], seemingly independently, one can use the case of a 3 layer system such as Eq. 2.1 to deduce the case for a 4-layer system. Whilst this derivation is rather long we quote the result also presented in [69]

$$r_{gr}e^{i\epsilon_{gr}} = \frac{r_1 + r_2e^{-i\Delta_1} + r_3e^{-i(\Delta_1+\Delta_2)} - r_1r_2r_3e^{-i\Delta_2}}{1 + r_1r_2e^{-i\Delta_1} + r_2r_3e^{-i\Delta_2} + r_1r_3e^{-i(\Delta_2+\Delta_1)}} \tag{2.2}$$

Where r_1 and r_2 are the reflection coefficients for the air/graphene and graphene/SiO_2 interfaces respectively. To calculate the contrast C we use Eq's 2.1 and 2.2 in the following way similar to [68]

$$C = \frac{\left|r_{SiO_2}e^{i\epsilon_{SiO_2}}\right|^2 - \left|r_{gr}e^{i\epsilon_{gr}}\right|^2}{\left|r_{SiO_2}e^{i\epsilon_{SiO_2}}\right|^2} \tag{2.3}$$

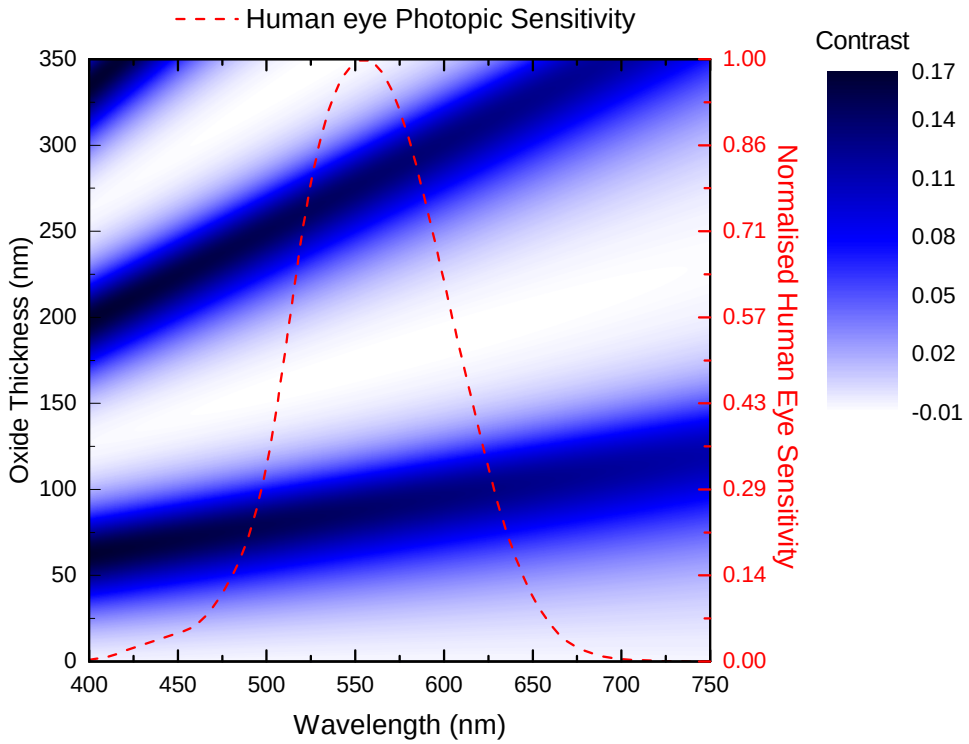

Figure 2.4: The optical contrast of graphene on an Si/SiO_2 substrate as a function of the incident wavelength of light and the oxide thickness. The optical contrast is not seen to increase above 18 %. On top of this plot we show the typical photopic sensitivity of the human eye in well-lit conditions which was taken from CIE (International Commission on Illumination) $V_M(\lambda)$ [72, 73] with the corresponding y-axis shown in red.

By plotting Eq. 2.3 for varying λ and oxide thickness d_2 we obtain the results shown in Fig. 2.4

We we see that for oxide thicknesses of approximately 90 and 290 nm we see the largest contrast in the green wavelength region. Therefore we pick 290 nm oxide thicknesses throughout this thesis due to their commercial availability. For the implementation of Eq. 2.1 and 2.2 we use the wavelength dependant refractive indices for Si and SiO_2, the refractive index of graphene is not dependant on wavelength and only depends on the fine structure constant for this we use a refractive index of $2.73\text{-}1.35i$ [39]. Including the extinction coefficient for graphene

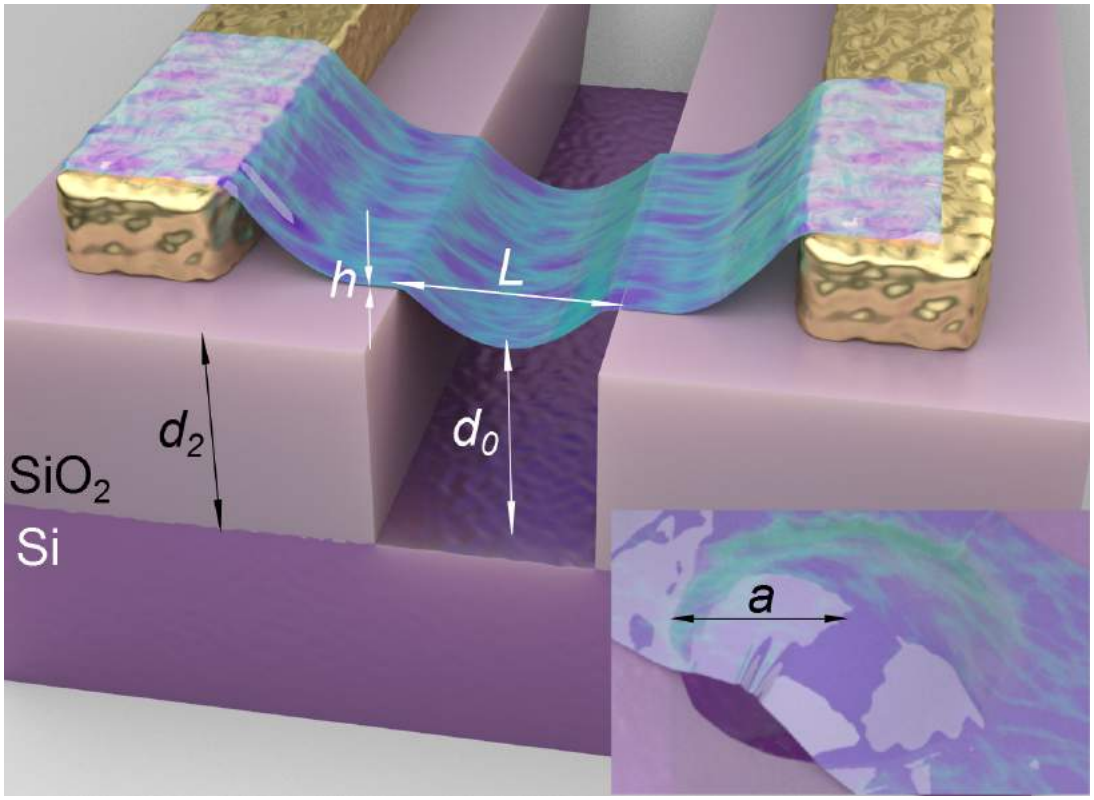

Figure 2.5: The variables used in the characterisation of both a beam-like resonator and a drum-resonator (shown inset). Where L is the length of the suspended region, h the material thickness, d_2 the oxide layer thickness, d_0 the gap between the 2D material and the substrate and a the radius of a drum-type resonator.

and silicon ensures that we account for any absorption of the materials.

2.2 Nanoelectromechanical Systems (NEMS) from Graphene and other 2D materials

In this section we discuss some of the NEMS fabricated from graphene and other 2D materials in literature. We focus exclusively on the literature around resonator-type devices studying both operating characteristics of such devices and the techniques used in understanding them.

2.2.1 Electrostatic Actuation of Graphene Resonator Devices

Throughout this work we are primarily interested in developing methods to study the behaviour of NEMS resonators based on 2D materials. To do this we need to be able to, with a good degree of accuracy, ascertain properties of the resonators such as amplitude, resonant frequency and the effects of damping on the resonators. To be able to do this we give a theoretical basis with which one can compare any experimental results for validation.

To understand firstly the amplitude response of a resonator we start with the case of a doubly-clamped beam. The formula for the deflection at the centre of such a system is given below

$$\delta = \frac{\eta L^4}{384EI} \tag{2.4}$$

Where η is the force per unit length, L the length of the beam, E the Young's modulus and $I = wh^3/12$ is the area moment of inertia with respect to the direction in which the beam is suspended, w and h are the width and thickness of the beam. The electrostatic distributed load, η, can be approximated by considering the case of a parallel plate capacitor [24] and taking the derivative with respect to the distance between the plates

$$\eta = \frac{F}{L} = \frac{1}{2L}\frac{\partial C}{\partial z}V^2 \tag{2.5}$$

Where combining Eq's 2.4 & 2.5 we obtain the following formula for the amplitude of vibration of a doubly clamped beam subjected to a uniform electrostatic load

$$\delta = \frac{\epsilon_0 \epsilon_r L^4 V^2}{32Eh^3 d_2^2} \tag{2.6}$$

Where ϵ_r is the relative permittivity of the material between the beam and the back-gate and d_2 is the distance between the beam and the back-gate (modelled as the oxide layer thickness). The approximation of the distance between the graphene and the back-gate being equal to the oxide thickness d_2 is valid for

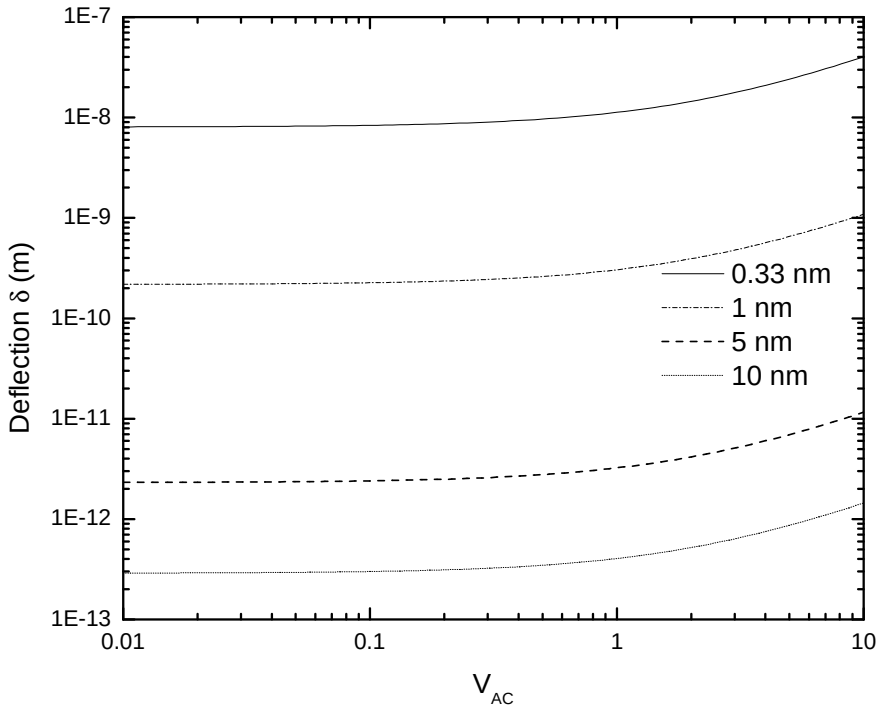

Figure 2.6: The amplitude at the centre of the resonator for varying thicknesses of graphene (E=1.153 TPa [46]) shown as a function of the applied V_{AC} voltage where the following resonator values are used: L=300 nm, ϵ_r=1, V_{DC}=5 V, d_2=290 nm.

thick materials however for much thinner material, such as a monolayer, it is important to incorporate the sagging into the trench of the monolayer which was found to be as much as 100 nm. To obtain an approximation of the amplitudes we implement Eq. 2.6 for the specific case shown in Fig. 2.6.

Fig. 2.6 shows the peak amplitude of the resonator type devices detailed. To understand how this matches with the proposed methods of measuring the electrostatic actuation with an AFM, we quote the typical noise floor for vertical measurements of around 10 pm.

While we also wish to map the amplitude response of resonator type devices we also wish to understand how the resonant frequency behaves. For this we use the following formula to approximate the resonant frequency of a doubly-clamped

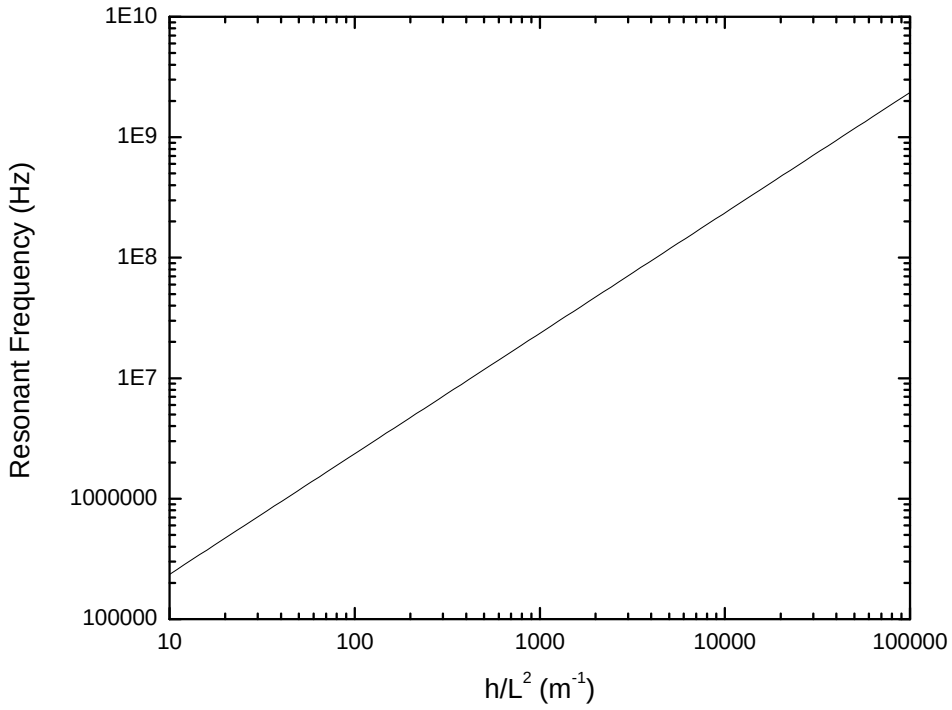

Figure 2.7: The resonance frequency for a doubly clamped beam of graphene/MLG (E=1.153 TPa [46], ρ=2200 kg/m^3 [75]) as a function of h/L^2 assuming no tension.

beam given by [24]

$$f_0 = \left(\kappa \left(\frac{E}{\rho}\right)^{1/2} \frac{h}{L^2}\right)^2 + A^2 0.57 \frac{\Gamma}{\rho L^2 w h} \tag{2.7}$$

Where κ is the clamping coefficient and is shown to be 1.03 for a beam clamped on both ends [74] and Γ is the tension present in the beam. We then plot the resonant frequency of such a system as a function of h/L^2 (assuming Γ=0) shown in Fig. 2.7

The Eq. 2.7, holds for materials where bending is the primary mechanism. This is not always the case as for thin materials and devices driven at high amplitude membrane behaviour may become more dominant i.e. stretching.

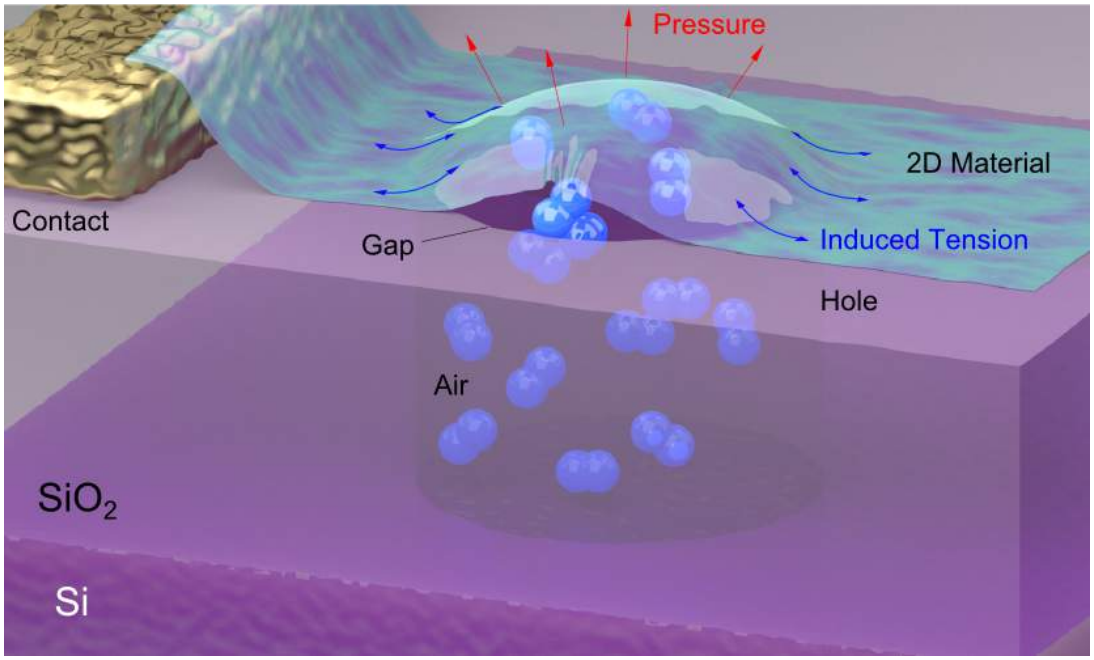

Figure 2.8: Illustration of some of the mechanisms present when depositing a device over a hole and operating under vacuum. If the device is fabricated under atmospheric pressure then this pressure will act to increase the tension in the suspended material at low outside pressure. This is seen as an increase in the resonant frequency. Additionally we show that devices with small gaps allow air to enter or escape the otherwise covered hole as described in the main text.

2.2.2 Damping Mechanisms Present in 2D NEMS

The first and most obvious damping mechanism present in not only graphene and 2D NEMS but all MEMS is damping due to the air in the ambient environment. Firstly, and while not strictly a damping mechanism, it was observed that if a resonator is deposited over a hole in the substrate under ambient conditions and then studied in vacuum, an increase in the resonant frequency is seen. This has been observed experimentally [76] where the excess pressure of the air in turn induces tension on the beam resulting in an upwards shift in the resonant frequency. In the same study Lee *et al* distinguish between two damping mechanisms. The first regime, for the devices used in the study [76], is for pressures over approximately 60 Torr. This damping regime is called free molecule flow (FMF) damping and the Q-factor has a characteristic $1/p$ dependence as can be seen below [77]

$$Q_{FMF} = \frac{\rho h \omega_0}{4} \left(\frac{\pi RT}{2m} \right)^{1/2} \frac{1}{p} \tag{2.8}$$

Where ρ is the density, R is the gas constant 8.31 J mol^{-1} K^{-1}, T temperature, m the mass of the air molecule, h the thickness of the beam and ω_0 the angular resonant frequency of the resonator. The physical mechanism for FMF damping is through the collision between the resonator and the molecules present in the atmosphere.

Whilst not strictly a damping mechanism it was also reported that on devices where there was a partial covering of the hole to make an incomplete drum there was an additional tension present in the device [76]. This scenario only occurred where the mean-free path (MFP) of the air was larger than the opening in the partially covered drum, thereby not allowing air molecules to enter the cavity at a rate that could be seen over the course of the experiment. Upon an increase in pressure and thus decrease in MFP the pressure was able to equilibrate, removing any tension in the beam caused by the pressure difference.

A topic discussed in the context of traditional beam-like resonators is the effect of viscous damping [78, 79, 80]. One figure of merit to understand whether viscous damping has a significant effect on a device's performance is through the Knudsen number given below

$$Kn = \frac{\lambda_{MFP}}{l} = \frac{k_B T}{\sqrt{2}\pi \iota^2 p l} \tag{2.9}$$

Where ι is the air molecule diameter and l the characteristic length of the device. Various values for the value of Kn at which viscous damping becomes important have been given: $Kn < 0.1$ [79] and $Kn < 0.01$[81].

There are several other damping effects which are special to the case of graphene resonators. One of the main effects observed is the effect of the van der Waals forces on the morphology of the resonator devices. It has been proposed [82, 83] that graphene and similar carbon nanotubes can effectively adhere to the side walls of the trench etched into the substrate through vdW forces giving an induced tension in the device and therefore an increase in the resonant frequency.

2.2.3 Beam-Membrane Mechanical Transition in 2D Materials

In the study of resonator type devices there are, broadly, two regimes of mechanical behaviour which are exhibited by devices. The first of these two regimes is beam bending which is associated with compression along one surface and extension along the opposite, i.e. a bending moment is set up. This mechanism depends on a wide range of the mechanical properties of the material such as shear modulus G and out-of-plane elastic modulus E_3 amongst others. The second mechanism is membrane behaviour whereby stretching in-plane of the material contributes to the overall response of the system. For graphene, with an extremely high in-plane elastic modulus but a relatively low out-of-plane stiffness we expect membrane behaviour to dominate, especially for relatively thin samples. To understand whether we expect beam or membrane behaviour to dominate the stiffness characteristics of our resonators we employ the parameter Π shown in Eq. 2.10 [84]. This equation describes the behaviour of a material suspended over a hole.

$$\Pi = [12(1-\nu^2)]^{3/2}\left(\frac{Fa^2}{Eh^4}\right) \tag{2.10}$$

Where ν is the Poisson ratio, E the elastic modulus, F the applied load, a the radius of the suspended material and h the film thickness. We implement Eq. 2.10 and use the values Π given[84] to determine the various regimes.

The graph in Fig. 2.9 shows that for low loads the graphene resonator will be either be in the plate regime however for higher loads applied to the centre we see a departure from plate behaviour to that of a beam/membrane.

2.2.4 Characterisation of NEMS based on 2D Materials

2.2.4.1 Optical Readout Techniques

For typical graphene resonators suspended over either a trench or a hole etched into an SiO_2 substrate it is possible to use a simple setup where two lasers are used, one for the actuation, another for detection. The laser light incident on the

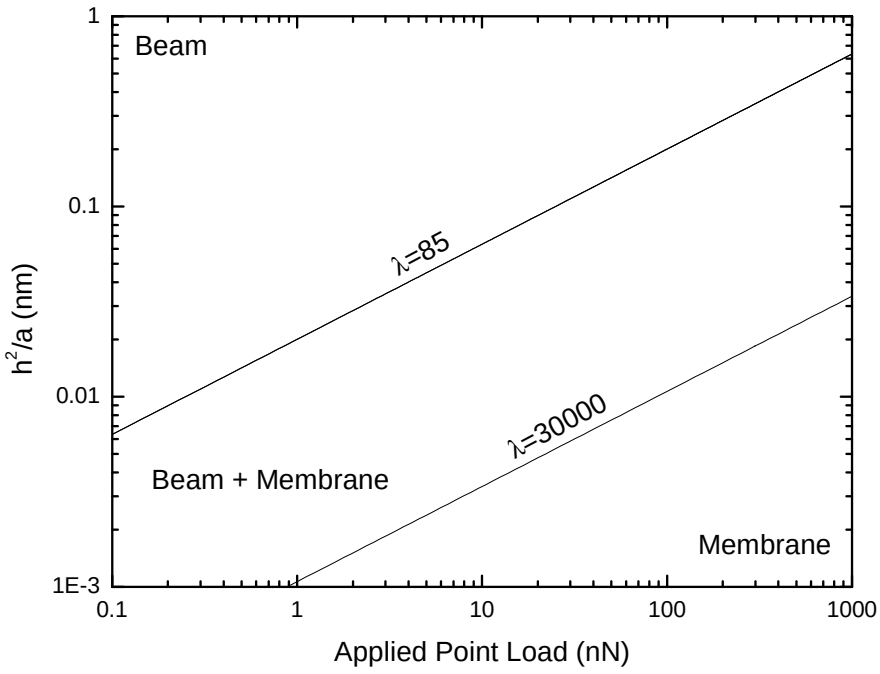

Figure 2.9: We show the three main regions of behaviour for a graphene resonator: beam, membrane and a mixture of the two. The regions shown hold for a circular arrangement of suspended graphene/MLG (E=1.15 TPa, ν=0.194) clamped at the edges with an applied load at the centre

sample, as discussed in earlier sections, undergoes interference when reflected from the underlying Si/SiO_2, where the total intensity of the light output depends on the position of the suspended graphene or 2D material. This is a setup adopted in various studies of graphene NEMS [24, 82, 85, 86, 87] and MoS_2 NEMS [50, 76, 88]. The only study to explicitly state the sensitivity of the measurement system found values in the range of 30.2-243.1 fm/$Hz^{1/2}$ [50], these values depnded greatly on the devices themselves. For the study [50] a He-Ne laser (λ=632.8 nm) is incident on the MoS_2 resonator.

There have also been various theoretical analysis of the optical detection of metallized NEMS[89] where near-field effects are considered, showing a shot-noise limited detection down to 7 fm/$Hz^{1/2}$ with the use of a Michelson interferometer. Near-field effects become dominant where the width of the resonator beam is of the order of the wavelength of light and diffraction around the edges of the beam plays a non-negligable role.

In other studies that use near-field effects for the optical detection of graphene NEMS [25], sensitivities of 260 fm/$Hz^{1/2}$ have been reported. In this study evanescent waves, which couple to a graphene resonator, are measured by placing a glass microsphere in close proximity to the device whilst laser light passes nearby. The resolution of this system was found to be limited by the Q factor of the microsphere used, with large room for improvement reported .

Optical readout techniques predominantly make use of a laser as the primary sensing method. This has issues in that lasers provide noise in both the amplitude of the output beam and also the phase. There is also mode-hopping where temperature changes can result in quick variations in the wavelength. With optical interferometers there can also be a great deal of noise associated with the drift of one arm with respect to the other.

Another issue that is considered in studies [24, 50] is the heating of the device due to the focused laser beam incident on it. For this it has been shown that for laser powers of <0.6 mW (λ=632.8 nm) there was negligible heating of isolated MoS_2 resonators [50]. The effect of the laser heating is however thought to be greatly dependent on both the flake thickness and also whether the flake is contacted electronically as this will provide a cooling channel.

2.2.4.2 SPM Based Measurements of Resonator-Type Devices

One of the primary downsides for the techniques of optical and electrical readout is that the one is limited in the lateral resolution with which one can probe the characteristics of the devices. With optical one is held back by the diffraction limited laser spot size, meaning that devices much smaller than the wavelength will be both subjected to near-field effects along with a greatly diminished signal. For the electrical readout one can sense the actuation of extremely small devices but again a lateral resolution is not available. To combat this limit of resolution for both optical and electrical techniques, attention has been turned to the use of scanning probe microscopy. With a lateral resolution of a few nm, depending on tip size, one should be able to probe the spatial properties and functions of even the smallest NEMS.

The direct application of SPM to high-frequency graphene resonators was performed by Garcia-Sanchez *et.al* [21]. In this particular study a contact mode cantilever is scanned across the surface of the resonator-type devices. During the scanning the graphene is actuated via external electrodes at high frequency. As the resonant frequency of the contact mode cantilever is typically of the order of 10 kHz, much lower than the resonant frequency of the graphene NEMS, the cantilever becomes inertially stiffened and is not sensitive to the individual vibrations. To overcome this Garcia-Sanchez *et al.* apply a sinusoidal modulation signal to the resonator at a much lower frequency. It is then possible to extract the amplitude of this envelope signal and thus the amplitude of the resonator. One additional trick used in this study is to tune the modulation frequency to that of the contact resonance of the cantilever, with the idea that the increase in amplitude will provide a much greater signal. One downside to this approach may lie in the use of the cantilever's contact resonance. If the Q-factor is high then any change in the contact resonant frequency, through a change in the sample stiffness, will result in a shift-along the resonance curve and a sharp decrease in the measured amplitude which would not be representative of the sample motion.

One additional drawback to this technique is the difficulty of implementation, as NEMS often require operation in a vacuum, preferably at low temperature to obtain the best performance characteristics. This is difficult for all but the most

sophisticated AFM systems. However despite this Garcia-Sanchez *et al.* managed to image graphene NEMS in ambient conditions and extract high-resolution maps for the vibrational amplitude of the devices studied. From this they were able to deduce different eigen modes of the resonator beams as well as uncover that the amplitude distribution was highly irregular and depended greatly on the local stresses within the beam. It was also found that a new set of eigen modes where the amplitude was greatest at the edges of the device, rather than the centre, were present. Whilst this method is able to measure the high frequency amplitude maps of graphene NEMS it is not possible to measure the high frequency time-dependant phenomena which would be necessary for measuring the response time of such devices.

In another study by Rivas *et al.* [22] an atomic force microscope is used to map the amplitude response of traditional tuning forks manufactured from $LiNbO_3$ with resonant frequencies in the 50-60 kHz range. In this particular study the AFM was operated in contact mode with cantilevers with a high resonant frequency 70-300 kHz, higher than that of the MEMS devices studied. In this case there is no need for any modulation techniques to overcome the high-frequency detection barrier so the case is rather more simple. In this study the effect of the cantilever on the resonant amplitude of the device was studied, with loads of up to 1.5 μN applied to the surface of the MEMS device. Only small changes in the amplitude response were seen. It should be noted that the dynamic stiffness of the piezoelectric tuning fork used in this case is comparable to that of the cantilever so the effects should be minimal. This is not the case as with previous studies using graphene based NEMS and MEMS [21] where the inertia of the graphene NEMS is negligable compared to that of the tip and is much more likely to be affected by its presence.

2.2.4.3 Electrical Readout Techniques

NEMS are designed to be used in conventional Si wafer processing techniques for integration into electronic circuits. For this reason it is important to understand how one can measure the behaviour of such devices electronically. To measure the response of the system electronically the suspended graphene resonator is used

to form a capacitor with the back-gate electrode whereby the capacitance varies as the graphene vibrates. To do this there are usually two RF signals applied to the sample which differ by Δf. This plays on the fact that the conductance of graphene changes at high frequency so effectively acts as a non-linear mixer which will allow one to detect the properties of the system at the much lower frequency Δf[90, 91, 92].

One problem with the electrical readout technique is that it becomes extremely difficult to quantify, for example the amplitude of vibration, as the rate of change of the conductance as a function of the gate voltage must be known. The cut-off frequency for such a system is rather higher than those of current optical or AFM techniques due to the nature of the down-mixing of the frequencies and is limited to approximately 1 GHz in current setups [92]. The limiting factor in such a case comes from the capacitance between the gold contacts and the underlying silicon.

2.3 Investigating Sample Electrical and Mechanical Properties with SPM

Throughout this work we use extensively a variety of scanning probe methods (SPM) therefore we shall introduce some of the less commonly used techniques. The three techniques we are introducing are mainly involved in the mechanical characterisation of materials and devices, each has it's merits and drawbacks.

2.3.1 Cantilever Dynamics

To understand how the behaviour of the cantilever changes in response to particular outside influences such as tip-surface interaction, especially at higher frequencies, it is necessary to use a continuum model. For this we typically use the Euler-Bernoulli beam theory. To determine the dynamic properties of a beam using this model will employ the time-dependant model given below

$$\frac{\partial^2}{\partial x^2}\left(EI\frac{\partial^2 w}{\partial x^2}\right) = -\mu\frac{\partial^2 w}{\partial t^2} + q(x) \tag{2.11}$$

Where E is the Young's modulus, I the second moment of area, $w(x,t)$ denotes the displacement of the beam at position x along the beam, $q(x)$ denotes the distributed load on the cantilever and μ is the mass per unit length.

One particular mechanism that is of interest is the contact-resonance of a cantilever, this is the shift in resonant frequency upon contact or intermittent-contact with the sample. By studying the response of the cantilever to varying levels of tip-surface interaction it was found that higher forces translate to an increase in the resonant frequency of the cantilever[93]. In the same study it was found that higher resonant frequencies of the cantilever are much less sensitive to the tip-surface interaction, i.e. the force applied.

2.3.2 Mechanical Techniques

2.3.2.1 Force Modulation Microscopy (FMM)

Force modulation microscopy is performed whilst the AFM tip is in constant contact with the surface [94]. Then either the tip or the sample is vibrated at a frequency of typically 2-3 kHz. The reason for this frequency range is two-fold. Firstly the motion of the cantilever must be fast enough such that the feedback of the AFM is too slow to try and compensate; secondly the frequency should be lower than the contact resonance of the cantilever, this is so that the response to the material stiffness is unaffected by the cantilever resonance dynamics.

As FMM relies on the cantilever to cause an indentation to or flexing of the sample, the sensitivity of the system is limited to a range of stiffness' close to that of the cantilever. It is therefore only useful for relatively compliant samples. To extract quantitative data from FMM one can use a simplified two-spring model, where one spring is the cantilever with stiffness k_c and the other the sample with stiffness k_s, to derive an expression as seen in Eq. 2.12

$$k_s = k_c \frac{V_s}{V_h - V_s} \tag{2.12}$$

Where V_h and V_s are the FMM signals on a hard surface and the area of interest respectively. It is suggested that V_h be taken on a surface that is significantly

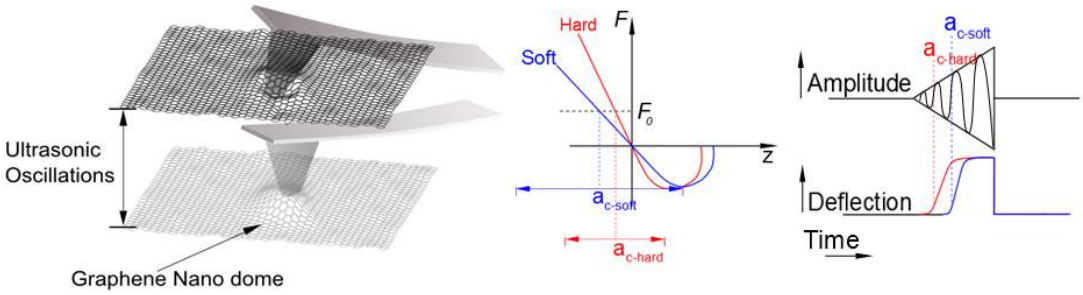

Figure 2.10: Operation of UFM shown where ultrasonic vibrations cause the force on the cantilever to vary according to the van der Waals interaction. Softer materials require a larger vibration amplitude as shown in the difference in a_{c-soft} and a_{c-hard}. The piezo amplitude is modulated with a triangular waveform, seen on the right hand side allowing the location of the amplitude at which the ultrasonic deflection occurs to be found. This appears as a sudden increase in the deflection of the cantilever at the modulation frequency, something that is relatively easy to detect.

stiffer than the cantilever such as the substrate itself in order to obtain the most accurate results.

2.3.2.2 Ultrasonic Force Microscopy (UFM)

Where FMM is unable to provide the stiffness sensitivity required, usually for stiffer samples, we use ultrasonic force microscopy as its high frequency nature allows the imaging of much stiffer materials. Ultrasonic force microscopy was invented by Kolosov and Yamanaka [15] and is an adaptation of scanning acoustic microscopy [95]. UFM allows one to probe the tip-surface interaction and therefore is affected by such properties as tip-sample adhesion and the sample stiffness. The implementation of UFM involves the application of high frequency vibrations typically 2-100 MHz [96] and is implemented by oscillating the sample or the tip (called waveguide UFM [96, 97]) with a piezoelectric transducer.

As is demonstrated in Fig. 2.10 the vibration frequency applied to the piezo is on the order of MHz whilst we apply an envelope function with a frequency of a few kHz typically. The purpose of this is to vary the piezo amplitude to find the point at which the non-linearity is reached, the additional deflection produced by the non-linear region is then present in the deflection of the cantilever at the

modulation frequency.

As UFM works at frequencies much higher than the typical resonance of a contact mode cantilever, the tip does not have time to react to the vibrations applied to it. Therefore the cantilever can be thought of as being inertially stiffened. Using a point mass attached to a spring approximation, the effective spring constant of the cantilever is given by $k_c^* = m\omega^2$, which for a frequency of 4 MHz gives a stiffness of $k_c^* \approx 10,000$ N/m. This increased stiffness effectively causes the tip to indent into the sample. One may think that this would cause damage to anything but the most robust materials however during the modulation cycle contact is broken between the sample and the tip periodically thousands of times. This removes any torsional forces on the cantilever and greatly reduces the damage done to the sample.

On a final note ultrasonic force microscopy can be thought of as a near-field technique as the wavelength of the elastic waves in the sample is at best, $\lambda \approx 500\mu$m, clearly too large to map nanoscale structures.

Whilst UFM has the capability to discern between areas of high stiffness it is, due to difficulties with establishing contact area, difficult to quantify these results. Dinelli *et al.* proposed a method by which the effective contact stiffness S_{eff} can be inferred [98]

$$S_{eff}(F) = \frac{F_2 - F_1}{a_2 - a_1} \tag{2.13}$$

Where F denotes the static force applied by the tip to the sample and a represents the amplitude at which the jump-in or additional ultrasonic deflection occurs. Subscripts 1 and 2 denote the values at two different static forces applied by the AFM tip to the surface. The image in Fig. 2.11 shows the UFM signal as a function of sample vibration amplitude.

The piezo amplitude at which the onset of the ultrasonic deflection occurs can be found through the use of an oscilloscope however it is necessary to be able to convert the applied voltage at the piezo into an amplitude, typically in nm. Whilst one can characterise the sample motion relatively easily using such techniques as laser interferometry it has been found that the piezo amplitude varies measurably over the scale of 100 μm on the sample [99], leading to possibly inaccurate results.

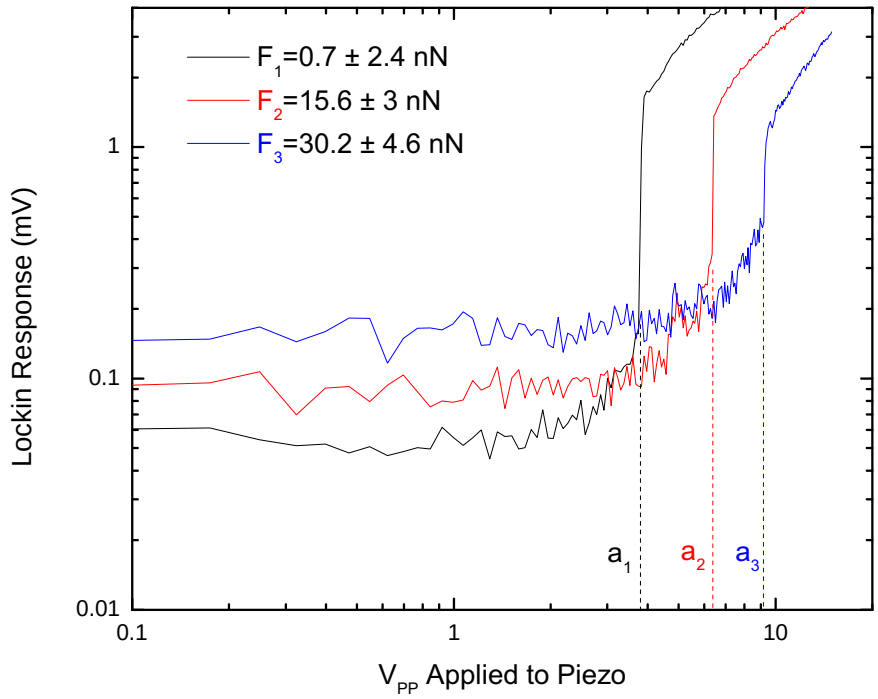

Figure 2.11: The piezo amplitude at which the additional deflection is achieved is indicated by symbols $a_{1,2,3}$ which correspond to the three difference forces applied $F_{1,2,3}$.

To counteract this it was found that by increasing the amplitude of the sample vibrations to much higher than the jump-in amplitude the rate of increase of the piezo amplitude was equal to the increase in ultrasonic deflection[100]. From here the increase in the lockin amplifier response (given in r.m.s) can be converted to nm through the deflection sensitivity of the AFM/cantilever combined system. For a more detailed discussion on this see section B.2 in the appendix.

2.3.3 Electrical Techniques

Whilst mechanical SPM techniques are useful in ascertaining the properties of NEMS they can only provide us with one half of the story. The other half, how the NEMS interacts with its surroundings electrically, must be probed with additional SPM techniques. Here we discuss the basics behind the main techniques used for electrical characterisation.

2.3.3.1 Electrostatic Forces Acting on a Conductive Probe

When a bias is applied between two conductive materials an electrostatic charge builds up on both materials. The amount of charge that accumulates depends on the capacitance of the system and the bias applied. This build up of charge in turn causes an electrostatic force to act between the two pieces. Considering the specific case where we have two materials, one a conductive cantilever and another a silicon back gate, which can be considered conductive, we model the forces present by considering two identical parallel metallic plates given as

$$F = -\frac{\epsilon_0 V^2 A}{2(h_t + d_2)^2} \tag{2.14}$$

Where V is the DC bias between the plates, A is the surface area of the metallic plates and $h_t + d_2$ is the separation between the two plates given as the sum of the tip height and the oxide layer thickness.

Whilst the model of the conductive cantilever biased with a Si back-gate is similar to the above mentioned case it is not completely accurate. For the case of a conductive AFM probe, the cantilever itself is not perpendicular to the sample and therefore the end close to the tip will contribute more. In addition to this

there are contributions to the total capacitance from the cone, tip apex and the cantilever holder. Therefore to accurately describe the behaviour of the system it is necessary to consider these contributions as is shown below [101] where F_{cl} was derived by [102]

$$F_{tip} = -\epsilon_0 \epsilon_r \pi R_t^2 V^2 \left(\frac{1 - \sin\theta}{d_2(d_2 + R_t(1 - \sin\theta))} \right) \tag{2.15}$$

$$F_{cone} = -\frac{\epsilon_0 \epsilon_r \pi V^2}{(\ln(\tan(\theta/2)))^2} \left(\ln\left(\frac{d_2 + h_t}{d_2 + R_t(1-\sin\theta)} \right) + \left(d_2 + R_t - \frac{R_t}{\tan\theta} \right) \left(\frac{1}{d_2 + h_t} - \frac{1}{d_2 + R_t(1-\sin\theta)} \right) \right) \tag{2.16}$$

$$F_{cl} = -\frac{\epsilon_0 w V^2}{2} \left(\left(\frac{\cos\beta}{\tan\beta} \right) \left(\frac{1}{(h_t + d_2)\cos\beta + L\sin\beta} - \frac{1}{(h_t + d_2)\cos\beta} \right) \right) \tag{2.17}$$

Where R_t is the tip radius, d_2 the separation between the tip and conducting plane given here as the oxide thickness, h_t the height of the tip/cone, θ the angle of the cone. The symbol β is the angle the cantilever makes to the surface, L and w are the length and the width of the cantilever.

From Fig. 2.12 we can see that for the case where the tip is positioned on an SiO_2/Si sample (300 nm oxide) the tip forces are extremely small and below the sensitivity of the system for even the most compliant of cantilevers. However the forces acting on the cone and the cantilever beam itself are detectable. If the sample is in contact with the insulating substrate then forces acting on the tip/cone only act to increase the force between the sample and the tip but will contribute little to the overall deflection of the cantilever.

2.3.3.2 Electrostatic Force Microscopy

Electrostatic force microscopy is a term given to the family of scanning probe methods which detect properties of materials such as charge density, work function and surface potential with nanoscale resolution. The basic operating principle of the family of EFM techniques is to apply an AC+DC bias between the conductive probe and the sample. The principles of which are illustrated in Fig.

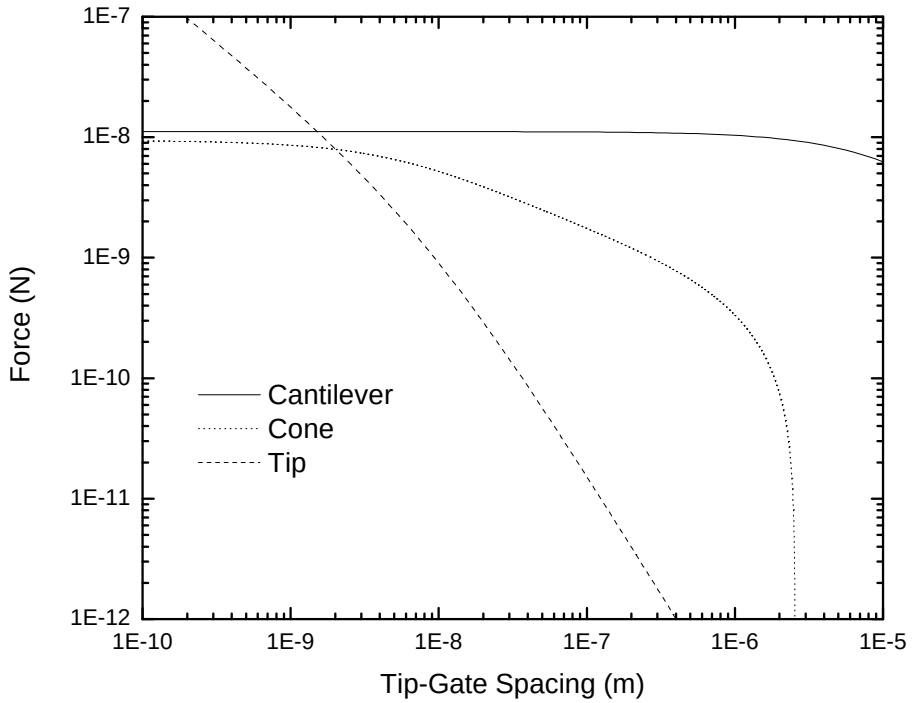

Figure 2.12: The calculated forces acting on the tip, cone and cantilever as a function of the separation between the tip and the conducting sample. Values used are R_t=10 nm, L=500 μm, w=50 μm, V= 15 V, β=0.262 rad, θ=0.175 rad and h_t=15 μm.

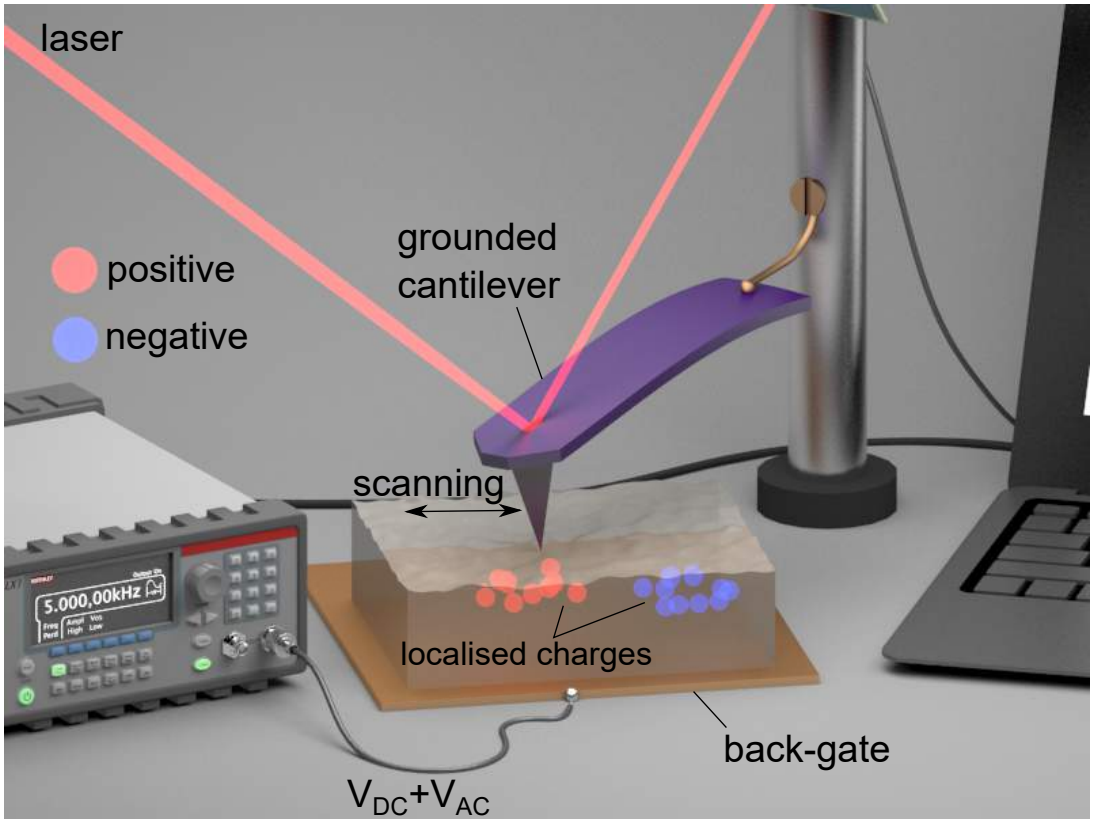

Figure 2.13: Diagram of the basic operating principles of EFM and similar techniques. An AC+DC bias is applied between the tip and sample. Varying V_{DC} can be used to counteract local changes in surface charge density for example such as the difference between areas with a positive and negative charge. By changing the DC voltage during the scan so that no net force is seen by the cantilever and monitoring the applied DC voltage once can build a map of the local electrostatic environment.

2.13 where by a conductive AFM probe is scanned over a sample with a varying local electrostatic environment, such as trapped charges. The charges will act on the conductive cantilever electro statically, this is felt as an increase in the vibration amplitude. By using a feedback loop we are able to apply a DC voltage to counteract this.

To understand the principles behind EFM and how DC voltages and electric fields are measurable at a certain frequency it is necessary to consider the back-gate and the cantilever as a capacitor. Whilst we have previously considered, in greater detail, the electrostatic forces between tip/cone/cantilever and the sample

it is necessary to understand the dependence on the frequency of the system. For this we consider the more general form of the force dependence given in Eq. 2.18

$$F = \frac{1}{2}\frac{\partial C}{\partial z}V^2 \tag{2.18}$$

Where the capacitance of the system is given by C, which is partially differentiated in the direction normal to the plates z. V denotes the potential difference between the plates. For the case of EFM one applies a DC+AC voltage between the cantilever and sample. There are however other sources of potential difference present which will depend on the sample measured such as the contact potential difference V_{CPD} and any voltage V_{SC} coming from a static charge on the surface of the material. Therefore the total voltage $V = (V_{DC} + V_{CPD} + V_{SC} + V_{AC}\sin(\omega t))$ should be input into Eq. 2.18 and the resultant equation can then be split into three components: the DC component, force at ω and 2ω given in Eq's 2.19, 2.20 and 2.21

$$F_{DC} = \frac{1}{2}\frac{\partial C}{\partial z}((V_{DC} + V_{CPD} + V_{SC})^2 + V_{AC}^2/2) \tag{2.19}$$

$$F_{\omega} = \frac{\partial C}{\partial z}(V_{DC} + V_{CPD} + V_{SC})V_{AC}\sin(\omega t) \tag{2.20}$$

$$F_{2\omega} = -\frac{1}{4}\frac{\partial C}{\partial z}V_{AC}^2\cos(2\omega t) \tag{2.21}$$

Typically EFM monitors F_{ω} for imaging however, some systems make use of $F_{2\omega}$ to measure the capacitive coupling to the sample [103]. Usually a corrective voltage is applied between the tip and the sample with the aid of a feedback loop. This effectively removes the electrostatic forces acting on the cantilever providing a feedback signal to achieve zero electromechanical actuation, thus determining the zero total voltage.

2.3.3.3 Contact Electrostatic Force Microscopy

Whilst EFM and KPFM are conventionally non-contact mode techniques there have been efforts made to develop a contact method of electrostatic force mi-

croscopy [104, 105]. The purpose for this development is two-fold, firstly to obtain the maximum resolution of electrostatic fields on the sample and secondly to remove the coupling between topography and electrostatic interaction with the tip. However by choosing the contact regime for electrostatic force microscopy one also needs to take into account the effect of sample compliance.

2.3.4 Time-resolved Techniques

In order to resolve time-dependant properties with an atomic force microscope one has a few options. Firstly, the direct signal from the photo-diode can be measured in real-time. One such example would be the mechanical response time of a resonator to an applied voltage. This could conventionally be done using an oscilloscope or other such device and would be an adequate solution for low frequency systems < 100 kHz. However as one progresses to higher frequency devices there are certain barriers that need to be overcome. Firstly the photodiode in the AFM has a limited bandwidth this may be in the region of a few MHz or a few tens of MHz if it is biased. As the frequency of device operation increases beyond this we start to see effects of wire capacitance in effectively filtering out the measured signal as well as unwanted inductance.

In dealing with high frequency signals one of the techniques commonly used in RF electronics is the principle of heterodyning. This is the phenomena where a fixed oscillator at frequency ω_1 is mixed through some non-linear interaction with the signal to be measured at ω_2. Through this non-linear interaction we obtain two additional frequencies at $\omega_3 = \omega_1 \pm \omega_2$ where if ω_1 and ω_2 are chosen to be similar then one of the ω_3 will be of a suitably low frequency and will not suffer any of the effects of bandwidth limitation or the difficulty associated with detecting high frequency signals.

2.3.4.1 Heterodyne Force Microscopy (HFM)

Heterodyne force microscopy was first implemented [23] as a means of detecting the dynamic mechanical properties of materials such as visco-elastic behaviour.

By using the heterodyne principle it is possible to measure the dynamic mechanical properties of a material at high frequencies, well above those accessible to conventional SPM techniques.

HFM works by oscillating the tip and sample at two slightly dissimilar frequencies, usually in the MHz regime. Then by using the non-linear tip-surface interaction as the mixer, the two frequencies are combined. This can be demonstrated by approximating the tip-surface interaction as [23]

$$F_{ts} = kz_0 - \chi z_0^2 \tag{2.22}$$

Where $z_0(t)$ denotes the distance between tip and sample and can be thought of as the difference of the tip and sample vibrations $z_0(t) = z_t(t) - z_s(t)$ and

$$z_t(t) = A_t \sin(\omega_t t) \tag{2.23}$$

$$z_s(t) = A_s \sin(\omega_s t + \omega_s \tau) \tag{2.24}$$

where ω represents the angular frequency and $\omega_s\tau$ denotes the phase attributed to the dynamic mechanical phenomena on the sample surface, with τ being the characteristic timescale of the phenomena such as the stress relaxation in a visco-elastic material. Inserting Eq's 2.24 and 2.23 into 2.22 we obtain the DC and low frequency terms acting on the cantilever

$$F = \chi[\frac{1}{2}(A_t^2 + A_s^2) - A_s A_t \cos(t(\omega_t - \omega_s) - \omega_s \tau)] \tag{2.25}$$

From Eq. 2.25 it can be seen that the action at the difference frequency has preserved the phase which came from the dynamic phenomena at high frequency ($\omega_s\tau$); this, combined with a known vibration amplitude of the tip, also known as the local oscillator, allows one to preserve the amplitude and phase of the response at high frequency to a more manageable lower frequency. It is important to understand the difference between the beating and mixing effects as is illustrated in Fig. 2.14.

In Fig. 2.14 we see that for a detection system limited in speed to below 1/period of the beating the total signal detected will be 0, this is not the case for mixing. Given this information one would assume that beating does not play a

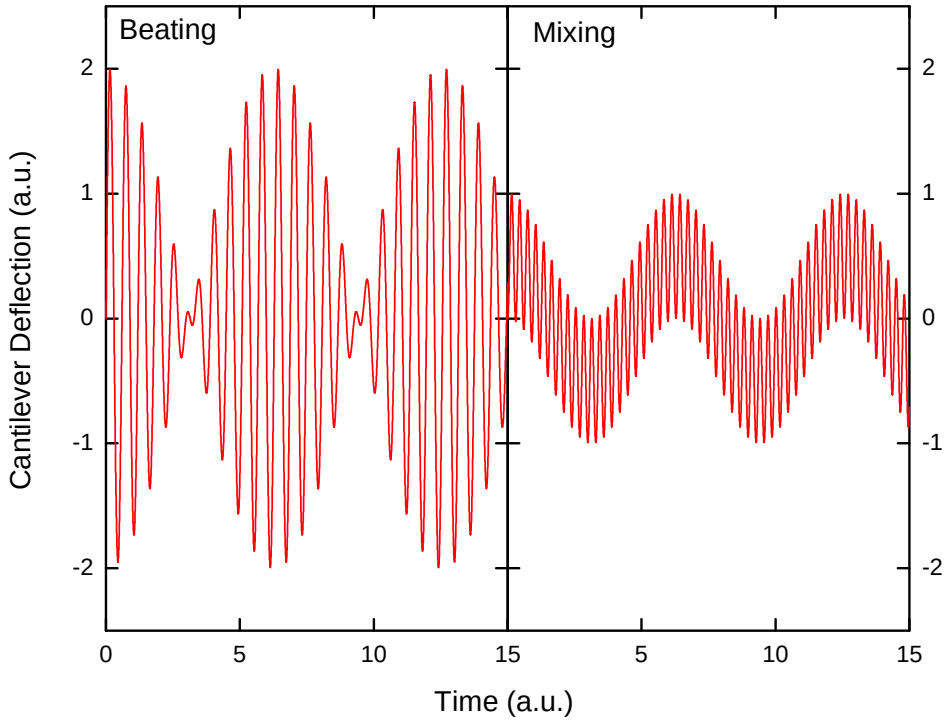

Figure 2.14: The difference between beating and mixing is demonstrated where the beating signal is the sum of two Sine waves ($S_1 + S_2$) differing in frequency whereas the mixing is the multiplication of the same two Sine waves ($S_1 S_2$).

role in HFM however it has been shown that beating does in fact play a certain role in image contrast [106]. This is due to the real motion of the cantilever provided by the beating signal and how this feeds back into the tip-surface interaction providing an additional force. This was found to be the case for all but quadratic tip-sample interactions[106].

As all of the mixing is taking place at the tip-surface point-contact there is no need for a fast detection system to be present in the AFM. The limiting factor for this is usually the response time of the photo-diode so, provided the mixed frequency is less than this, detection should not be an issue. By monitoring the phase of the heterodyne signal one can see any changes in the dynamic response of the sample.

Whilst not a widely used technique there have been sufficient studies into the mechanisms behind the contrast in HFM. Initially it was thought that, along with ultrasonic force microscopy (UFM), Rayleigh scattering was responsible for the nanoscale contrast in UFM and HFM[107]. This was later analysed quantitatively and it was found that Rayleigh scattering was several orders of magnitude smaller than was observed experimentally [108] and was not the main cause of the contrast. In addition, it was proposed that the contrast mechanism depended on the sample type where for nanoparticles embedded in a polymer substrate the contrast was due to energy lost through the friction of the nanoparticle with the surroundings. For much stiffer samples the proposed mechanism was through a variation in the sample stiffness[108] making both HFM and UFM near-field techniques.

2.3.4.2 Electrostatic Heterodyne Force Microscopy (Non-Contact)

In the preceding section we have discussed the method of HFM whereby the tip and sample are vibrated mechanically through a piezo actuator, providing information on the time-dependant properties of the sample. There is however much interest in studying time-dependant electrostatic properties in micro/nano electronic devices, to do this the piezo actuators have been replaced with high frequency electric fields[109, 110]. In these studies the cantilever is however not in contact with the surface and the non-linear electrostatic interaction is used as

the mixer in-place of the tip-surface interaction. The spacing between the tip and the sample in both cases was 100 nm[110] and 500 nm[109].

Chapter 3

Materials and Methods

3.1 2D Materials Preparation

3.1.1 Substrate Preparation and Interaction

Throughout a majority of this work the substrate used is a Silicon wafer with a 300 nm thermal Oxide layer grown on top. The reason for the use of an oxide layer of a specific thickness is highlighted in previous work [66, 67, 68] where the oxide thickness can be selected to provide optimal interference and therefore increase the optical contrast of the flake. For this reason a majority of devices and flakes are produced on an Si/SiO_2 substrate.

To clean the substrate prior to the deposition of graphene, Acetone and IPA baths are used in an ultrasonic bath to remove contamination. In addition to this the sample is cleaned with an $Ar/O_2(2\%)$ plasma, further removing organic contamination.

Whilst adhesion to the substrate is desired for the purposes of exfoliation it may also introduce unwanted substrate interaction, usually in the form of charge transfer [111, 112] which leads to the doping of graphene. Other environmental factors also affect the electrical properties of graphene such as moisture and oxygen [113]. Moisture has been found to increase the irreversibility of the doping produced by oxygen [113] therefore it is necessary to remove it. This is typically

done through thermal annealing in vacuum [114].

3.1.2 Building Heterostructures; an All-dry Transfer of 2D Materials

Whilst the individual properties of the 2D materials are relatively well understood, the next challenge is to understand how these materials behave when they are stacked together to form practical devices. To do this we use an all-dry stamping method [115]. This method provides the advantage that the 2D materials are not subjected to a harsh chemical environment, which can sometimes be involved when etching away the substrate beneath deposited flakes. The principle behind this method is that the 2D material of choice is subjected to exfoliation in the traditional manner except this time it is deposited on a thin gel film. The gel film used in this case is Gel-pak® PF-4X film (0.5 mm thickness). Once the material has been transferred from the tape to the film it is then carefully transferred to a glass window as shown in Fig. 3.1b where care is taken to ensure that there are no delaminations or dirt trapped beneath.

Once the 2D material of choice has been deposited onto the film and positioned on the glass window shown in Fig. 3.1b it must be positioned above the sample. This can be done with the use of the XYZ manipulator. It is also necessary to adjust the tilt of the sample such that it is as close to parallel as possible with the gel-film. This alignment is performed by shining a laser through the glass plate onto the reflective substrate. The reflected beams are both then incident on a beam-splitter. If the beams from the glass and substrate are aligned on top of one another then the plate and sample are parallel, if not then appropriate adjustments can be made with the sample tip-tilt stage.

Once the system has been aligned, a long working distance lens, either 10x or 50x, is used to locate the flakes deposited onto the Gel-pak®. It is important to note that as there is no oxide layer present to aid in the optical contrast of the flake it is very difficult to identify monolayer flakes by eye. Instead, a CCD camera is used as the contrast provided is greatly improved.

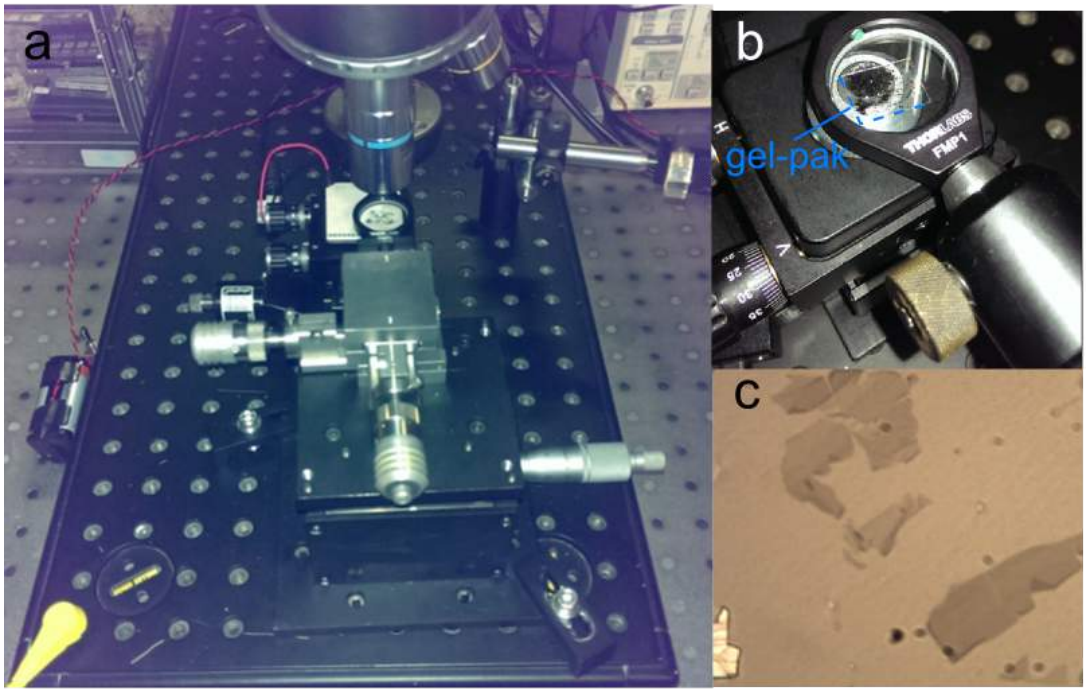

Figure 3.1: Image a) shows the apparatus for the transfer of 2D materials complete with XYZ manipulators and tip-tilt stages. Image in b) shows the glass window complete with Gel-pak® film positioned above the sample stage ready for deposition outlined in dashed blue, Image c) is a view through 50x long working distance lens (LWD) lens of multi-layer graphene.

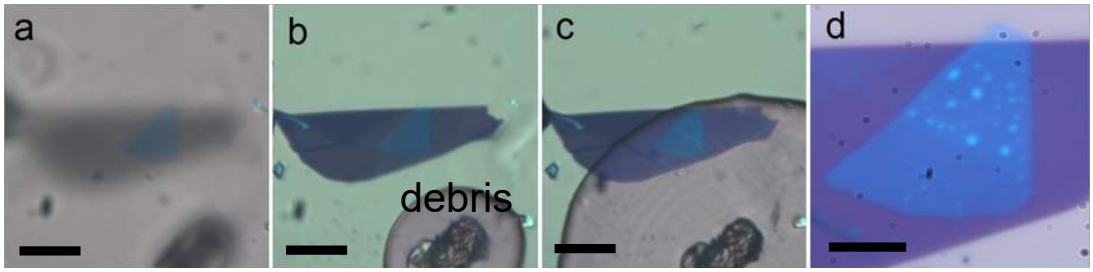

Figure 3.2: The deposition process of a thick multi-layer graphene flake onto multi-layer h-BN. Image a) shows the h-BN (blue) on the substrate whilst the few-layer graphene on the film is shown blurred. As the graphene is brought into contact the contrast change is observed b) showing that good contact is made with the substrate, also showing a piece of debris which prevents the gel-pak contacting the surface at that point. Slowly removing the Gel-Pak® leaves the graphene adhered to the substrate and h-BN c). Image d) shows a 50x image of the resulting structure. Scale bar is 30 μm in a-c and 10 μm in d.

With a desired flake identified, the gel-film is brought closer to the sample such that it is possible to identify the flake and the area of the substrate on which the 2D-material is to be deposited. From here the sample can be rotated or moved in the XY plane to align the two. To deposit the flake the gel-film is brought into contact with the sample. When this happens an easily observable change in the contrast is seen as shown in Fig. 3.2. Once pressed fully into contact with the sample, the visco-elastic stamp is slowly peeled away revealing the material deposited on top.

Once the flake has been deposited the sample can be removed or additional layers of 2D-materials can be deposited. It is also worth noting that for devices where a high level of purity is required it may be necessary to clean the layers prior to deposition. This can be done with aforementioned cleaning methods or by using an AFM in contact mode as an effective 'nano-broom' [116]. As an example of some of the most basic devices created using this method we show below graphene of varying thickness deposited upon h-BN, see Fig. 3.3

3.1.3 Sample Degradation and Oxidation

The stability of the transition metal dichalcogenides has been studied theoretically with density functional theory (DFT) [117]. In this study the room-

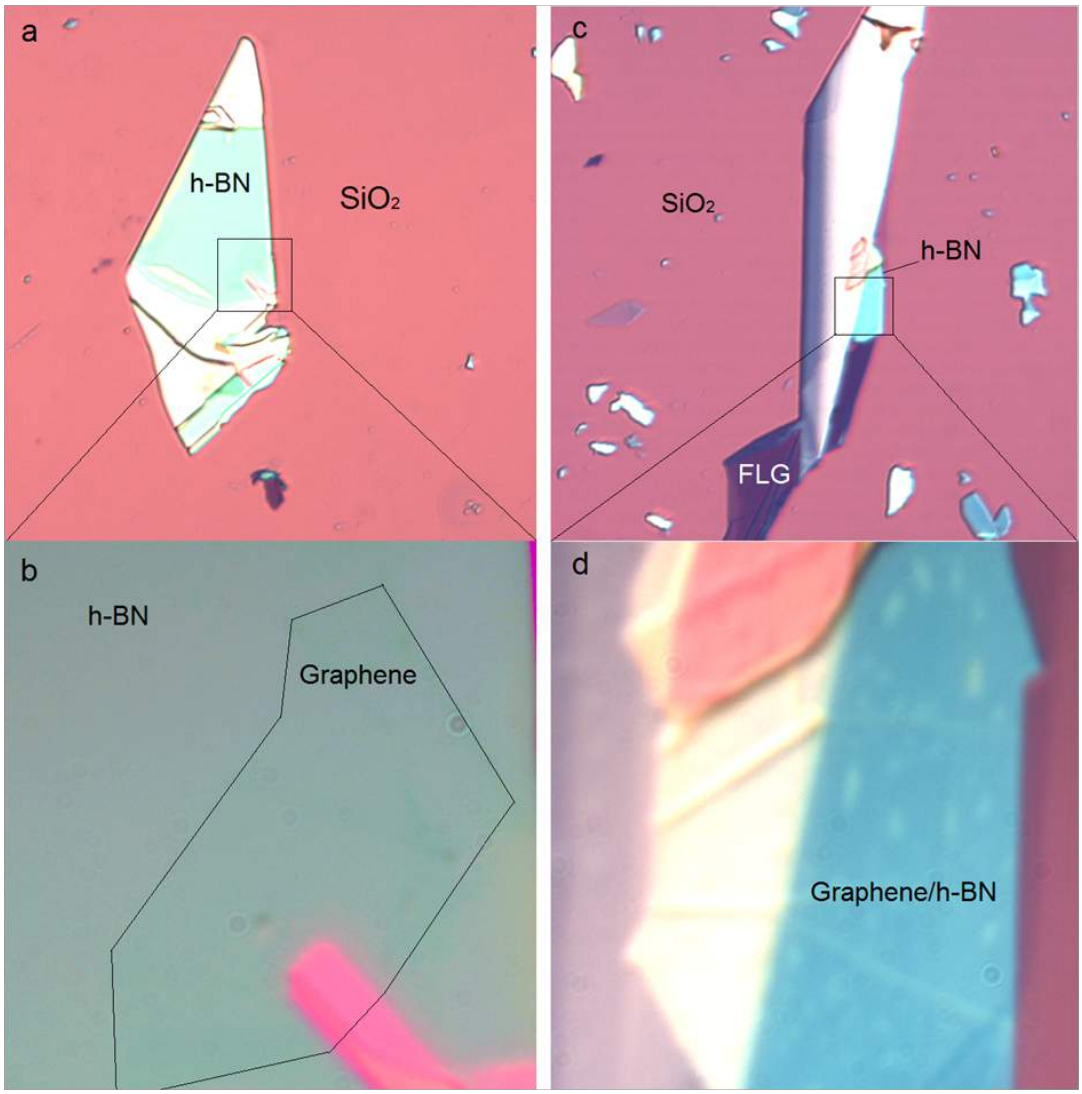

Figure 3.3: Image a) shows a thick piece of h-BN deposited on SiO_2 displayed under 10x magnification , b) shows a close view under 100x magnification revealing a monolayer of graphene which is identifiable through it's orientated edges and wrinkles. Image c) demonstrates another similar sample of h-BN on SiO_2 where image d) provides a magnified view showing the light blue region where FLG is deposited onto thick h-BN.

temperature stability of transition metal di-chalcogenides and oxides was studied for both H and T structures. The calculations demonstrated that, for transition metals tungsten and molybdenum, the H structures were found theoretically to be stable whilst T structures were not. Whilst there is limited experimental confirmations for all of the materials' stability, room-temperature $1T$-WTe_2 was found to degrade in an ambient environment[118] where the degradation was noticeable after a period of 1 day and primarily due to the oxidation of the material. Degradation of MoS_2 electronic devices was noticed after being left in an ambient environment, however these effects were found to be reversible after thermal annealing[119].

Studies on the chemical stability of hexagonal boron nitride nanotubes reveal a resistance to degradation at temperatures over 700^oC [120] in air. This surpasses the stability of carbon nanotubes which are stable up to 400^oC in air[121, 122]. In one study it was found that annealing in a reducing or vacuum environment of approximately 400^oC will result in hole doping upon exposure to ambient conditions [123]. Other studies probe the stability of graphene in air with Raman spectroscopy and report a stability of monolayer graphene at temperatures up to 500^oC [124].

Similar studies on few layer h-BN at high temperature in air have reported stability up to 1100^oC whilst oxygen is unable to penetrate through making h-BN an ideal corrosion resistant coating[125]. The calculated energy required to remove a carbon atom from graphene was estimated to be 7.4 eV [126] whereas the energy required to remove a BN pair is estimated at 15 eV [125]. This highly desirable behaviour has been made use of in the study of rather more volatile 2D-materials such as black phosphorus where oxidation happens in a matter of hours [127]. By encapsulating 2D materials susceptible to environmental conditions with h-BN it is possible to avoid any degradation in the material that would otherwise be present[51, 128].

3.2 Scanning Probe Methods

Throughout this study the AFM used was a Bruker Multimode, III, IV, and VIII. For the purposes of monitoring the deflection signal during the operation of various sub-methods we use a home mode electronic 'break-out' box. This electronics box simply allows the deflection signal to be monitored via a standard BNC connector which is fed into a lockin amplifier (Stanford Research Systems SR830).

3.2.1 Sample Vibration

In the application of FMM, UFM and HFM methods the sample must be vibrated at frequencies around 4 MHz. To implement this we use a piezo transducer disc with wrap-around electrodes fabricated by PI Ceramics (PIC 151 Material). The material used is a blend of PZT (Lead Zirconate Titanate) with a thickness tuned so that the thickness resonance is approximately 4 MHz. In applying a voltage to the actuate these transducers we ensure that the top plate is grounded unless otherwise stated, this is to ensure that there was no electrostatic interaction with the tip/sample. In addition to this the wires connecting the piezo to the coaxial cabling were twisted such that any outside electromagnetic interference would cancel out and also to reduce the cross-talk between wires. Finally to mount the sample on the piezo actuator we first attach a thin glass cover slip with cyanoacrylate and upon this we use a powdered crystal salol (Phenyl Salicylate) which has a melting point of 41.5 ^{o}C to fix the sample to the glass cover slip. Salol is chosen as it freezes in a highly crystalline nature and will minimise the attenuation of ultraonic vibrations to the sample.

3.2.2 Tip Vibration

For the application of HFM and E-HFM it is also necessary to vibrate the tip. For this we needed to modify the existing tip-holder to incorporate a high frequency piezo transducer as the piezo used for tapping mode was not sufficient.

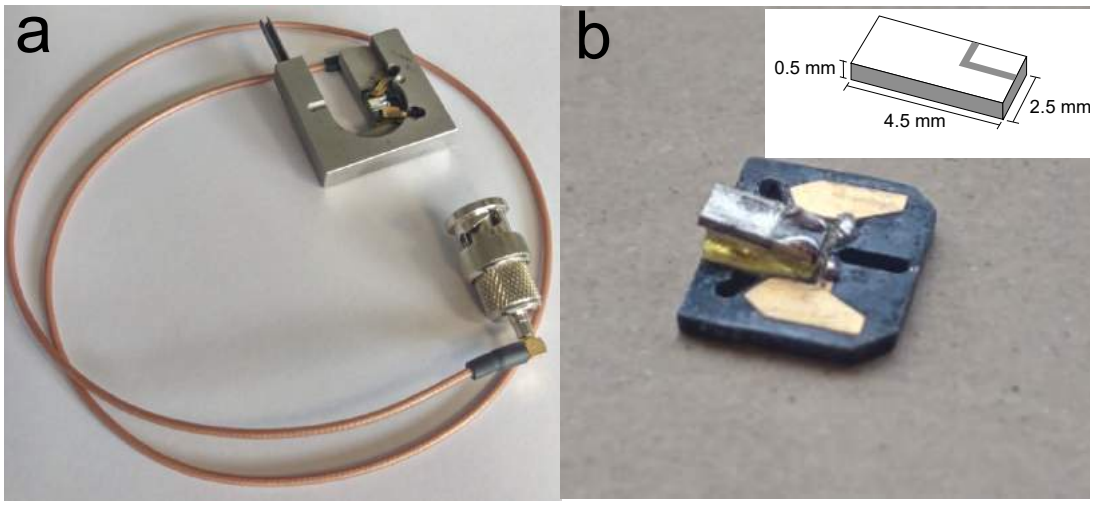

Figure 3.4: Image a) custom tip holder with BNC connector used in HFM and E-HFM experiments. Image b) shows the insert with attached piezo from APC International. The piezo itself is attached to the plastic insert with epoxy, the angle of the piezo is made such that it is similar to standard tip-holders making an angle of approximately 15^o. Inset is a diagram of the piezo dimensions, white areas are the electrodes where the right hand side is the wrap-around electrode allowing contact to top and bottom from the one side.

The tip holder was fabricated in-house and was designed to fit in all multimode microscopes, see Fig. 3.4.

The tip holder, being electrically conductive, was used as the ground and as such was connected to the BNC connector. This linked the ground of the function generator to that of chassis of the AFM. We use a network analyser (Agilent 4395A) to measure the frequency response of the tip piezo in HFM and E-HFM experiments. The network analyser was setup to measure the power transmitted through the piezo as seen in Fig. 3.5.

To understand which piezo modes are attributed to each frequency we quote the following dimensions: 2.00x0.50x4.50(wxhxl) in units of mm. Therefore we calculate the natural frequencies of the piezo given that they can be approximated to $f_0 = N_T/x$ where N_T is the frequency constant (N_T ≈2005/1524 for thickness/length or width for APC material 840) and x is either the height width or length. The resonant frequencies for the height, length and width are given as: f_h=4.01 MHz, f_l=339 kHz and f_w=762 kHz. The width expansion mode is

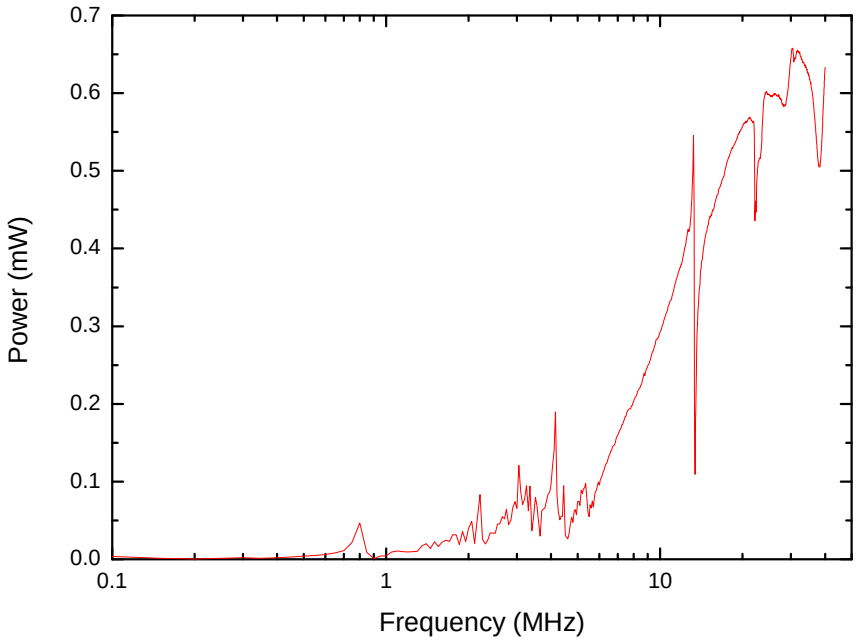

Figure 3.5: The power allowed to pass through a piezo transducer as a function of frequency up to 40 MHz with a driving power of 1 mW. Several peaks or resonances are seen and attributed to various modes of the piezo vibration.

present at approximately 800 kHz and we do not see the length expansion mode in this figure, there are also 3 other resonances seen at 2.3 MHz, 3.2 MHz and 13.2 MHz. We attribute these frequencies to the shear-mode resonances.

3.2.3 Electrostatic/Heterodyne Force Microscopy (HFM)

In HFM experiments the tip and sample were driven by two Keithly 3390 function generators with a frequency range of 0-50 MHz. To ensure there was no drift in the difference frequency, the internal clocks were synchronised with that of the lockin amplifier. This synchronisation was important to avoid drift in the phase detection of the heterodyne signal.

Chapter 4

Morphology of 2D Materials and Their Heterostructures

The morphological structure of materials and devices is often linked closely with the mechanical integrity and other such properties of devices. It is therefore a useful way through which to gain an understanding into the state of the material under any given condition. In this section we study the morphological properties of various 2D materials and their heterostructures in a variety of environments. The most prominent of morphological effects that we study is the Moirè pattern which is achieved when the hexagonal structures of graphene and h-BN are stacked upon one another. The work carried out in this chapter is in collaboration with researchers at the University of Manchester who provided the aligned graphene on h-BN samples.

4.1 Graphene on Hexagonal Boron Nitride

The electronic properties of graphene have been found to be greatly improved if one uses atomically flat h-BN instead of SiO_2. This is has been found to be due to both the absence of doping from the substrate and also from a reduced surface roughness[49]. Not only is h-BN useful as a substrate for graphene based

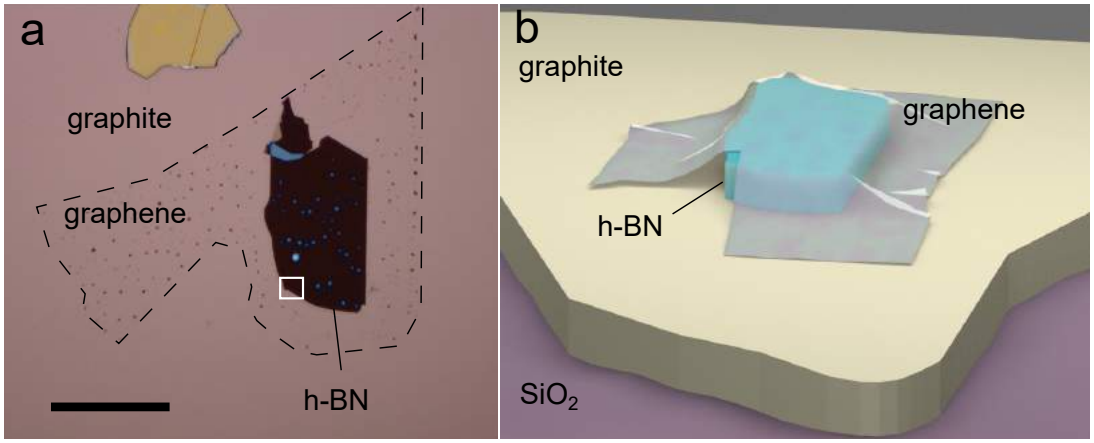

Figure 4.1: Image a) shows an optical image of the sample used, showing graphene (outlined with a dashed line) on a slab of thick h-BN which is resting on a larger flake of graphite. The scale bar shown is approximately 50 μm. The area of interest for the purpose of most AFM studies in this section is shown within the white square. The image in b) is a schematic representation of the sample from a 3D perspective showing the layer ordering and that the graphite flake sits on an SiO_2 substrate.

devices but it also is an important material in the devices themselves. Hexagonal boron nitride has already been used as an ultrathin dielectric in contact with graphene[129, 130] in addition to its use in other devices such as tunnelling transistors [131, 132]. It is therefore of importance for the future application of graphene on h-BN in electronic devices to understand the behaviour of the two materials in contact. In this section we study the morphology of monolayer graphene and MLG on h-BN substrates.

The samples of graphene on h-BN were produced by a method similar to that shown in section 3.1.2 by the graphene group at Manchester University whereby a layer of h-BN was exfoliated onto a slab of graphite on an SiO_2 substrate and a graphene flake later transferred on top. The flake studied is seen in Fig. 4.1. The sample studied in this section is where the graphene and h-BN lattices are aligned to within $\approx 0.5^\circ$ [133].

We are interested in observing any difference in the morphology of graphene on h-BN compared to graphite. For this we study the sample in Fig. 4.1 with both contact mode AFM and UFM, the results of which are seen in Fig. 4.2.

The topography and UFM stiffness maps shown in Fig. 4.2 show a prevalence

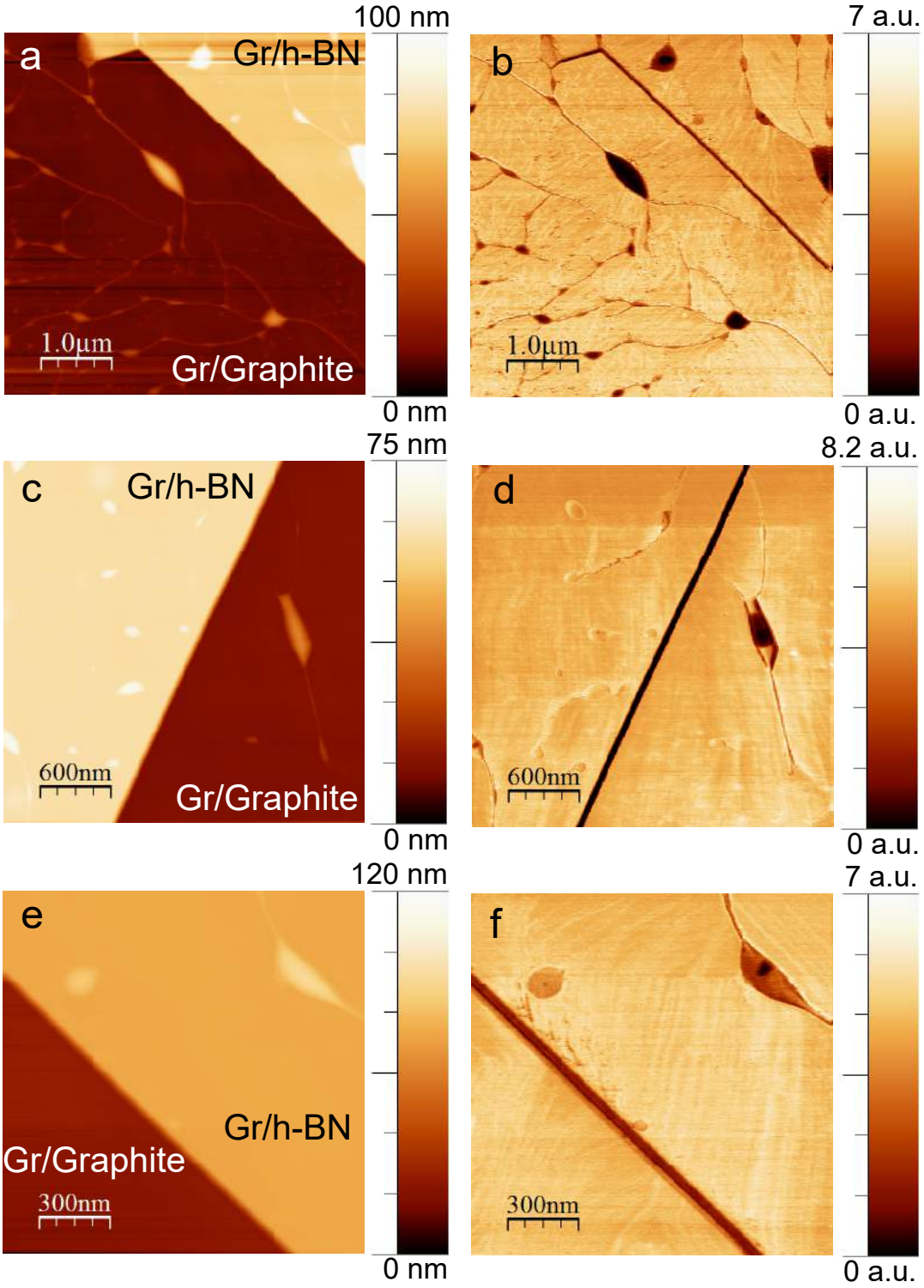

Figure 4.2: Topography (a,c,d) and UFM (b,d,f) maps of monolayer graphene aligned on h-BN/graphite. Thicker regions denote the h-BN flake (50 nm thick). Scans taken at a set force of approximately 3 nN. In both the topography and the UFM maps, regions of decreased stiffness are seen that are elongated and connected through thinner delaminations.

of delaminated regions which appear as bubble like structures. These are observed in both graphene on graphite as well as on h-BN. Whilst in topography these delaminated regions appear to be similar on both the graphite and h-BN, we see a slight difference when imaging with UFM. From Fig. 4.2b we observe that some of the delaminations of graphene on graphite (lower left) appear darker than those on h-BN. We also notice that the delaminations on h-BN appear to have dark spots located close to the centre of the delamination. The reason that we observe a lower stiffness in the delaminations on graphite compared to h-BN is unclear although it may indicate that there is a higher level of intrinsic stress present in graphene on h-BN which may arise due to the lattice mismatch between graphene and h-BN. We also propose that darker spots seen in the centre of most delaminations of graphene on h-BN, but also some on graphite, may be the buckling of the structure due to the ultrasonic amplitude applied during UFM operation.

4.2 Graphene on Hexagonal Boron Nitride: Moirè Pattern

Graphene and h-BN both share the same structure, being two-dimensional hexagonal arrays of atoms. There is however a slight difference in the lattice constant as explained in section 2.1.2 of approximately 1.7%. Therefore when graphene is stacked on h-BN or vice versa we would expect to see the atoms periodical line up with one another (i.e. they are commensurate/incommensurate). This forms the basis of the Moirè pattern which has been widely observed experimentally[133, 134, 135]. The Moirè pattern will take the form of the two sub-lattices (in this case hexagonal) however the size of the pattern depends largely on the angle of rotation between the sheets of graphene and h-BN, where perfect alignment relates to the largest period of the Moirè pattern ($\approx$14 nm[133]). In this section we continue to study the Moirè pattern of a sample where the two lattices are alligned with each other.

The study of graphene and h-BN Moirè patterns experimentally with an AFM has revealed no detectable variation in the height between the commensurate and

in-commensurate regions[133] indicating that the variation is less than vertical resolution of the system, quoted as $\approx$ 50 pm. However in the same report the Moirè pattern has been revealed through scanning tunnelling microscopy due to the much higher resolution. One additional way of observing the Moirè pattern with an AFM is to use nanomechanical mapping[133].

In this section we probe the morphological and nanomechanical properties of monolayer graphene aligned on hexagonal boron nitride, yielding the largest Moirè period possible. As we see from literature the topographical differences observed between commensurate and in-commensurate regions are not detectable through contact AFM, we therefore scan the sample with both frictional force microscopy (FFM), Fig. 4.3) and ultrasonic force microscopy (UFM) (Fig. 4.4).

To estimate the frictional forces quantitatively we follow the method set out previously[136] where the cantilever used was a ®BudgetSensors contact mode cantilever with a spring constant k_c $\approx$0.2 Nm^{-1}. We estimate the deflection sensitivity as 150 nm V^{-1} and the tip height h_t as 17 μm.

From Fig. 4.3 we observe that there is a clear contrast in the frictional characteristics of the different regions of the Moirè pattern. In Fig. 4.3a we observe a clear hexagonal structure where each hexagon is surrounded by a clearly defined region of increased friction, there is however a slight distortion in the pattern. Figure 4.3b shows a less well defined hexagonal pattern due to the increase in the set force to 75 nN. We also observe that the regions where the friction is higher appear to be larger. There are several reasons as to why one may observe an increase in the friction, such as an increase in the contact area with the AFM tip due to a variation in mechanical stiffness and adhesion to the sample which was proposed initially elsewhere[133]. Whilst an increased level of adhesion may account for the increase in the FFM signal it does not explain the broadening of this region that we see at higher set forces. One possible explanation for the broadening of the commensurate/incommensurate region at higher set forces is that the tip is able to partially alter the alignment of the graphene with respect to the h-BN resulting in an increase in the adhesion over a wider area. The fact that we also see a less well defined hexagonal structure at higher set forces also adds support to the claim that we are partially deforming or causing the graphene to 'bunch-up' at higher levels of frictional force.

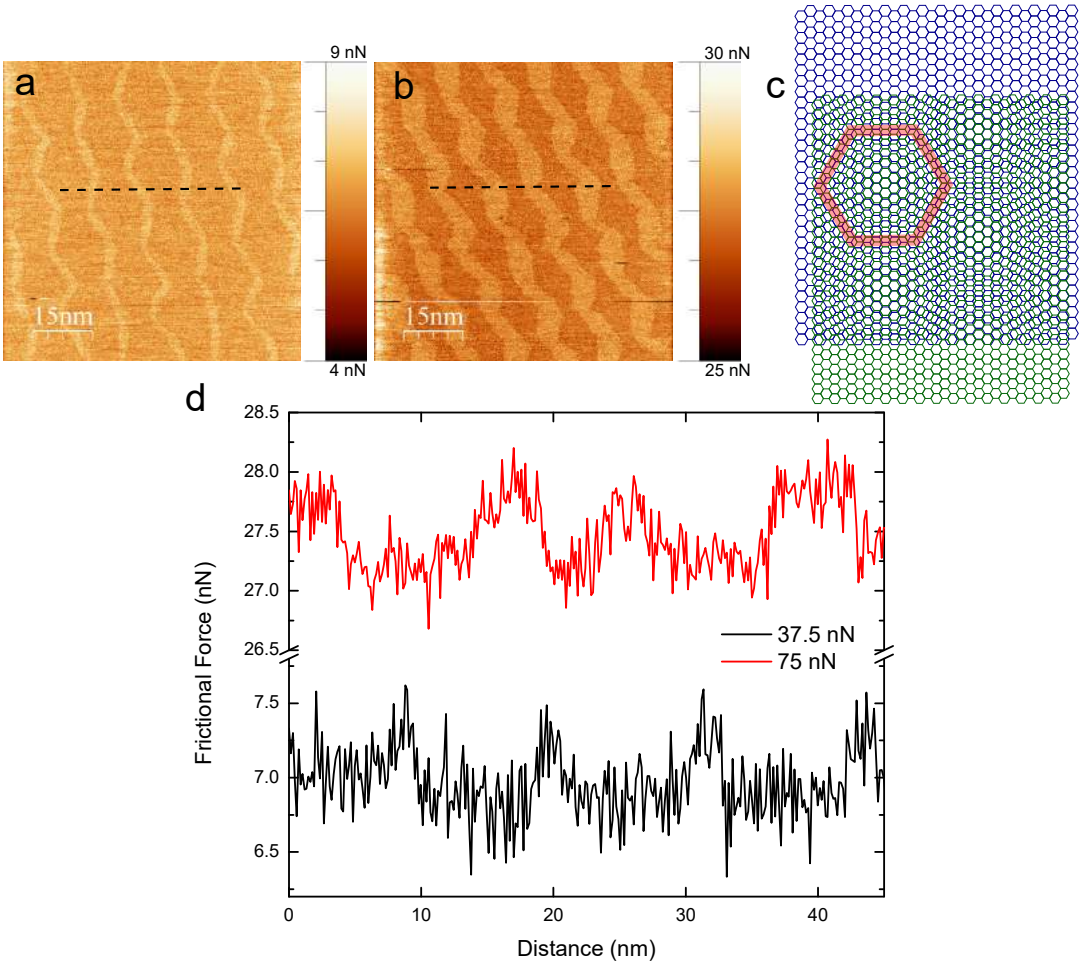

Figure 4.3: Images a) and b), taken on the trace and retrace of the same scan, show the frictional force acting on the cantilever for set forces of 37.5 nN and 75 nN respectively. Tip velocity in both scans was 300 nm s^{-1}. Image c) shows a schematic representation of the formation of the Moirè pattern where two hexagonal patterns differing in size by 10% are superimposed. The resulting super-lattice is highlighted in red. Graph d) shows the two traces of the FFM in a) and b) with the dashed black line.

To study the nature of the gr/h-BN Moirè pattern stiffness and adhesion properties we employ ultrasonic force microscopy. As the UFM contrast can depend on the tip-sample adhesion as well as the mechanical stiffness of the sample, one would expect to observe the Moirè pattern. By obtaining a UFM image of the same sample as shown in Fig. 4.3 we see clearly the hexagonal pattern as with FFM, see Fig. 4.4.

In Fig. 4.4a we observe, albeit with a level of difficulty, the hexagonal superlattice that is the Moirè pattern with force modulation microscopy. As FMM responds only to sample stiffness and is relatively unaffected by adhesion we deduce that local variations in the mechanical stiffness are present and account for at least some of the contrast observed. In addition to this in Fig's. 4.4b-d we probe the mechanical and adhesion properties with UFM. With UFM we do not always observe the same contrast across all scans. If we compare Fig's. 4.4b and d with c we see that there is an inversion of the contrast, whilst the contrast in Fig. 4.4c was only observed once throughout all UFM scans it may still hold a clue as to the adhesion/stiffness interaction. As all images in Fig. 4.4 were taken at different points over the sample and Fig's 4.4b-d were taken over the period of several days, we propose that environmental factors such as humidity and temperature may affect the adhesion between the tip and the sample and therefore the UFM contrast. We additionally rule out the claim that these areas are of varying degrees of alignment as we do not observe any noticeable change in the Moirè period. In other studies into the mechanical properties of graphene aligned on h-BN a narrow region of high stiffness is observed showing a clearly defined, sharp hexagonal pattern[133]. This is in agreement with the UFM image in Fig. 4.4c but not b or d. One possible explanation for this is that in most cases the tip-sample adhesion variation dominates the UFM contrast, however if the adhesion is reduced through some environmental factor then the stiffness will dominate. It should also be pointed out that the regions of lower UFM signal in Fig's 4.4b and d would correspond to regions of either high tip-sample adhesion or low h-BN/graphene adhesion, which would allow the tip to partially separate the graphene from the h-BN. A theoretical study into the adhesion between h-BN and graphene shows that these regions of low UFM signal in Fig's 4.4b and d would correspond to low interlayer adhesion [137]. If this is the case then we

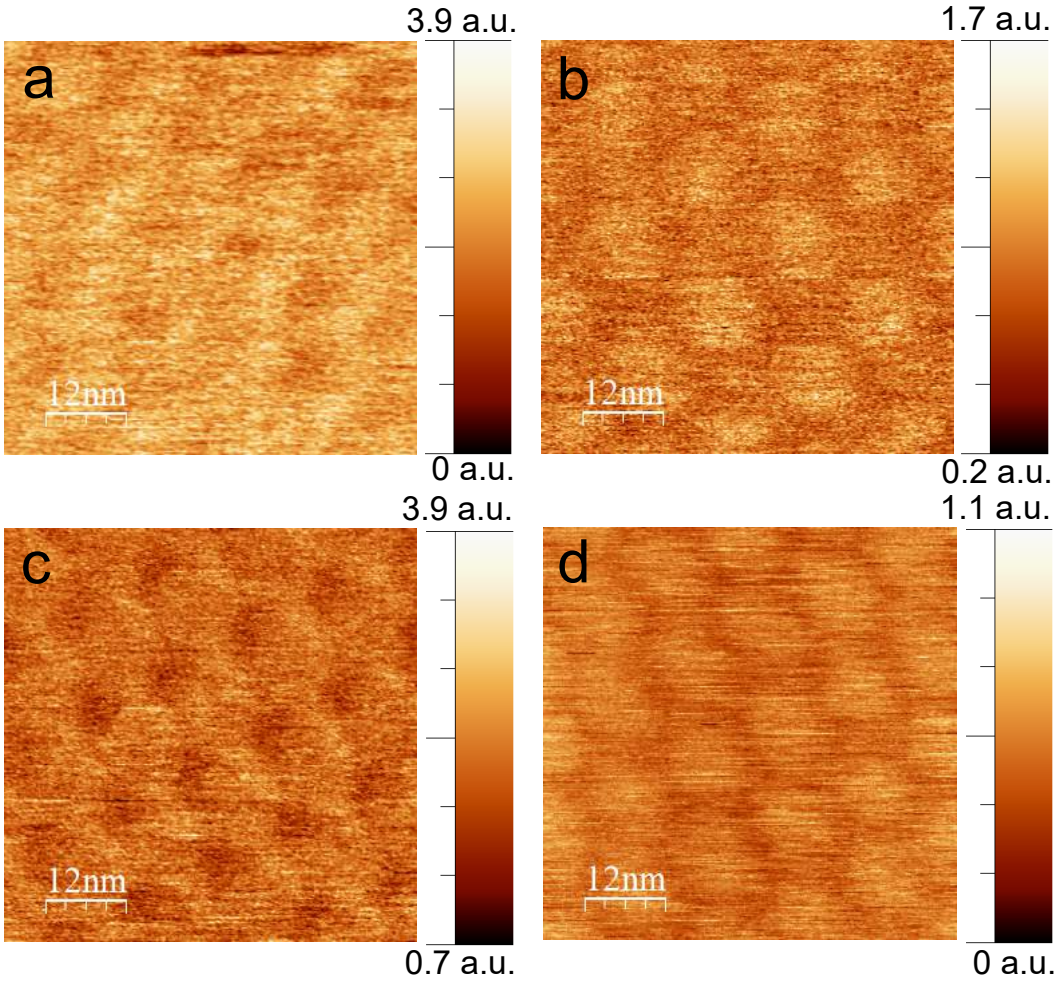

Figure 4.4: Sample stiffness maps of different areas of the Moirè pattern where Image a) shows FMM at a tip speed of 120 nm s^{-1}, b-d) UFM images at tip speeds of 150, 50 and 30 nm s^{-1} respectively. In all images the set force was kept low in the range of 0-5 nN. Image scales are not comparable between UFM images due to variation in the piezo displacement in different regions of the sample.

may be observing a lower UFM signal as the tip is able to partially detach the graphene from the underlying h-BN. The variation in the adhesion seen in [137] is a relatively broad transition, similar to that seen with UFM giving more support to this claim.

4.3 Summary

To summarise this chapter we have studied the Moirè pattern observed when graphene is aligned on h-BN and deduced that the local sample adhesion plays a significant role in the system. This increased apparent adhesion may result from a corrugation of the atoms due to lattice mismatch. Using frictional force microscopy (FFM) we have measured well defined hexagonal boundaries which we attribute to a higher tip-sample adhesion. In addition to using FFM we have studied the Moirè patterns with UFM whereby we were also able to observe the hexagonal structure. One key difference between FFM and UFM is that, for the most part the boundaries of the hexagonal regions were much more clearly defined with FFM than with UFM. This may be attributable to both interlayer adhesion and sample stiffness. It was calculated theoretically that the h-BN/graphene interlayer adhesion is weaker in these hexagonal boundary regions and the transition is relatively broad [137], these regions correspond to areas of low UFM signal suggesting that during the UFM sample oscillation the tip is able to partially pull-up the top graphene layer. In contrast we propose that the mechanical stiffness of the hexagonal boundary is a much sharper transition as shown through quantitative nanomechanical mapping[133]. We propose that the decreased stiffness in these boundaries creates a larger tip-surface contact area which leads to higher frictional forces. This is backed up by the claim that we observe a sharp transition in the friction signal seen where additionally we were able to broaden these areas further by applying a higher load to the sample through the AFM tip. These local mechanical and adhesion properties may have implications in the behaviour of electronic and electromechanical devices where it may be possible to use the super-lattice to observe and make use of interesting new physics.

Chapter 5

Nanomechanical Phenomena

5.1 Subsurface Imaging in 2D Materials with Ultrasonic Force Microscopy

The work performed in this section was done in conjunction with collaborators: Oleg Kolosov, Franco Dinelli and Pasqualantonio Pingue. All experimental results and theoretical calculations performed were carried out by the author, some of which have contributed to the submission of publication, see publication list for more details.

Ultrasonic force microscopy (UFM) has shown extensively its ability to detect the subsurface structure of many systems. The question often arises as to how deep one can observe beneath the surface? The answer to this question depends greatly on the stiffness of the sample, the effect the subsurface detail has on the mechanical integrity of the system as well as probe surface area and the adhesion between the tip and the sample. As a general rule the greater the effect on the mechanical integrity of the sample the subsurface detail has, the more easily it will be detected and therefore will lend itself to being seen at greater depths.

As UFM allows the user to probe the mechanical properties of a sample with nano scale resolution it is apparent that this is a near-field technique, as is the case of HFM as discussed in section 2.3.4.1. Considering an elastic wave travelling

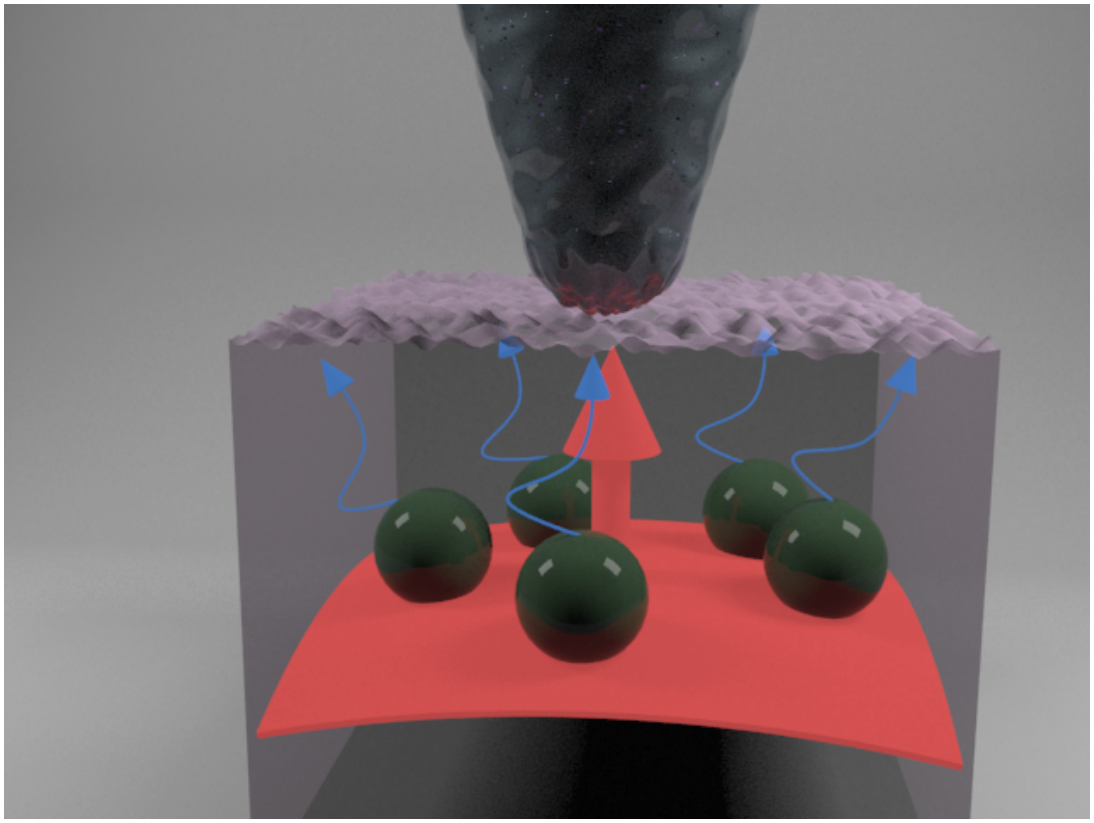

Figure 5.1: Illustration of the process of observing subsurface structures in ultrasonic force microscopy. Spherical inclusions (dark green) in an medium of differing elastic properties (pink) generate mechanical evanescant waves (light blue) when an incident plane wave (bright red) is present.

through a typical medium such as GaAs (v_l=5238 m/s in the [110] direction [138]) then for the wavelength, with typical operating frequency of 4 MHz, we obtain a wavelength of λ=1.3 mm, far larger than the features one would hope to resolve. Therefore UFM contrast is believed to be largely due to evanescent waves present near the surface. These waves have their origins in a mismatch of the stress at the boundaries between areas of varying mechanical stiffness as is demonstrated in Fig. 5.1

Fig. 5.1 shows the basic concept of near-field imaging in UFM. The incoming plane wave shown in red is incident on the subsurface detail in the vicinity of the tip. As the incident plane wave comes into contact with the subsurface detail a stress discontinuity arises in the form of an evanescent strain wave, analogous to

those used in near-field optics. These exponentially decaying waves provide the contrast which is picked up by the probe as a change in the tip-surface contact stiffness.

We are particularly interested in the application of UFM to measure the subsurface properties of 2D materials and their heterostructures. This is of importance as many devices fabricated from 2D materials will consist of many layers and one would like to be able to test the mechanical integrity of such devices. This may include trying to locate possible debris, wrinkles or other features beneath the surface that may impact on the operating efficiency of the device. One particular difference that all vdW solids have over conventional '3D' materials is that they possess a high degree of mechanical anisotropy, that is the in-plane properties are largely different from the out of plane properties. These materials are often referred to as transversely isotropic as the in-plane behaviour is, in general, isotropic. Here we study the effect of sample anisotropy on the resolution of UFM.

5.1.1 Theoretical Interpretation: Sample Anisotropy

Korneev and Johnson [139, 140] developed a theoretical framework to describe the surface perturbation when waves generated by an earthquake were scattered by an inclusion. This interpretation was however found to be insufficient in describing the observed contrast in ultrasonic microscopies (UFM/HFM), due largely to the much smaller scale. This is in agreement with similar studies performed on HFM (see section 2.3.4.1). The solution postulated for the origin of the subsurface contrast was believed to have its roots in the stress fields beneath the surface. The understanding behind this hypothesis is that with UFM we are measuring, effectively, the distance required by the sample vibration to reach the non-linear part of the tip-sample interaction. The distance to this region depends on how far indented into a sample the dynamically stiffened tip becomes, something that is determined largely by the stiffness of the sample located within the stress field of the probe. It is therefore necessary to understand the extent of the stress field both in terms of depth but also radially from the tip to understand the sample's contribution to the UFM signal. To understand the propagation of the stress

field beneath the AFM tip in contact with 2D materials we consider two cases, the first of which is an elastic sphere of radius R_t in contact with an isotropic medium. The stress distribution is given by Eq. 5.1

$$\sigma_z = -\frac{3F^{1/3}}{2\pi}\left(\frac{4E^*}{3R_t}\right)^{2/3}\left(\frac{z}{u^{1/2}}\right)^3\frac{g^2u}{u^2+g^2z^2} \tag{5.1}$$

Here F is the force applied by the AFM tip, E^* is the effective combined elastic modulus of both tip and sample, r and z give the radial and vertical position within the stress field whilst g the effective contact radius and u the axillary variable are given by

$$u = \frac{1}{2}\left((r^2+z^2-g^2+\left[(r^2+z^2-g^2)^2+4g^2z^2\right]\right)) \tag{5.2}$$

$$g = \left(\frac{3FR_t}{4E^*}\right)^{1/3} \tag{5.3}$$

This case predicts well the stress distribution for isotropic materials however 2D materials are highly anisotropic, more specifically they are transversely isotropic where the in-plane properties are isotropic but vary from the out-of-plane properties.

The second case we discuss is therefore where the isotropic elastic indenter is in contact with a transversely isotropic medium such as a stack of 2D materials. These transversely isotropic materials can be classified by 5 elastic constants a_{11}, a_{12}, a_{13}, a_{33} and a_{44}. The theoretical interpretation of the stress field inside such a transversely isotropic material from an elastic spherical indenter was produced by Dahan and Zarka [141]. Their theoretical approach is rather complicated and lengthy so has been omitted. Instead we apply their method to a series of 2D-materials which can be seen in Fig. 5.2, where the elastic constants used for the three materials are given in Table. 5.1.

We see that for the transversely isotropic case, in particular graphite, the depth at which the stress field propagates is greatly increased. This is due to not only the decreased out of plane stiffness but also a much lower inter-layer shear modulus G_{23}, this effectively 'focuses' the stress to a region under the area

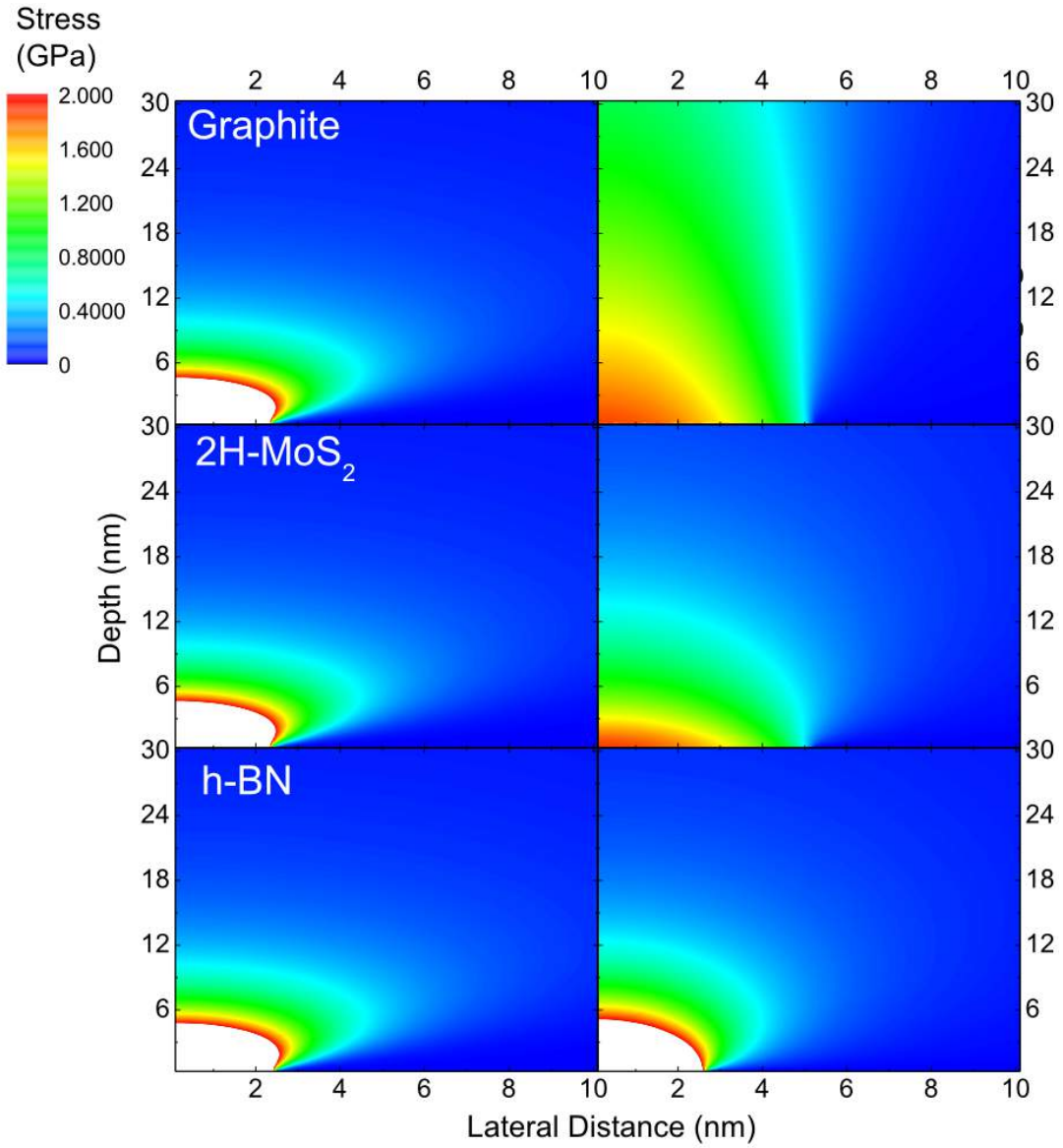

Figure 5.2: The resultant stress field σ_{zz} for MLG/graphite, multilayer 2H-MoS_2 and h-BN. Left images are for the isotropic case where out-of-plane moduli and Poisson ratios are taken from the known in-plane values. Images on the right are for the transversely isotropic case. The force F applied to the tip in all cases is 100 nN whereas the indenter radius R=10 nm. All values of stress are given in GPa. The indenter is treated as an isotropic Silicon sphere with E=62 GPa and ν=0.27. Areas shown in white are areas of higher than 2 GPa stress.

Material	E_1 (GPa)	E_3 (GPa)	ν_{12}	ν_{13}	G_{23} (GPa)
MLG/Graphite	1153[46]	39.5[46]	0.194[46]	0.006[46]	0.268[46]
2H-MoS_2	330[58]	160[45]	0.25[142]	0.18[45]	19[143]
h-BN	811[44]	38[45]	0.18[45]	0.01[45]	7.7[44]

Table 5.1: Table of values used in the simulation of the stress field σ_{zz} for transversely isotropic materials in Fig. 5.2. Where E denotes Young's modulus, ν Poisson ratio and G the shear modulus.

of contact. Therefore only material that is present within the stress field may contribute to the overall UFM signal. That is the resolution of UFM is governed by the width/depth of the stress field. We therefore propose that a low value of E_3 with low a value of G_{23} results in a deeply penetrating stress field and will allow for the detection of structures deep beneath the sample.

As UFM is a contact mode method the tip will apply a static force to the sample, this is known to increase the amplitude at which one will see any signal. In addition to this the force applied to the sample will vary with time as it is vibrated with typical r.m.s amplitudes 0.2-0.5 nm by the piezo[99] causing the tip to indent into the sample. To avoid confusion this is in addition to the static force one always applies in contact mode AFM. Estimating the tip dynamic stiffness as a point mass on a spring $k_{eff} \approx m\omega^2 = 10^4 \mathrm{Nm}^{-1}$ we see that the dynamic force applied to the sample may be in the region of 10^3 nN. Clearly there are a wide range of forces that are present in one amplitude modulation cycle. To understand the role the applied force plays on the depth of the propogating stress field we monitor σ_{zz} as a function of depth directly beneath the tip (r=0) for a transversely isotropic medium indented with a spherical isotropic indenter. By plotting the point at which σ_{zz}=0.1 GPa for several applied loads we see how the depth varies between the three materials, graphene, h-BN and MoS_2. The results can be seen in Fig. 5.3.

It should also be noted that we have chosen the particular value for σ_{zz}=0.1 GPa to illustrate the load dependence of the depth. It is slightly more complex to discuss the depth at which any object in a variety of materials will contribute equally to the UFM signal as one has to consider the size of the object in relation

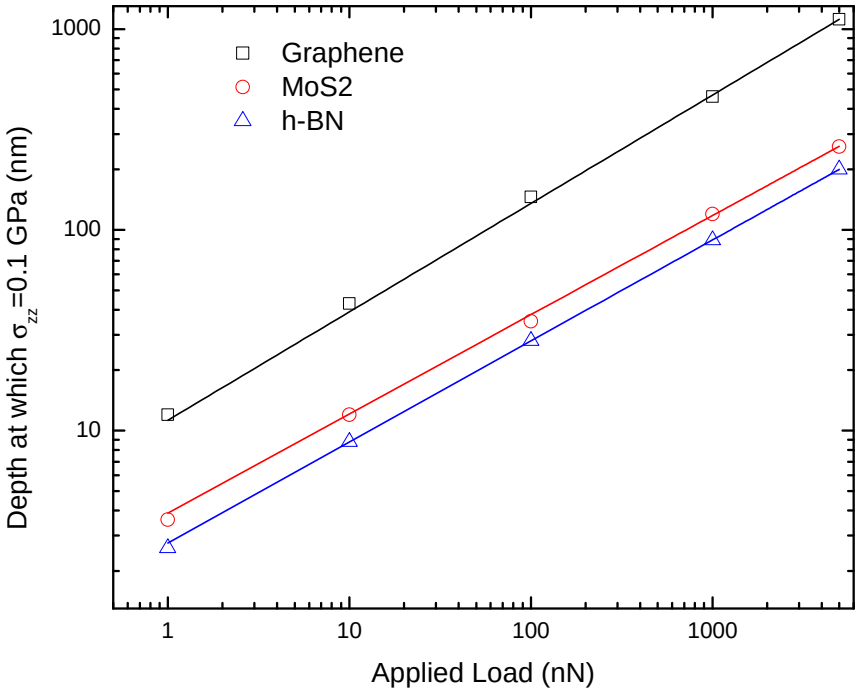

Figure 5.3: The depth at which the stress σ_{zz} decreases to 0.1 GPa directly beneath the tip. The materials plotted are multilayer graphene (black), $2H$-MoS_2 (red) and h-BN (blue). All values were calculated numerically.

to the whole surface area where $S_{\sigma_{zz}=0.1GPa}$. Because of the difference in material elastic properties $S_{\sigma_{zz}=0.1GPa}$ will vary drastically between MLG/graphite and multi-layer MoS_2 as an example (See Fig. 5.2).

Therefore we summarise that the subsurface lateral resolution and also the depth at which UFM is able to sense is greatly increased by the sample anisotropy. We see that the most pronounced effect of sample anisotropy is in graphene compared to MoS_2 and h-BN, this is due to it's low value of E_3 but also it's low interlayer shear modulus G_{23}= 0.268 GPa.

5.1.2 Observing Subsurface Structure in 2D Materials

As the UFM signal is derived from the elastic properties located within the stress field, objects located close to the surface will be more easily resolved than the same objects at a greater depth. This is because the surface area of the object in relation to the surface area of constant stress is much higher than it would be if the depth z were larger. To understand how the depth z of an object such as a pocket of air or debris buried beneath the surface of a stack of 2D materials will affect the UFM signal we use a simple FEA analysis model. In this model the tip-surface contact area is modelled as a circular area with radius R_t=10 nm over which the a load F is applied. We then bury a cylindrical inclusion with radius r_d=10 nm and height h_d=5 nm at a depth z. To estimate the difference in UFM signal we take the difference in indentation for the case where the tip is positioned directly above the inclusion and where the tip is a lateral distance of 30 nm away. The results of this simulation are seen in Fig. 5.11

As one would expect the observed difference in the averaged indentation A_{diff} shows that as the inclusion increases in depth the effective UFM signal decreases as $A_{diff} \propto V_{UFM}$. We however see that A_{diff} approaches a limit for depths of approximately 50 nm. This may represent a decrease in the lateral resolution of the UFM and increasing the distance between the two points at which we calculate A_{diff} would be expected to show a depth dependence beyond the one seen in Fig. 5.4.

This difference in deflection corresponds to the additional movement required by the piezo transducer to obtain an ultrasonic signal, if this additional deflection

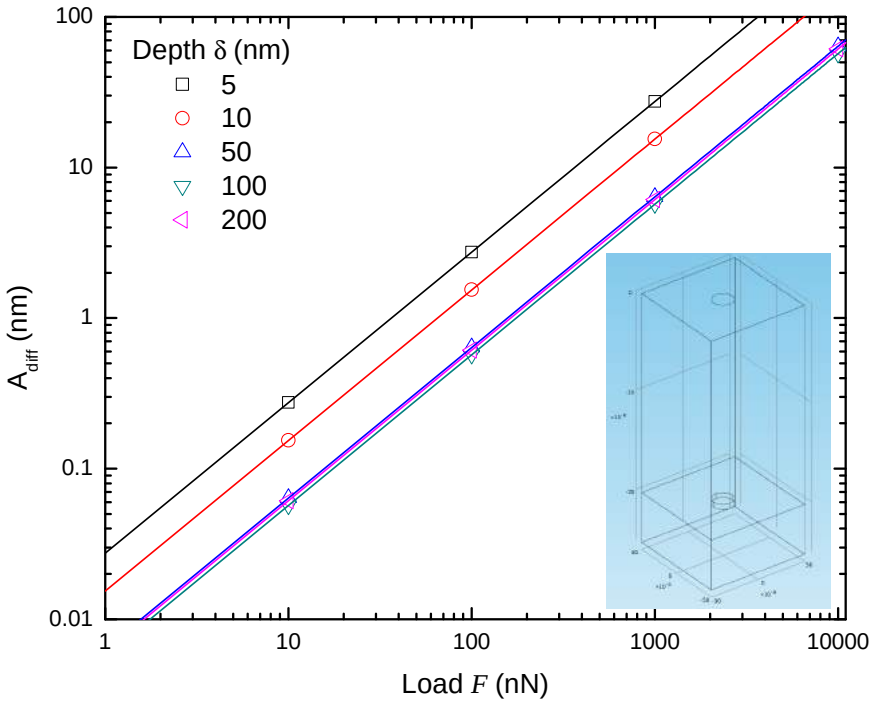

Figure 5.4: The difference in the indentation between the tip located directly over the cylindrical inclusion and at a distance of 30 nm along the surface. The cylindrical inclusion (r_d=10 nm, h_d=5 nm) is modelled as an extremely soft material designed to represent air. The material above and below it is graphite modelled as an transversely isotropic medium. Inset is a wire-frame diagram of the FEA model used for the simulation.

is larger than the maximum amplitude of the piezo then there will be no UFM signal.

It is not possible to come up with a simple analytical expression for the lateral resolution and depth of view for UFM therefore it is only possible through numerical calculations and FEA to predict how deep beneath the surface we can detect.

In order to compare our predictions with experiment we image a series of 2D materials for varying thickness's with UFM. To emulate the situation where there is an inclusion we deposit these materials on a Si/SiO_2 substrate with trenches 300 nm wide etched into them. These substrates were produced for us by Rosamund *et al.* [144]. These flakes were deposited with the traditional mechanical exfoliation. Firstly we imaged MoS_2 as seen in Fig. 5.6.

In Fig. 5.6 we see that the trenches are clearly visible as the UFM signal is virtually nil, indicating a very low relative stiffness. We also see an uneven UFM signal on the supported MoS_2 when the topography appears to be relatively flat, this was thought to be largely due to the uneven nature of the substrate beneath the material and is indicative of an uneven interaction/adhesion with it.

It is believed that material within the stress field is not the only contribution to the UFM signal, in addition, any action that contributes to the reaction force of the sample will be detected by the UFM. This may constitute a flexing of the sample, in this case a bending of the bulk MoS_2 in the region over the trench. We propose that the UFM contrast is then dependent on anything that will provide a reaction force, or lack thereof, to affect the signal. The two main mechanisms we consider are the large-scale flexing of the material which can happen over hundreds of nm to a few μm and to the local variations in stiffness which are present only in the immediate stress-field produced by the AFM tip (See paper No.2 in the list of publications). By considering the system as a series of springs, the stiffness will add in an inverse fashion $1/k_{eff} = 1/k_1 + 1/k_2 + ...$, because of this if there is any one spring that is significantly softer than the rest then this will largely dominate the overall stiffness k_{eff}. We see this in the case of 2D materials suspended over a large trench where k_{flex} is significantly lower than any other stiffness present in the measurement. To illustrate this effect we measure

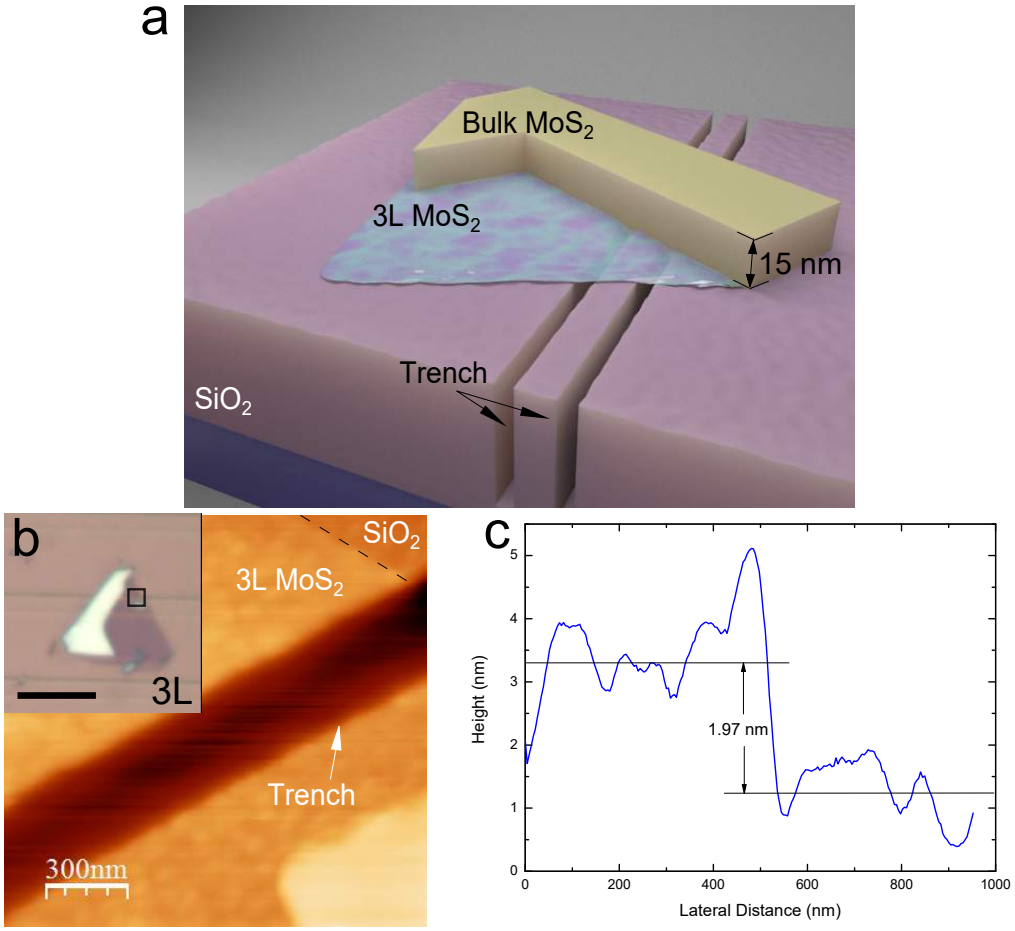

Figure 5.5: Image in a) shows a schematic representation of the sample studied where a tri-layer and bulk section of MoS_2 are part of the same flake deposited over trenches etched into the substrate. Image b) shows an AFM topography image of the edge of the suspended tri-layer section with an optical image of the flake shown, scale bar is approximately 5 μm. Finally the graph in c) shows an average of several traces at the step edge confirming the three layer thickness.

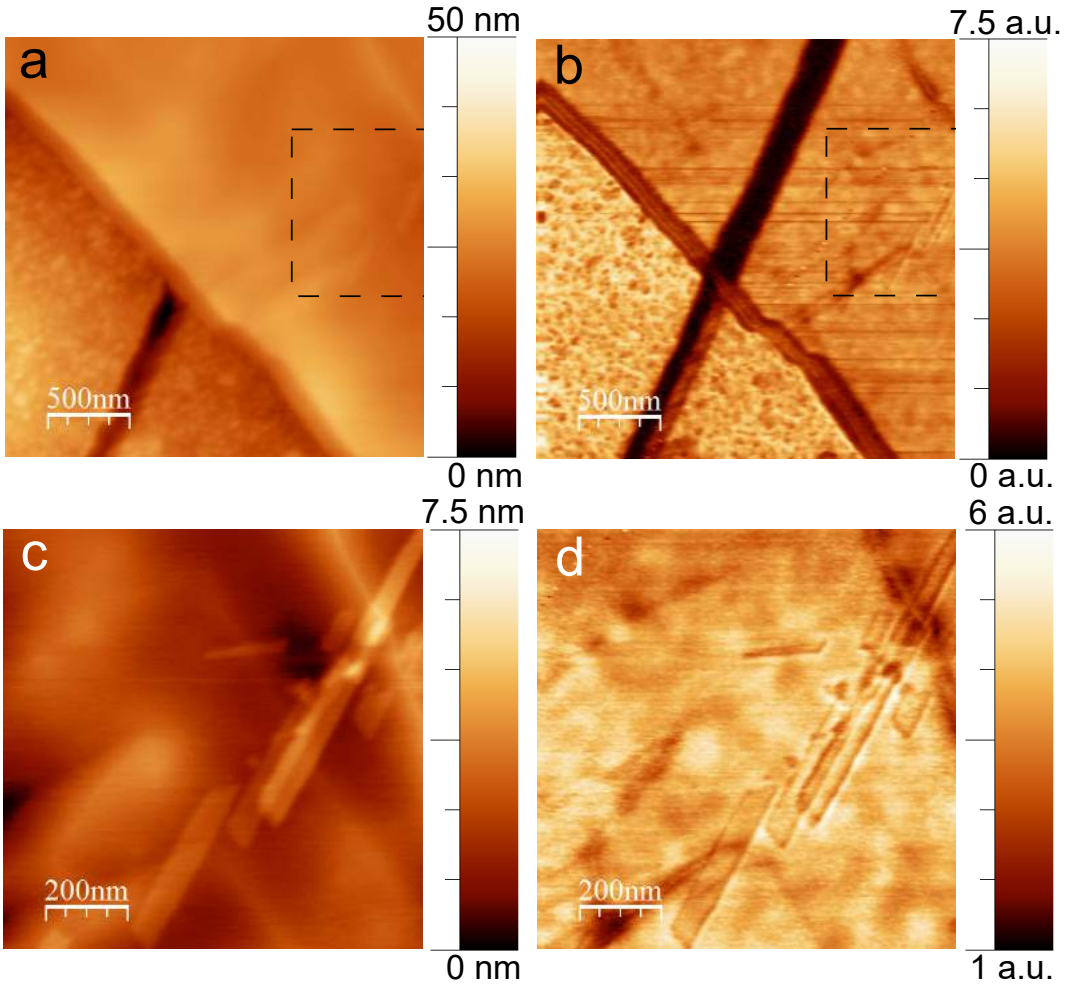

Figure 5.6: Image in a) shows the topography of a MoS_2 sample where a tri-layer thickness is seen to the lower left whilst a thicker bulk material (15 nm) is seen in the upper right whilst a trench of 300 nm width runs beneath the sample from bottom left to top right. Image b) shows the UFM image of the region in a) clearly displaying the trench beneath the thicker material. Images c) and d) are the topography and UFM images of the dashed regions seen in a) and b) respectively. Set force used is approximately 2 nN with a UFM drive amplitude of 3 V_{pp}.

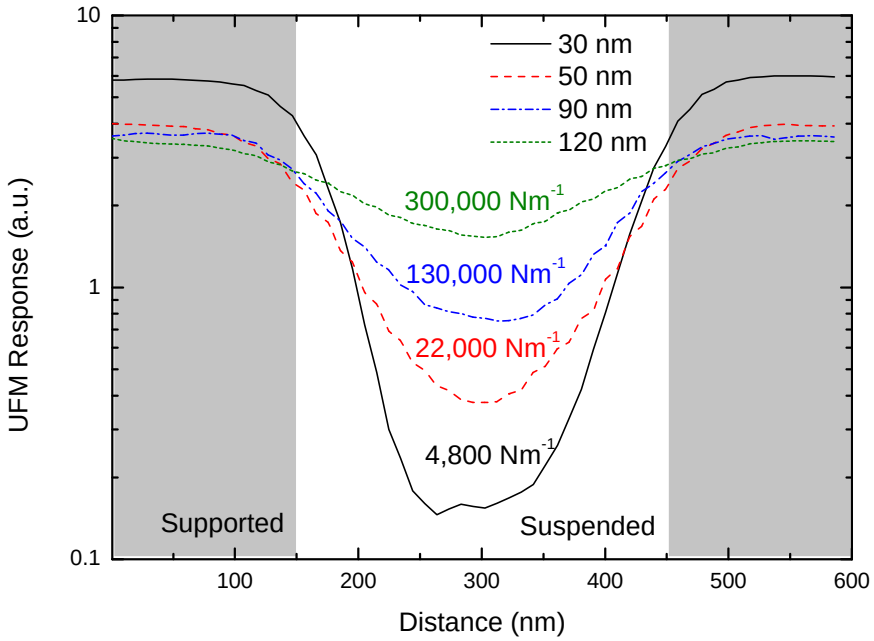

Figure 5.7: UFM signal profile across MLG/graphite suspended over a trench where the centre of the trench is centred at a distance of 300 nm on the graph. We show the UFM profiles for 30 nm (solid black), 50 nm (dashed red), 90 nm (dash/dot blue) and 120 nm (short dash green) graphene imaged with a set force of approximately 10 nN at a frequency of 4.23 MHz and modulation frequency 2.71 kHz. Estimated theoretical values for the stiffness at the centre of the beams are shown alongside the measured data.

the UFM response for MLG/graphite suspended over a 300 nm trench etched into Si/SiO_2 substrate, the results are shown in Fig. 5.7

From Fig. 5.7 we see that as the thickness increases, the UFM signal, which is tied to the measured stiffness, increases over the trench. This is due to the increased flexural stiffness of the MLG/graphite beam. If we compare the UFM signal suspended over the trench against MLG/graphite supported by the substrate we see a clear difference in the signal measured, even for 120 nm thickness. This demonstrates how flexural bending of the graphene will dominate the UFM signal, in this instance, and any structures hidden within the graphite such as a cavity or other such inclusion will be effectively drowned out by the flexural

bending of the sample.

It is also worth nothing that the UFM signal on the supported material decreases appreciably when the thickness goes beyond 30 nm. We speculate that the reason for this decrease is due to two possible causes; firstly the thicker graphite will have more disorder such as layer folding and cavities and therefore a decreased stiffness, secondly we postulate that at 30 nm thickness and below the SiO_2 substrate will have a significant contribution to the signal.

Therefore in summary we have quantitatively analysed the effect of the transversely isotropic nature of graphene, h-BN and MoS_2 and have found this to play a significant role in the depth at which one can see beneath the surface. This depth is especially high for graphene due to its high in-plane stiffness and very low interlayer shear modulus. Not only does the effect of sample anisotropy dictate the depth at which one can detect subsurface objects but also the lateral resolution as the width of the stress distribution is dictated largely by the low interlayer shear modulus found in vdW solids. The extent to which flexural bending depends on the thickness and width of the beam that is flexing under the AFM tip, may be an undesirable effect if one wishes to measure small features such as 50 nm cavities buried in a suspended beam of 2D materials.

5.2 Mechanical Properties of Graphene Grown on 4H-SiC; Effects of Hydrogen Intercalation

In this section we present the work on SiC/graphene systems which was performed collaboratively with researchers from The National Physical Laboratory: Olga Kazakova and Christos Melios; The Institute of Electronic Materials Technology: W. Strupiǹski and from Lancaster University: O. Kolosov, C. J. Lambert, Z. Y. Mijbil and S. Bailey. All samples were grown by W. Strupiǹski whilst all experimental data shown is that of the author. Theoretical calculations were performed by Z. Al-Milli, in preparation for the submission of the results for publication.

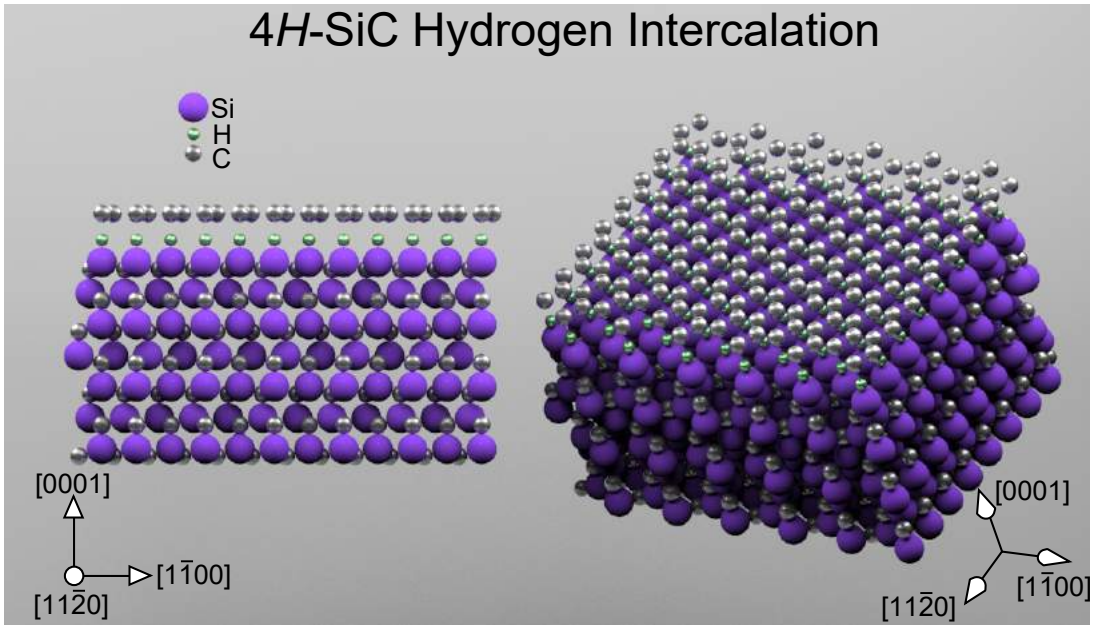

Figure 5.8: Illustration of monolayer graphene grown on 4*H*-SiC intercalated with hydrogen. The crystallographic directions are also shown from a side and perspective view.

Whilst graphene has been shown to have a great deal of desirable properties for a wide range of applications, particularly in electronics, there are still issues with both the high-quality and economical large-scale production. One such route to large scale production of graphene is through the growth on SiC. By heating the SiC substrate at high temperature a hexagonal carbon layer is formed on the surface. Whilst this layer is identical to graphene in terms of its structure it remains bonded to the Si atoms beneath. This detrimentally affects the electronic properties of graphene, a hurdle that would have to be overcome for commercial applications. One potential solution to this is through the intercalation of Hydrogen, effectively removing the effect of the substrate on the graphene layer and restoring its desirable electronic properties [13, 145, 146, 147, 148].

In this section we study changes in the mechanical properties of the samples for various growth conditions to understand to what extent the substrate interacts with the graphene layer/s. As graphene on SiC is a very stiff material we employ differential UFM to obtain quantitative measurements of the mechanical stiffness of the samples.

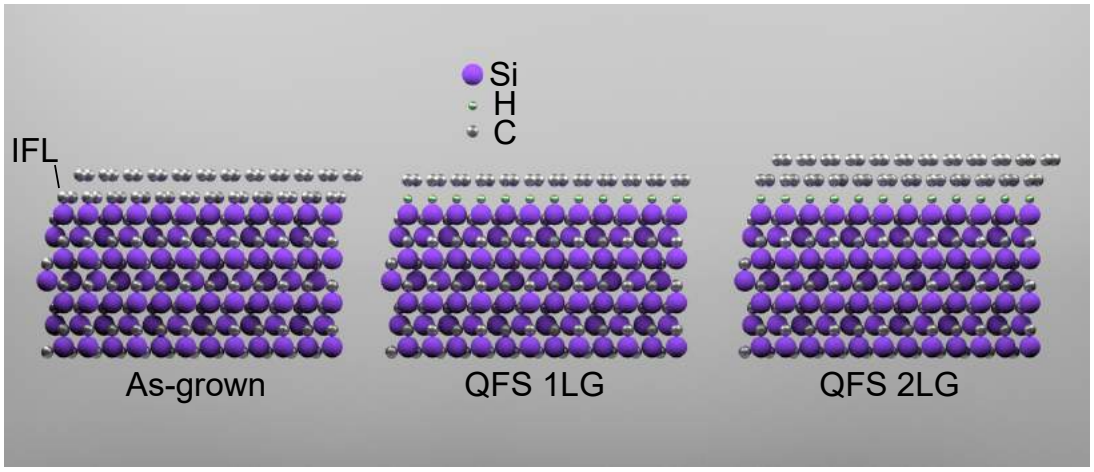

Figure 5.9: A schematic of the three sample types studied in this section. From left to right is the As-grown where the interfacial layer (IFL) is partially bonded to the underlying silicon atoms, QFS 1LG where the graphene has been decoupled from the substrate through hydrogen intercalation and lastly QFS 2LG which is where we have intercalated the As-grown sample with hydrogen leaving two decoupled graphene layers.

The samples studied in this section are divided into three broad sections, as shown in Fig. 5.9: Firstly the 'as-grown' samples where a fresh piece of SiC has been heated to the extent that one or more graphene layers have formed on the surface. The second sample group is 'intercalated' where the as-grown sample has been heated in the presence of hydrogen gas whereby the hydrogen atoms are able to either migrate beneath the graphene layers or penetrate beneath through some high-temperature mechanism. This is done at such a temperature as to prevent the etching of the substrate with hydrogen which is normally done at temperatures of approximately 1500°C [149] compared to approximately 1200°C for the intercalation with hydrogen (see Appendix B.1). We refer to intercalated samples as quasi-free-standing (QFS). The QFS studied here are of 1 and 2 layer thickness i.e. QFS 1LG and QFS 2LG. The experimental procedure for the growth of these samples and the intercalation is described in Appendix B.1. Furthermore we use an established method of creating hydrogen intercalated samples which has been shown through the use of surface enhanced Raman scattering (SERS) to effectively passivate the surface silicon atoms, showing Si-H stretching modes [150].

5.2.1 Stiffness Measurements of Graphene on 4H-SiC

To measure the mechanical stiffness of the samples we employ differential UFM, described in section 2.3.2.2, to quantify the contact stiffness of the sample. However to get a first impression of the mechanical integrity of the as-grown and intercalated samples we first produce UFM stiffness maps. These images are purely qualitative but allow one to discern between different regions of mechanical stiffness and adhesion. We show the UFM images for as-grown, QFS 1LG and QFS 2LG in Fig. 5.10. Sample thickness' were verified through Raman spectroscopy mapping to determine the thickness on the terraces. It was assumed that verification of sample thickness in one area was valid for the whole sample as growth conditions were the same throughout.

From Fig. 5.10 we observe that the UFM signal changes drastically depending on the force applied to the sample. What is counter-intuitive is that as the force increases the UFM signal decreases, something that is typically associated with a lower value of the sample stiffness. We observe this effect in all three sample types studied here. What is also unusual about this sample is the extremely high piezo vibration amplitudes required to obtain a good quality ultrasonic response. Typically in other experiments with UFM the piezo is driven at a voltage of 3-5 V_{pp} compared to the 5-20 V_{pp} needed to obtain a good signal when imaging graphene on SiC. What is more, for our as-grown and QFS 2LG samples we are able to discern between the terraces and the step edges for low set forces however this contrast disappears as the applied force increases by even such a low amount as 10 nN. To understand the true mechanism of these processes we studied the effect of set force on the measured UFM signal at several set forces. The results of which can be seen in Fig. 5.11

In all of these samples we observe that there is at times a decrease in the sample stiffness at the step edge. This is due mainly to the fact that thicker graphene grows at the terrace edges than on the terraces. Indicating that the stiffness should drastically decrease. In Fig. 5.11 we see that there is also a contrast inversion in the UFM images going from a set force of 0 nN to 13 nN. To describe the plethora of unusual behaviour we observe in these samples we propose that during the UFM amplitude modulation cycle (see section 2.3.2.2)

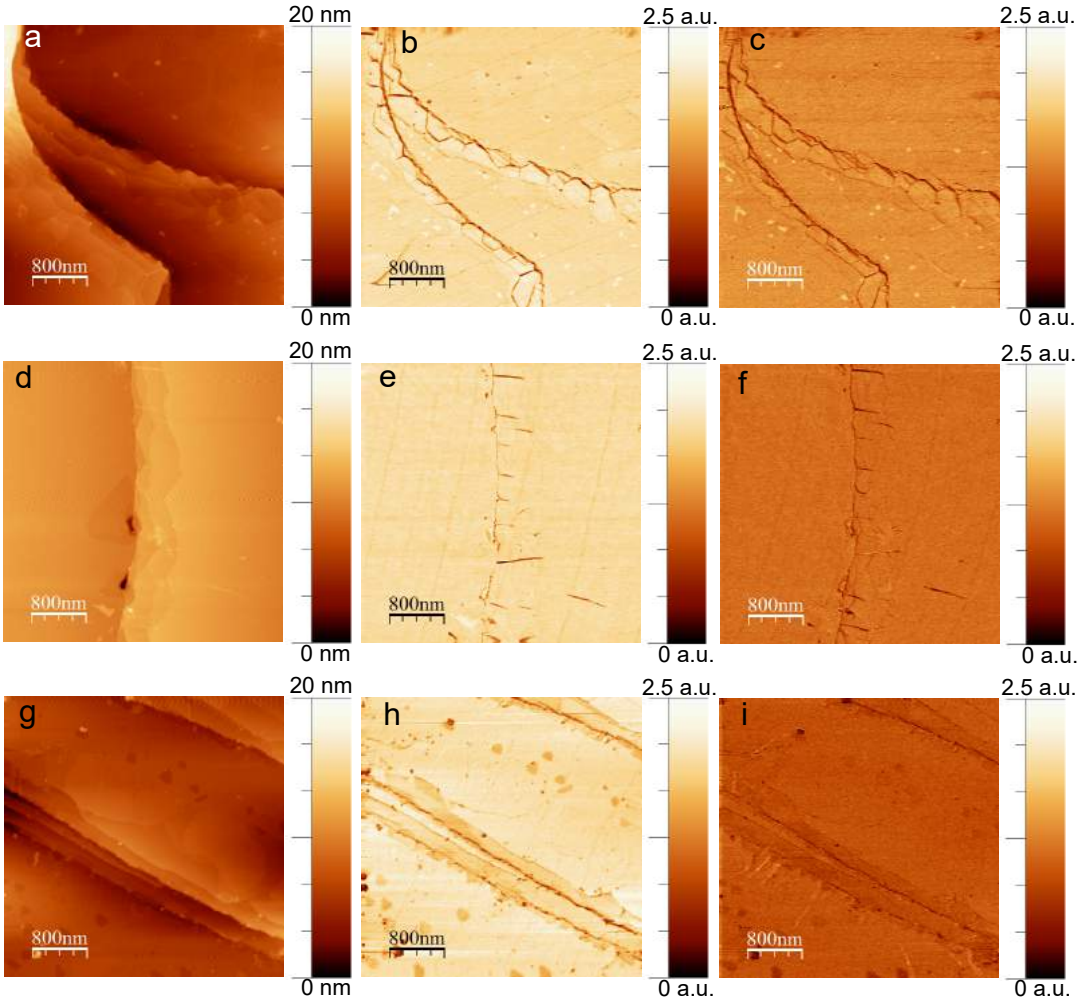

Figure 5.10: Images a-c are of our as-grown sample, d-f are QFS 1LG and g-i are QFS 2LG. Images on the left hand side show the topography of the region scanned, the centre column shows the UFM stiffness map of at a set force of approximately 0 nN and the UFM image in the right hand column show the UFM response at a set force of approximately 30 nN. Whilst all UFM images have been altered to show the same scale, the vibration amplitude (i.e. voltage applied to the sample piezo) to reach this response was different for each scan, they were the following: as-grown 5 V_{pp}, QFS 1LG 20 V_{pp} and QFS 2LG 10 V_{pp}.

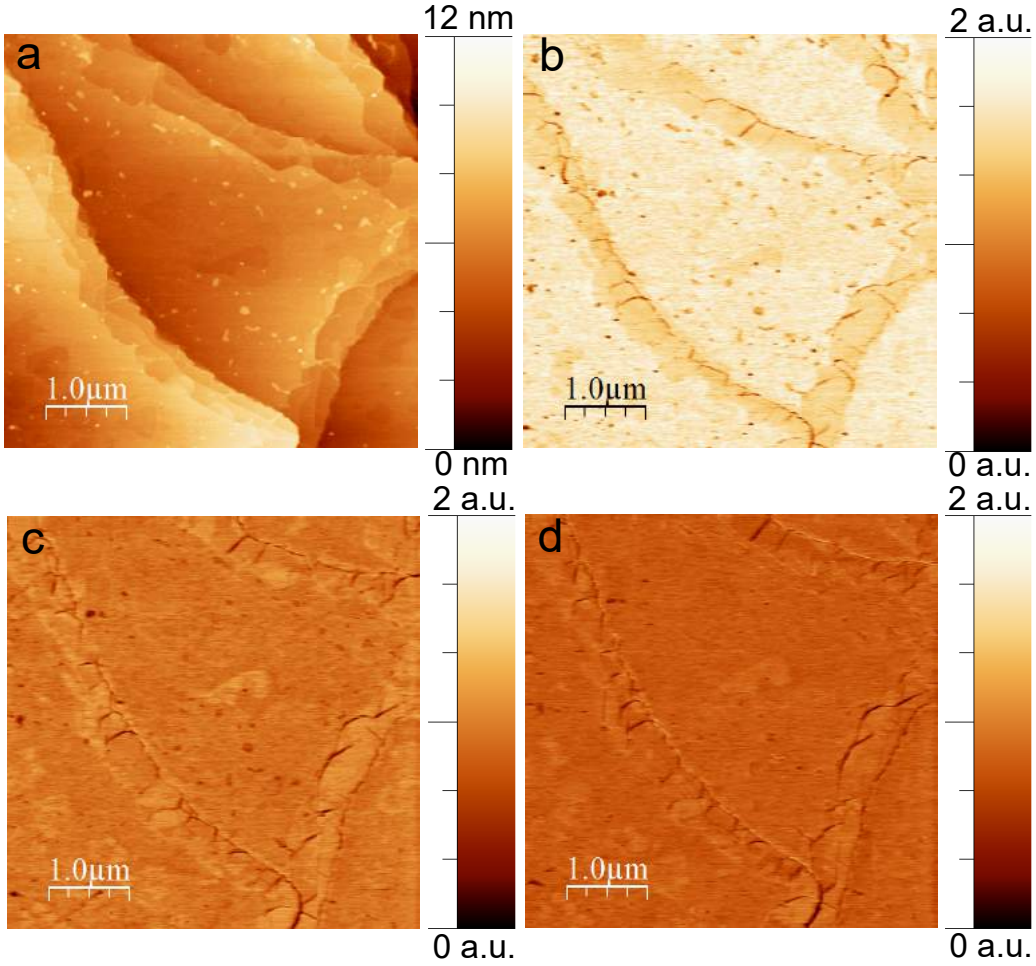

Figure 5.11: Image (a) shows the topography of an as-grown sample (IFL + 1LG) whereas images (b-d) are the UFM image of the same area for set forces of 0, 13 and 26 nN respectively. Brighter regions denote areas of a higher stiffness.

the tip is able to pull-up the graphene beneath the tip. This may explain the high sample vibration amplitude required to obtain a measurable UFM response however it does not explain the decrease in the UFM response for increasing set force. The reason for the decreased signal observed in UFM may in fact be due to indentation of the tip into the sample. This may be supported by the fact that we see a larger decrease in the UFM signal on the terraces (see Fig. 5.10) in QFS 1LG than as-grown and an even bigger decrease for QFS 2LG between set forces.

In addition to this we also note that there is a high level of adhesion between the tip and the sample. This can be seen when the tip approaches contact with the sample, eluding to an electrostatic nature. This high electrostatic adhesion may come from the polar nature of SiC, one would expect this electrostatic attraction to be shielded by the graphene however in our case the graphene was not grounded, nor was the cantilever highly conductive (silicon). As this electrostatic force was detectable when the tip was retracted ($\approx$15 μm above the surface) it became a question of when to adjust the AFM photodiode such that the total deflection was zero (i.e. defining 0 nN). To try to exclude any electrostatic forces we moved the cantilever far away from the surface ($\approx$1 mm) where the electrostatic forces were negligible. It is also worth noting that even though care was taken to ensure the force acting on the cantilever was accurate there will be electrostatic adhesion forces acting between the tip/cone of the cantilever and the sample, all of which will work to increase the effective contact force whilst not affecting the deflection of the cantilever. Finally we also mention that the long-range adhesion seen in particular with the as-grown sample was seen to vary significantly over the period of 20-30 minutes, for this reason the set force was recalibrated after each image.

To understand the mechanical stiffness of the samples studied, we employed differential UFM (see section 2.3.2.2). This method allowed us to measure quantitatively the local sample stiffness. One additional benefit to differential UFM is that effects of local sample adhesion should not affect the stiffness measurement as long as the adhesion remains constant throughout the measurement process.

The measurements themselves were taken at a series of points on two different areas of the same sample. The samples studied were as-grown, QFS 1LG and QFS 2LG. The results of which can be seen in Fig. 5.12.

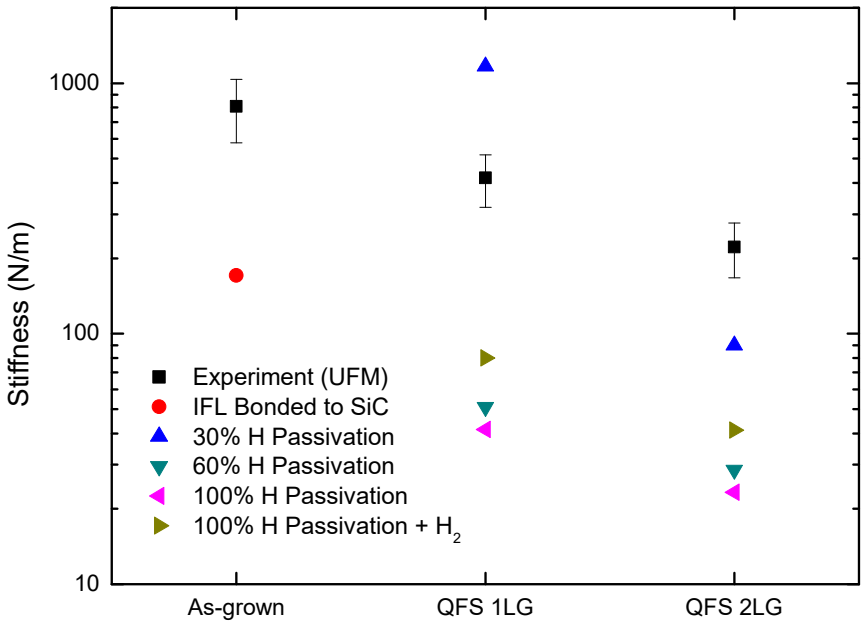

Figure 5.12: The measured and simulated stiffness measurements for the three types of sample in this study, as-grown, quasi-free-standing 1 layer graphene and quasi-free-standing two-layer graphene. Stiffnesses measured by differential UFM are shown in black and compared to theory for the following cases: IFL bonded to the substrate with 1LG on top (red), 30%(blue), 60% (green) and 100% (pink) of the silicon-carbon bonds replaced with Si-H bonds, in addition to this the case of 100% passivation with hydrogen with a layer of H_2 molecules between the substrate and the first graphene sheet, all theoretical values were obtained from calculations performed by Z. Y. Mijbil.

From Fig. 5.12 we note that the as-grown sample is the stiffest of the three types studied, this makes sense intuitively as the interfacial layer is still bonded to the substrate. By effectively decoupling the IFL from the substrate, creating a bilayer sampl,e the stiffness is greatly decreased (QFS 2LG) due to the out of plane elastic stiffness of graphene (≈40 GPa). We also note that the stiffness of QFS 1LG is stiffer than QFS 2LG, this may be due to the added 'spring' that is the graphene interlayer interaction. By comparison with theory we notice that there is a consistent underestimate of the measured stiffness compared with experimental values.

The origin of the discrepancy between theory and experiment may have its roots in several places. Firstly it is worth considering the method by which the theoretical values are calculated. These were calculated through density functional theory (DFT) where the simulated graphene sheet was pushed into the SiC or $SiCH_x$ and the total energy of the system measured. From here the energy of the system as a function of the separation was calculated by fitting the data quadratically and extracting the spring constant k as $E = kx^2/2$. If more than one graphene sheet was involved each interaction was probed separately and then the effective spring constant of the whole system was derived through $1/k_{eff} = 1/k_1 + 1/k_2 + ... + 1/k_n$. This method means that the effective stiffness was calculated where the spring behaved linearly. To measure this overall stiffness differential UFM measurements were performed between 0 and 30 nN approximately, this may have been beyond the linear response region of the system. In addition to this we suggest that the forces acting at the tip may have actually been much greater than the 0-30 nN we estimated from the deflection of the cantilever, this again would suggest that the stiffness values have been derived at different levels of applied force.

In comparing the measured stiffness values for QFS samples to the theoretical we see a similar trend in the decrease in stiffness going from QFS 1LG to QFS 2LG.

To conclude, the stiffness measurements of graphene on intercalated on SiC we see a considerable decrease in the sample stiffness going from as-grown to QFS 1 and 2LG. We attribute this to the decoupling of the substrate and graphene, something that has been found to greatly improve the electrical properties of

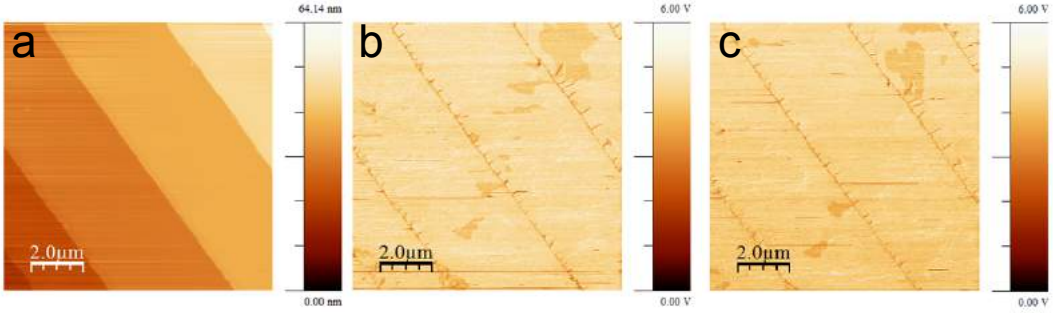

Figure 5.13: Images taken of QFS 2LG where image a) shows topography, image b) shows the UFM image where darker regions correspond to more compliant. Softer areas are thought to be due to pockets of excess hydrogen. Image c) is UFM of the same area as the centre image but taken approximately after another 1 hour of scanning.

graphene. Despite this decoupling we still see a relatively high level of support provided by the sample with stiffness' measured approximately between 100-200 Nm^{-1}. This may well prove to be a characteristic that will be important for the mechanical integrity of future electronic devices based on graphene grown on SiC.

5.2.2 Trapped Pockets of Hydrogen Beneath SiC

Upon analysing the images of our intercalated samples we observe pockets or areas of decreased stiffness. These regions also appear to sometimes be accompanied by a small increase in topographical height as can be seen in Fig. 5.13

It is however not always true that these softer regions are accompanied by an observed topography signal. In Fig. 5.13 we see that the softer regions are not stable in time and are free to either move or for the excess hydrogen to escape through some other mechanism. The size and number of these pockets was found to be greatly reduced by cleaning the samples gently and mechanically with a clean room wipe in IPA/Acetone. The change in height measured is only very small and was typically in the region of 3-8 Å. Initially these regions of decreased stiffness were presumed to be areas of intercalation compared to the majority of graphene bonded to the substrate however this theory was discounted after the observation of the movement of such regions over relatively short time scales, seen in Fig. 5.13.

One point of interest is the fact we do not always see a corresponding increase in the topography signal when we observe these regions with UFM. This could mean that the increase in height is there but below the detectable limit of the AFM or that these compliant pockets fall into two distinct categories. What is more, we observe both kinds of pockets in our QFS 1LG and QFS 2LG samples, ruling this out as the cause. The heights observed in these pockets ranged from 0.5-1.5 nm in height, where typical topographical and UFM maps can be seen in Fig. 5.14.

Upon further inspection of the pocket of decreased stiffness seen in Fig. 5.14 we observe smaller triangular regions within the region that are both lower in height but show up as stiffer in the UFM maps of Fig's 5.14b,c. This is different from the pockets where we observe no detectable height change where no such triangular regions are seen. The images shown in Fig. 5.15 illustrate this difference.

There are two proposed hypotheses as to why we only observe a height difference in some regions. The first proposal is that they are actually pockets of H_2 gas trapped beneath the graphene and the SiC or between graphene layers, the only difference is the amount of H_2 that is trapped dictating the height of the pocket. The second hypothesis is that they are actually two distinct regions such as areas where the level of hydrogen intercalation is higher. Whilst we can not say definitively due to the lack of data available, we believe that the strongest hypothesis is that these regions are both pockets of trapped hydrogen but where the pressure is lower meaning that the bulge produced is below the detectable limit to our AFM $\approx$0.1 nm. This however does not explain the absence of the triangular indentions that we observe. It may turn out that these triangular depressions are in fact the cause of the measurable increase in height. To try and understand if these triangular regions are connected to the hydrogen pockets observed we now turn our attention to them.

One additional suggestion as to the cause for the two different types of 'areas of decreased stiffness' was the presence of debris on the surface of the sample. However after imaging several samples that had been unattended for long periods we found different characteristics to the pockets of hydrogen seen in Fig's. 5.13,5.14 and 5.15 which were present on relatively clean samples. The dirtier

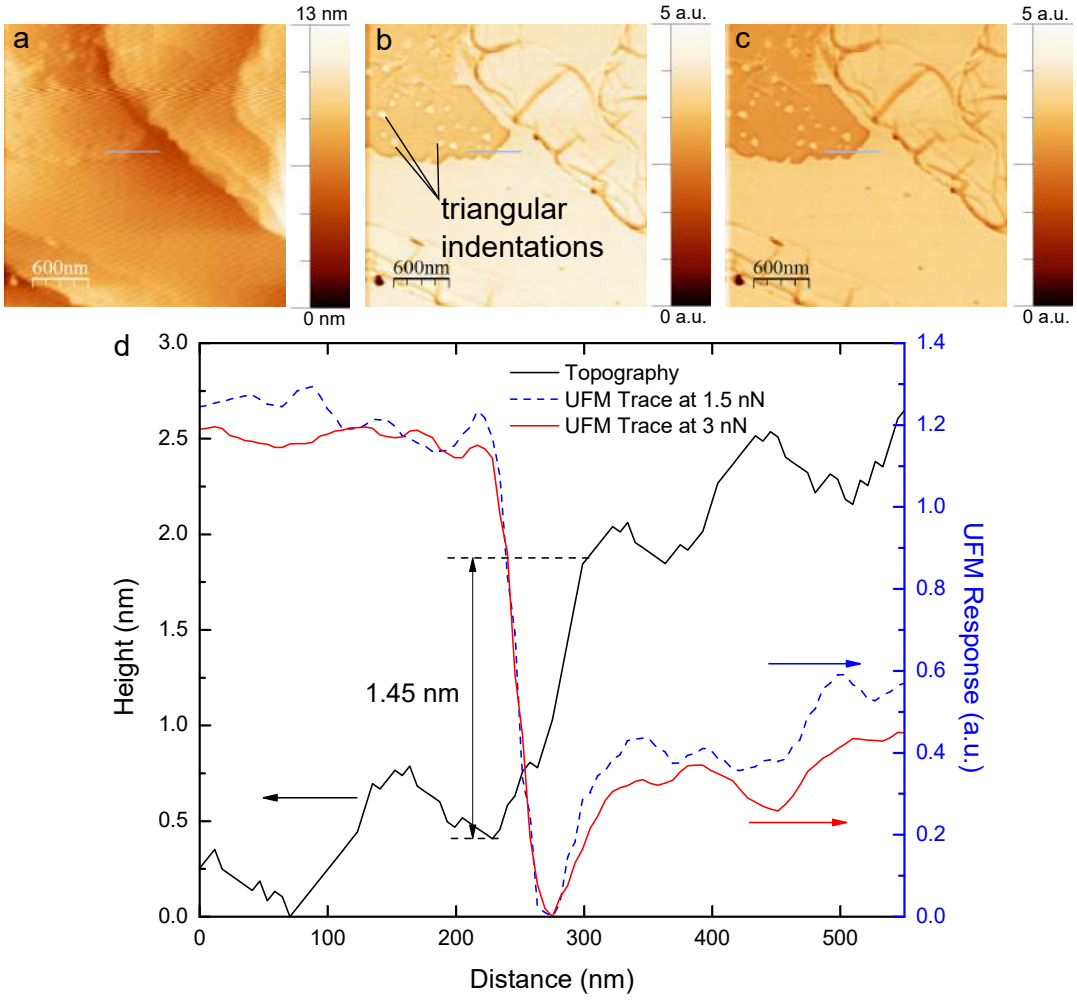

Figure 5.14: Image a) shows the topography of the region of a sample of QFS 1LG where we clearly see a raised region between the step edges. Images b) and c) are UFM images taken at set forces of approximately 1.5 and 3 nN. The graph in d) shows the profiles illustrated in blue in images a-c) where we see that the height difference is approximately 1.45 nm and corresponds to a measured decrease in the UFM signal. Both UFM images were taken virtually simultaneously where one was taken on the trace and the other on the retrace of the image.

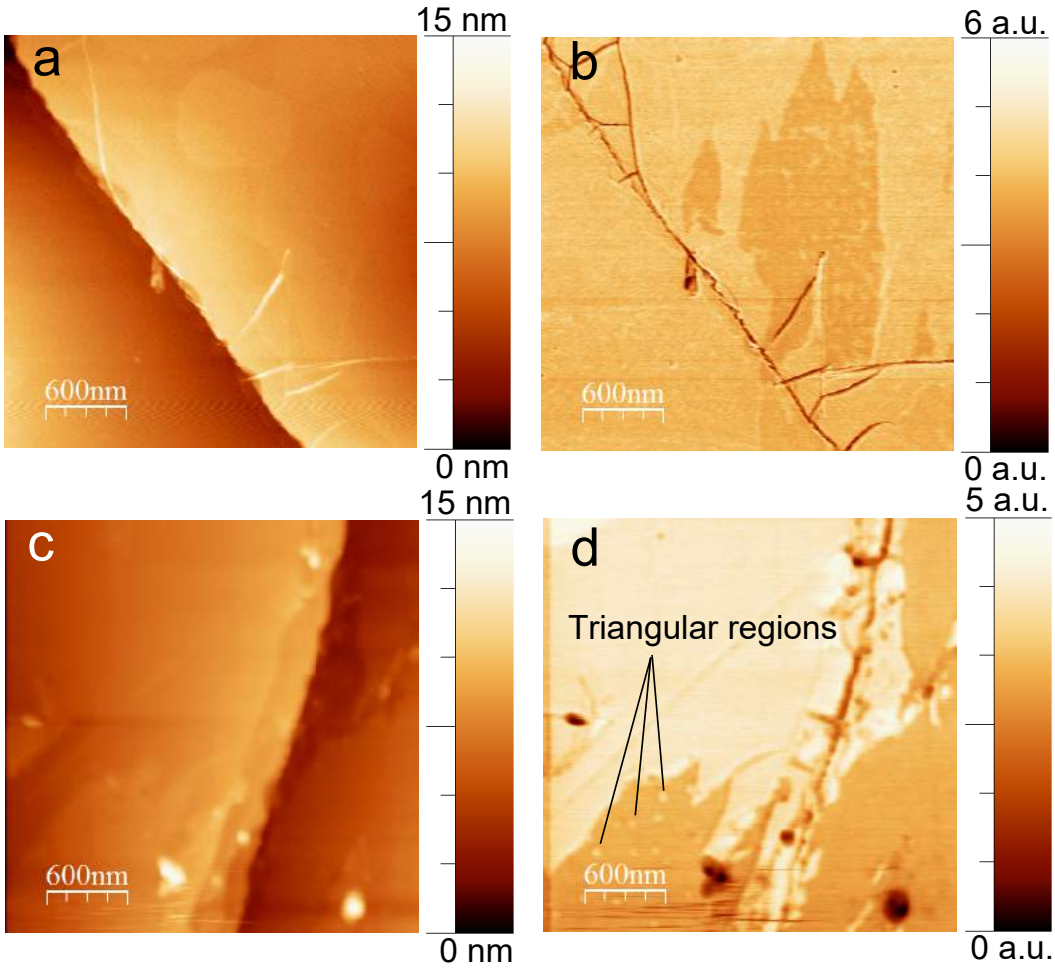

Figure 5.15: The two different types of areas of decreased stiffness observed. Images a) and b) correspond to the topography and UFM of QFS 2LG where the area of decreased stiffness shows no corresponding detectable change in the height. Images c) and d) show again the topography and UFM images of QFS 2LG but of an area where we observe a difference in the topography corresponding to the decrease in the UFM signal. The set force applied in images a) and b) was between 0-6 nN whilst the set force in c) and d) was approximately 2 nN.

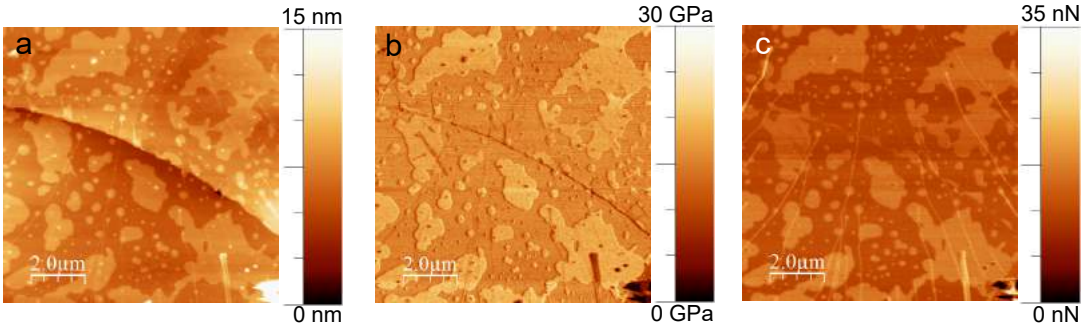

Figure 5.16: Debris seen on QFS 1LG where images a,b and c) denote the topography, stiffness measured through quantitative nanomechanical mapping and tip-surface adhesion respectively. The height of the debris was found to be 1.75-2 nm across the entire surface.

samples showed streaks that ran along the slow-scan axis from the tip pushing pieces of debris around, typical of most dirty AFM samples. In addition to this we observed an unusual kind of contamination, the results of which can be seen in Fig. 5.16

The source of this debris is unknown and what is more striking is that the thickness across all contaminated areas is approximately 1.75-2 nm. It is not thought to be the salol that bonds the substrate to the piezo as this is highly crystalline and one would be able to discern specific orientations. As the contamination is measurably stiffer than the surrounding SiC we are unable to comment on its nature or origin.

5.2.3 Triangular Indentations

The fact that these regions are nearly always triangular indicates that they may have their origins in the crystallographic structure of the substrate. We also notice that these triangular regions correspond to a decrease in the height compared to the pocket of gas. We propose that these triangular regions are where the top graphene layer is attached to the substrate. To understand the mechanical nature of these regions we employ FMM as well as UFM, this gives us a sensitivity to a large range of stiffness' and may help to unravel their nature seen in Fig. 5.17

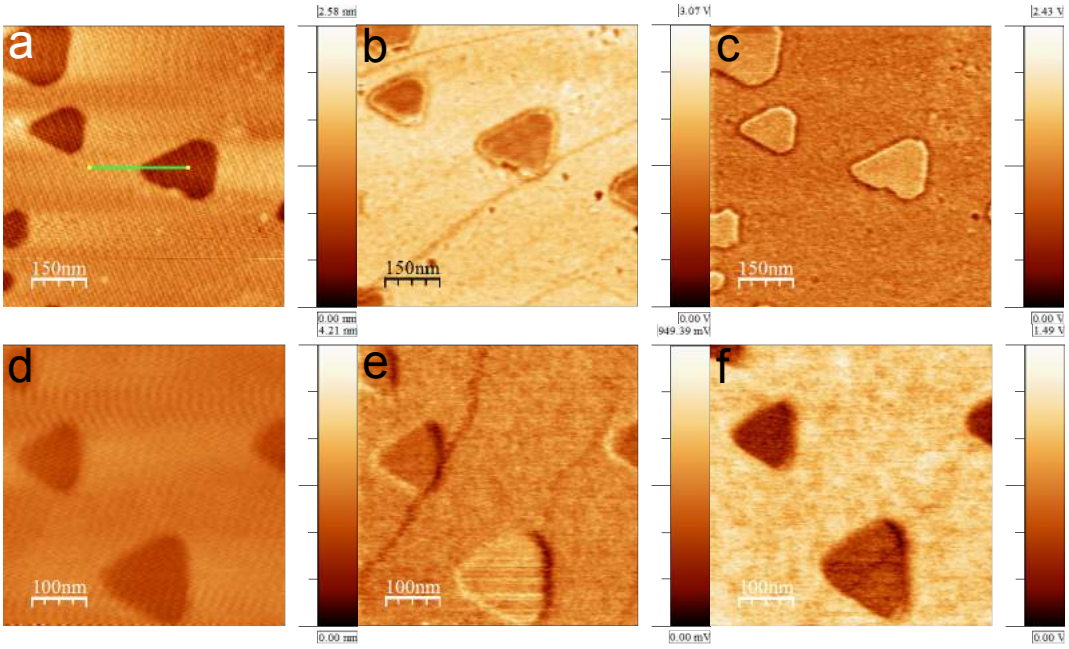

Figure 5.17: In this image we show the triangular depressions seen on the terraces of QFS 2LG. Image a) shows topography where the height difference along the green trace taken is approximately 0.8 nm. Image b) shows UFM at a set force of -6.5 nN and c) UFM taken at 33 nN. Image d) again shows topography of a similar region taken in conjunction with FMM image at e) -5 nN and f) 33 nN.

From Fig. 5.17 we see that the behaviour of the depressions under FMM and UFM varies drastically with varying set force. We should also point out the height of the depression was not found to vary detectably between the set forces used (-5 and 33 nN). With both UFM and FMM we notice a contrast inversion when going from a negative set force to a higher positive set force. Upon closer inspection we notice that the absolute signal on the depression does not tend to vary much with set force whilst the signal on the surrounding area changes. Interestingly the stiffness on the surrounding areas decreases for increasing set force according to UFM whilst increases according to FMM measurements. This qualitatively makes sense as with UFM the higher the set force the greater depth at which the tip indents into the sample resulting in a higher vibration amplitude needed to reach the non-linear region and detach from the surface, resulting in a lower signal. This explains why the UFM signal decreases in the region around the depression. As the UFM signal was not found to change drastically on the triangular depression we propose that the tip was not able to indent a significant amount due to the region being much stiffer. This may suggest that the triangular depressions are either SiC or regions where there is still an interfacial layer bonded to the substrate. The FMM data supports this as it does not measure indention like UFM but the effective spring constant of the sample, which as one would expect increases with increasing set force.

To understand further the properties of these depressions we employ frictional force microscopy (FFM). We probe the frictional forces on the cantilever by taking the trace-retrace both with ultrasound on and off, to see if these high frequency vibrations will affect the friction in an unusual way.

From Fig. 5.18 we see that the application of ultrasonic vibrations to the sample decreases the overall friction seen by the tip, this is an effect known as ultrasonic induced lubricity and originates in the tip periodically detaching from the surface[151]. The friction is considerably lower on the depression than it is on the surrounding areas and as graphene has a very low coefficient of friction this would at first make it unlikely that the depression is SiC or SiC terminated with hydrogen. Instead we propose that the difference comes from the increased mechanical stiffness which effectively decreases the contact area with the tip and thereby the frictional forces acting on it. To try and obtain a better understanding

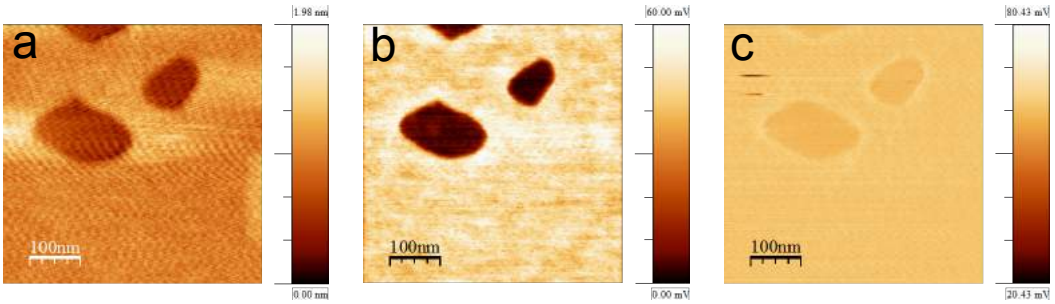

Figure 5.18: Image a) shows the topography of depressions seen in a QFS2LG sample, b) absolute frictional force acting on the tip c) frictional force acting on the tip with ultrasonic vibration applied to the sample. Lower signal in this case indicated a lower frictional force.

we study the application of several other methods such as KPFM, the results of which are seen in Fig. 5.19, the results of which were taken by Christos Melios in preparation for the publication of these results.

In Fig. 5.19 we see that both the step edges and the triangular indentations show an increase in the work function, this is to be expected for thicker material but is surprising for the triangular indentations. The adhesion data also shows lower attraction between the cantilever and the triangular regions, this is in agreement with a higher UFM signal seen when applying a positive set force as seen in Fig. 5.17. By observing the adhesion and deformation, both contributing factors to the UFM signal, independently will be able to determine the mechanical properties of these regions.

5.3 Summary

The study of the nanomechanical properties of 2D materials in this chapter was in two parts. Firstly we studied the application of ultrasonic probe techniques (UFM and HFM) to studying large stacks of 2D materials, something of importance for understanding the behaviour of complex heterostructures. Secondly we applied the knowledge gained in the first part to graphene grown on 4*H*-SiC and how we can detect the nature of the interaction of the graphene with the substrate with various levels of hydrogen intercalation.

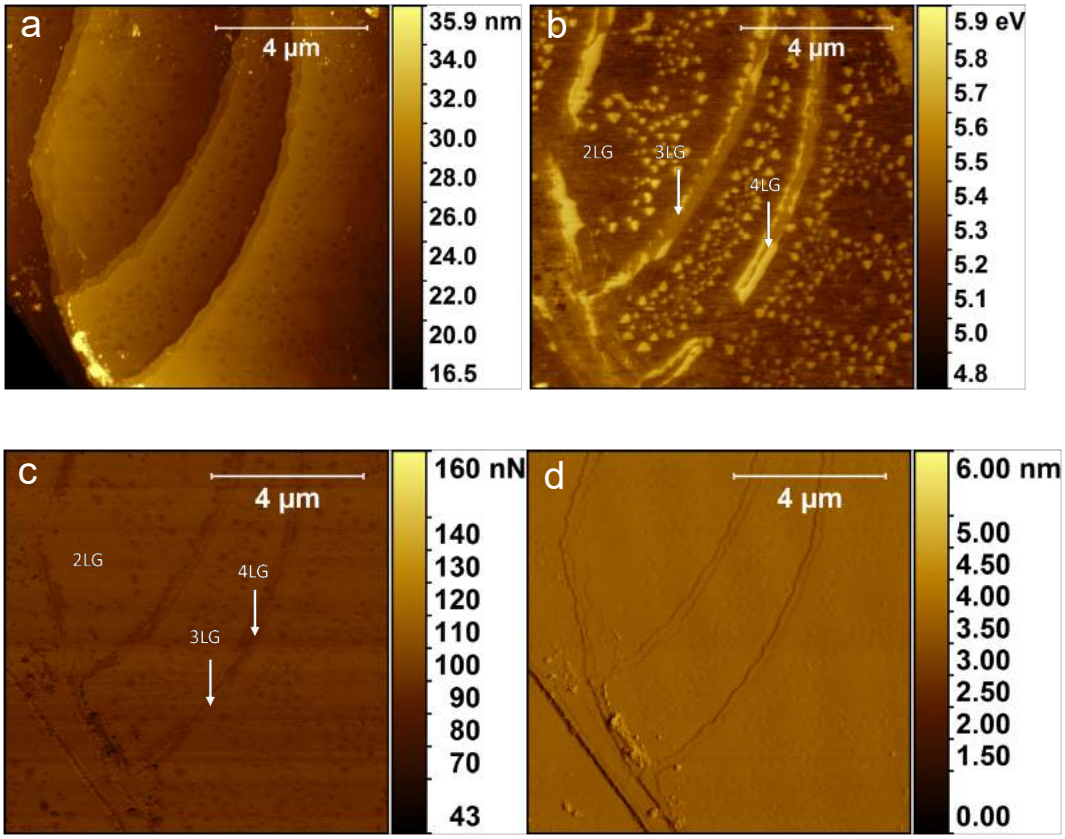

Figure 5.19: Image a) shows the topography of depressions seen in a QFS2LG sample, b) work function measurements of the same sample showing the terraces with bi-layer graphene and the step edges with a mixture of 3 and 4 layer graphene. Image c) shows the adhesion obtained through quantitative nanomechanical mapping for the same region, showing that both the triangular regions and thicker material on the step edges gives lower adhesion. Finally image d) shows a deformation map indicating that there is no appreciable difference in the mechanical stiffness between the thicker material on the step edges of the triangular regions.

Our studies in the first section show how the transversely isotropic properties of 2D materials, that is low out of plane stiffness, can enhance the lateral and depth at which one can probe beneath the surface. We demonstrate through numerical calculations that a low out of plane stiffness and a low interlayer shear modulus mean that the stress field produced by the AFM tip penetrates far beneath the surface and is effectively 'focused'. The implications of this are that one can easily detect subsurface anomalies in complex heterostructures which may compromise device performance.

In the second larger section we have applied ultrasonic techniques to study graphene grown on 4*H*-SiC where we measure the mechanical decoupling of the graphene from the substrate through intercalation with atomic hydrogen. It was found that the intercalation with hydrogen removes the covalent bonding between the graphene and the substrate and is replaced with a van der Waals interaction, reducing the strength of the mechanical interaction between the two, an observation that is consistent with other studies[152]. Through collaborative work we were able to link the electronic decoupling of the graphene and the substrate with a degree of mechanical decoupling. However even though we have lost a degree of mechanical support the graphene does not appear to wrinkle or show other signs of non-uniform stress distributions which may impede electronic performance. From this we suggest that an adequate amount of support remains, something that is ideal for the fabrication of electronic devices from such a material. We were also able to probe the mechanical properties of graphene grown on silicon carbide and found that after the hydrogen intercalation process small pockets of the gas remain trapped both between the substrate and the graphene and between adjacent layers of graphene if they were present. These remnant pockets of gas were not stable and could be moved with the AFM tip, cleaning or by being left over long periods. Finally we conclude this chapter by studying a series of triangular indentations observed in the silicon carbide, something that has not received a great deal of attention in literature. We show that these triangular indentations are mechanically and tribologically different from graphene on silicon carbide which may suggest that they are either bare silicon carbide or at least where the graphene layer is still partially bonded to the substrate.

This claim is further supported by observing the triangular regions in the middle of a trapped pocket of hydrogen through an increase in the stiffness. The presence of these triangular depressions may be detrimental to the performance of devices fabricated from such a substrate and would need to be addressed in future. Nonetheless graphene grown on 4*H*-SiC intercalated with hydrogen provides a promising route to the large-scale, high-quality and economic production of graphene devices.

Chapter 6

Nanoelectromechanical Phenomena

6.1 Imaging NEMS Like Devices with Direct Contact Electrostatic Force Microscopy

In this section we describe the work performed to characterise the level of electrostatic interaction the substrate has with the probe and the graphene or other 2D-material sample. To do this a method of dynamic contact electrostatic force microscopy (DC-EFM) was used. This method has been reported elsewhere [104, 105]. The benefits of this technique are that the tip remains in contact with the surface during the duration of the scan allowing one to monitor mechanical, electrical and electromechanical phenomena on the nanoscale. Results presented in this section were also published elsewhere[153].

An Agilent function generator is used to provide an AC+DC bias between the tip and the sample which for the purposes of this study were in the range of $-5 < V_{DC} < 5$ V whereas V_{AC} was typically 5 V. The frequency used is typically in the region of a few kHz, this is a high enough frequency to avoid any interaction with the feedback system but also low enough to not excite any resonance behaviour of the cantilever ($f_0 \approx$13 kHz). As is described in section

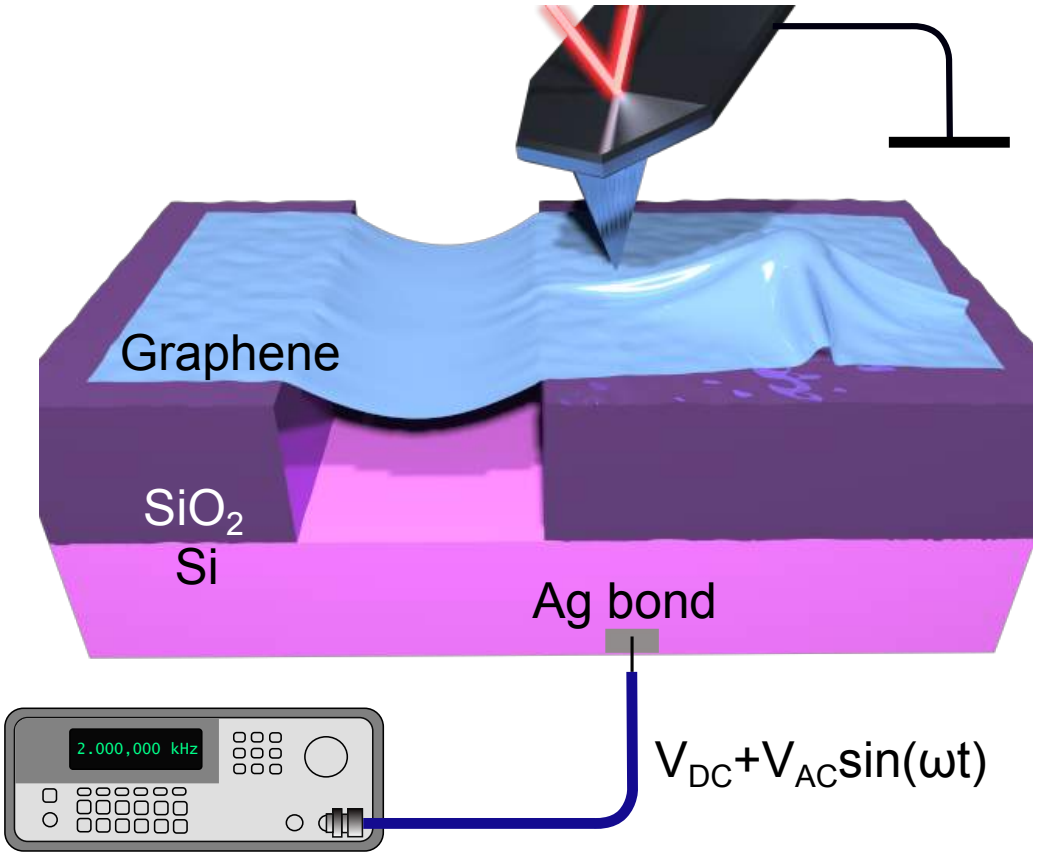

Figure 6.1: The experimental setup used for the purposes of detecting the electromechanical phenomena in graphene NEMS resonator-type devices. The graphene or other 2D material is suspended over a trench typically 250-300 nm wide etched into the Si/SiO_2 substrate. The silicon is electrically contacted by scratching away the oxide layer from underneath and attaching a small wire with Ag paint. We also ground the electrically conductive cantilever (Cr/Pt/Ir coated).

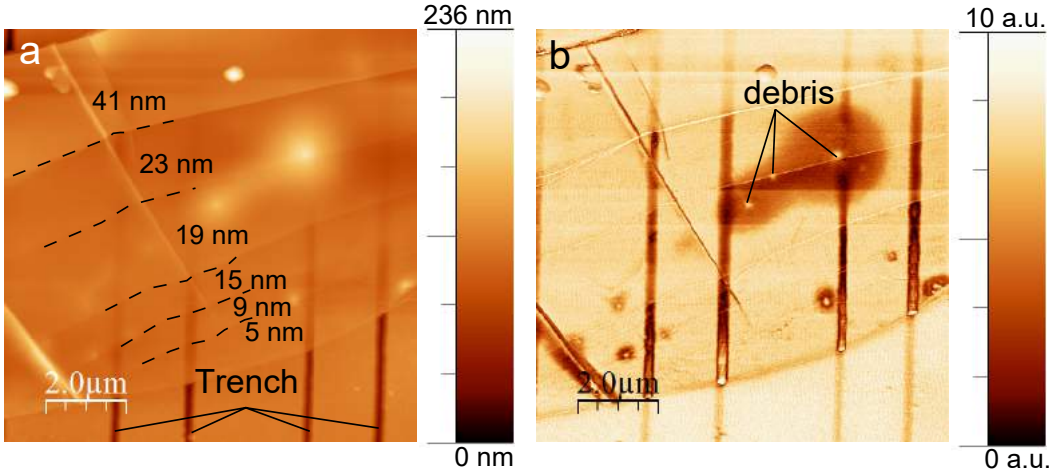

Figure 6.2: Image a) shows the topography of a MLG/thin graphite sample where the flake has cleaved in such a way as to leave terraces of different thickness, we quote the step thickness' as 5, 9, 15, 19, 23 and 41 nm thick. We also point out the locations of the trenches running vertically in the image. Image b) shows the corresponding DC-EFM image where brighter regions denote a higher signal obtained from the vibration of the cantilever at the frequency at which V_{AC} is applied (2 kHz). The static force applied by the cantilever is approximately 4-5 nN and the V_{DC}=4 V whilst V_{AC}=5 V. We also show what we believe is debris trapped beneath the surface located labelled in image b).

2.3.3.2 there is a DC component to the electrostatic force on the cantilever, in addition to this there are components at ω and 2ω; for the purposes of this study we are detecting the component at ω only.

6.1.1 Contrast Mechanism

As the cantilever used is conductive (Veeco Model SCP-PIC, Sb doped Si (0.01-0.025Ω) coated with a bottom layer of Cr (3 nm) and a Pt/Ir (20 nm) top layer) so the graphene sample is also grounded and therefore any suspended regions of a graphene film, such as those over the trenches etched into the substrate, are free to oscillate. When scanning the cantilever over these trenched regions we notice that the signal can be either higher or lower than the surrounding substrate. This was found to depend on either the value of V_{DC} used or the thickness of the flake (see Fig. 6.2).

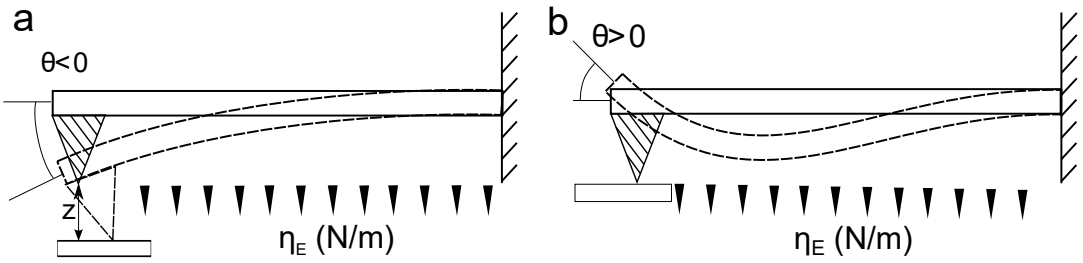

Figure 6.3: Two competing cantilever bending mechanisms in DC-EFM. Image a) shows the case when the sample is moving beneath the tip either due to electrostatic actuation or through sample compliance, the change in the cantilever angle θ is negative in this instance. Image b) shows the mechanism of bending where the sample is sufficiently rigid and behaves as a pivot point where the change in the angle is positive.

To understand the origin of the contrast in DC-EFM in Fig. 6.2 we study the response of the system whilst imaging the MLG suspended over the trenches, this gives us the greatest source of variation in the DC-EFM signal. Upon close inspection we notice that the DC-EFM signal on the suspended material is comparable to that of the supported for the region of 41 nm thickness, where it is essentially graphite. However whilst the signal on the supported MLG/graphite varies little for changes in thickness we see a decrease in the DC-EFM signal as the thickness decreases to a point, where the thickness is 5 nm at which point we see the signal increase again. The mechanism we propose for this dependence on thickness is that there are two bending mechanisms of the cantilever; one which will dominate for stiff samples (thicker MLG/graphite) and one which dominates for thinner MLG seen here at 5 nm thickness. The proposed mechanisms are seen in Fig. 6.3.

In Fig. 6.3 we see that the two different bending mechanisms provide opposite angles of deflection. As the atomic force microscope is sensitive directly to the change in angle at the end of the cantilever, not absolute deflection, the two bending mechanisms in Fig. 6.3 will compete against one another. We therefore propose that for a specific sample thickness the bending from both mechanisms may cancel out to yield a null signal.

The source for the bending illustrated in Fig. 6.3a is hypothesised to be a combination of the decreased mechanical stiffness of the sample beneath the

tip and the electrostatic actuation of the suspended MLG. To approximate the amount of electrostatic actuation present for such a system we use the simple approach shown in section 2.2.1. Here we see that for a system of 5 nm thick MLG the peak-peak vibration amplitude would be in the region of 0.1 nm. This is just above the detection limit of the AFM but rather low. To understand how the vibration of the sample contributes to the overall signal qualitatively we use the following two expressions Eq's. 6.1 and 6.2[153] to estimate the contributions to the total DC-EFM signal

$$\alpha_C = \frac{\eta L^3}{48EI} \tag{6.1}$$

$$\alpha_z = -\frac{3\delta_c}{2L} \tag{6.2}$$

Where α_C and α_z are the angles of deflection when a clamped-pivoted cantilever of length L is subjected to a force distribution $\eta(\mathrm{Nm}^{-1})$ and a point deflection at the tip δ_c. The symbols E and I denote the elastic modulus and second moment of area with respect to the axis across the trench. The total signal can then be written as the sum of Eq's. 6.1 and 6.2 to give Eq. 6.3.

$$\alpha = \frac{\eta L^3}{48EI} - \frac{3\delta_c}{2L} \tag{6.3}$$

It should also be pointed out that the signal observed by the AFM is actually twice the change in the angle observed at the end of the cantiever[154] due to the fact that the laser light is reflected from the surface and is not emanating from it. In Eq. 6.3 the movement of the tip δ_c corresponds to both the actuation of the sample and the flexing/indentation of the sample due to the force from the cantilever. We therefore can write δ_c to accomodate this as can be seen in Eq. 6.4.

$$\delta_c = \frac{1}{k}\frac{dC}{dz}V_{total}^2 + \frac{3\eta L}{8k'} \tag{6.4}$$

Where k is the spring constant of the suspended sample in response to a distributed load from the capacitive forces. The spring constant k' is of the suspended sample in response to a point load. The first term in Eq. 6.4 represents

the contribution from sample electrostatic actuation, the second term corresponds to the indentation of the tip from the distributed electrostatic load acting on the cantilever η. It is worth mentioning that the factor of 3/8 in the second term of Eq. 6.4 originates in the relation of a distributed load over the length of the cantilever to a point load acting at the tip[155]. As an approximation for the contributions to the total deflection seen by the AFM tip we equate the first term in Eq. 6.4 to be 0.1 nm and the second term is estimated at 0.05-0.1 nm by taking $k' \approx$20 Nm^{-1} and $\eta L \approx$3 nN. This shows that for the experimental conditions described both the beam bending due to flexing of the sample from the cantilever and electrostatic actuation of the sample are indeed comparable. We also note that the DC-EFM signal is still very weak even for high values of V_{DC}=V_{AC}=5 V, this adds further evidence to the fact that we are detecting cantilever vibrations on the order of 0.1-0.2 nm. We should also add that whilst our analysis and calculations give a certain degree of evidence towards the case that we are in fact detecting the actuation of the MLG resonators, we cannot say that it is a foregone conclusion as there are a great many effects that may affect the actuation of the graphene such as damping both from the ambient environment and from the AFM tip itself.

One other mechanism that may affect the DC-EFM signal is sample friction. This has been shown to be an appreciable effect in FMM where working at high-amplitudes is commonly avoided to reduce the effects of friction[156]. To test whether this is the case with DC-EFM, we study the signal as a function of set force and back-gate voltage for both graphene on SiO_2 and SiO_2 (see Fig. 6.4), materials with two very different coefficients of friction [136].

Clearly from Fig. 6.4 it can be seen that for SiO_2 and graphene the difference in the response at varying set forces for F <100 nN are minimal and only becomes apparent as a decrease in the response at higher values of V_{DC}. It is not apparent what is happening at F=100 nN as whilst there is a difference in the response at higher force, the signal is also more rounded close to the voltage required to nullify all static voltages and charge $V_{DC,n}$ and is more parabolic in shape.

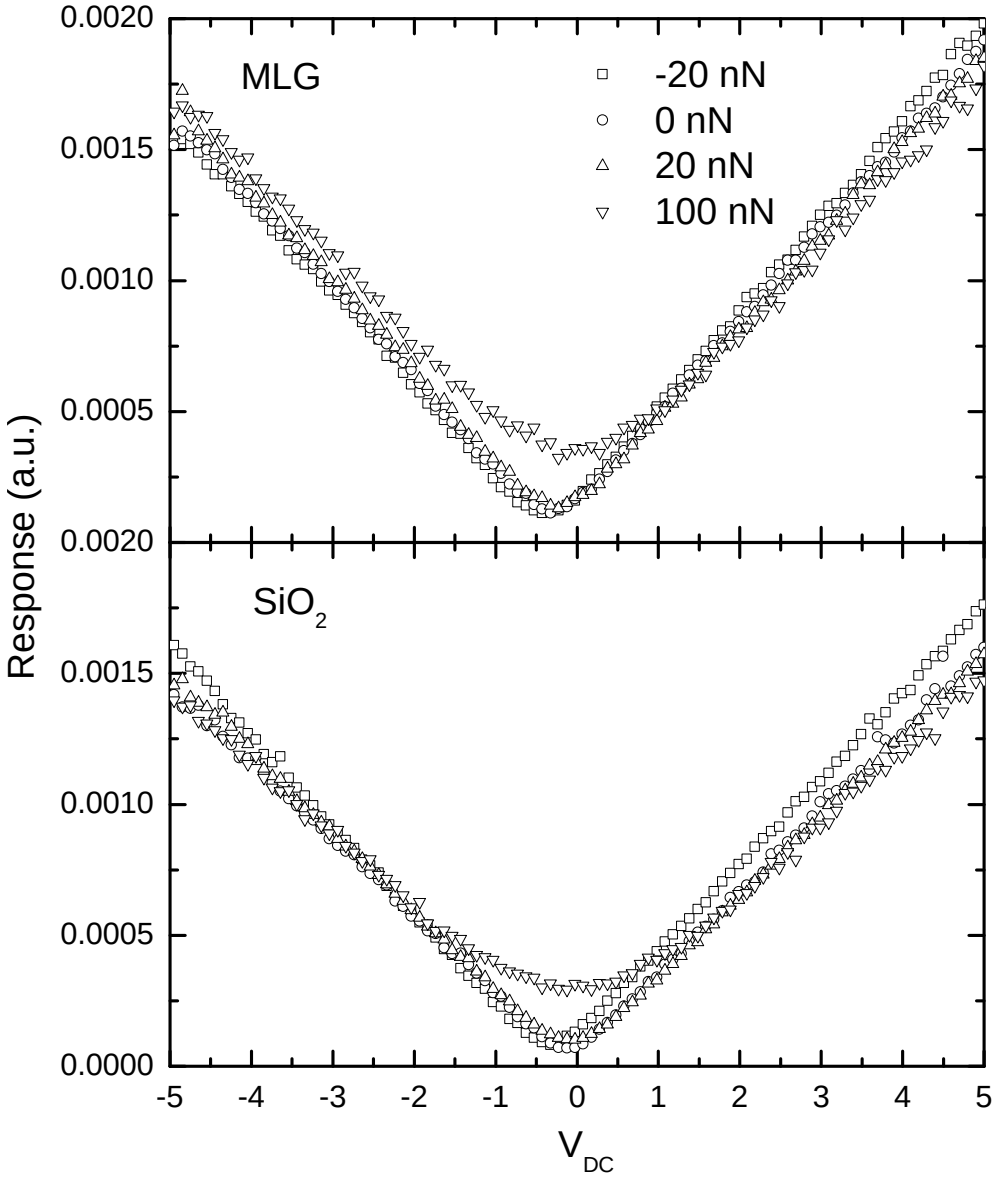

Figure 6.4: Top image shows the response of DC-EFM where the tip is resting on MLG on top of SiO_2 substrate. Bottom image shows the response of DC-EFM to sweeping the back gate DC bias whilst in direct contact with the SiO_2 substrate. All measurements were taken whilst maintaining an V_{AC}=5 V and the measured response is at the driving frequency ω=2 kHz.

6.1.2 Detecting Subsurface Charge Density Beneath Graphene

The fact that sample stiffness plays a role in the DC-EFM signal does not mean that certain electrical properties cannot be found. Even if the graphene actuation only accounts for a small portion of the DC-EFM signal it is possible to infer local properties of the sample such as the surface potential/charge density. By sweeping the back gate voltage and locating the null voltage $V_{DC,n}$ we can find the point at which the applied back gate voltage is equal and opposite to all other sources of voltages or charges at the sample. The main factors that may contribute to the null voltage are the contact potential difference V_{CPD} between the tip and the sample, charge transfer and other surface charge density. One can easily measure the work function and charge transfer of a sample through conventional non-contact EFM. Non-contact EFM also allows the user to detect surface charge density however this method falls short when we seek to measure the surface charge density of the substrate beneath graphene, a conductive layer that effectively shields any effect of the charges to the cantilever. In order to access the density of these charges we use the electrostatic actuation of the graphene suspended over the trench. By imaging the same scan line repeatedly and periodically changing V_{DC} we are able to observe a difference in $V_{DC,n}$ for the supported and suspended regions, see Fig. 6.5.

In Fig. 6.5 we see that $V_{DC,n}$ is approximately 1.5 V lower for the suspended region than it is for the supported region. As this difference is due largely to the charges beneath the graphene layer we can use it to estimate the charge density beneath the layer. Hong *et.al* provided a way of estimating the surface charge density beneath a conductive probe at a distance d from the surface using Eq. 6.5[105].

$$\sigma = -2\epsilon_0 V_{DC,n} \left(\frac{\partial C}{\partial z}\right) \frac{1}{C} \tag{6.5}$$

Where $V_{DC,n}$ is the voltage required to nullify the DC-EFM signal, C is the cantilever/cone/tip capacitance. Where Hong *et.al* estimate the probe/sample as a parallel plate capacitor leading to the approximation that $(\partial C/\partial z)/C \cong 1/d$. By using the above approximation we estimate the surface charge densities

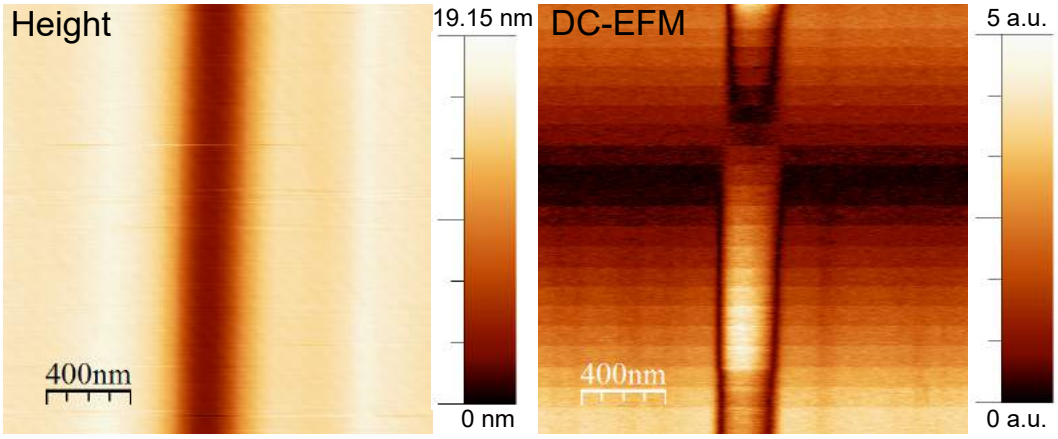

Figure 6.5: On the left is the topography where the dark central region is the MLG (7.5±0.5 nm) suspended over a trench of width 300 nm. Image on the right shows the DC-EFM amplitude signal where $V_{DC,n}$ varies from -5 V at the top of the image to +5 V at the bottom and is varied in 0.5 V steps. Both images were taken simultaneously where the AFM tip scanned the same line repeatedly. Set force $F \approx$10 nN, V_{AC}=5 V, Drive frequency ω=2 kHz. A Pt/Ir tip was used with a spring constant of k_c=0.15 N/m.

trapped beneath graphene and MoS_2 as; σ_{MLG}=-1.96±0.5 nC/cm^2 and σ_{MoS_2}=-2.45±0.5 nC/cm^2. In these calculations we take d as the distance between the tip and the underlying silicon therefore $d = d_1$=300 nm.

6.1.3 The Effect of Environmental Factors on the Operation of DC-EFM

Whilst performing many scans during the data taking process we noted that it was possible for the DC-EFM system to behave differently between samples and even on the same sample where the calculated surface charge densities would change from one scan to the next. We propose that the large variation in behaviour seen is due mainly to environmental factors such as temperature and humidity. One additional interesting behaviour that we observed involved the light used to illuminate the AFM samples that allowed us to align the cantilever with the sample. We notice that if one were to turn the light off mid-way through a scan then DC-EFM contrast could either disappear or be removed entirely, This may

suggest we are observing photo-excited characters that migrate into the SiO_2 and effectively increase the electrostatic force on the cantilever.

One other factor that we do not observe directly but is expected to affect the DC-EFM contrast is the size of the graphene flake used. The effect of the size is thought to be two-fold. Firstly the size of the flake will affect the total capacitance of the system, this is non-negligable as the size of the flake can be around 20-50 μm, comparable to the scale of the cantilever. Secondly the flake may shield a significant portion of the cantilever electrostatically. This effect may however be neglected if one were to use an electrically insulating cantilever.

One other explanation for the wide range of behaviour could have, in retrospect, come from the electrical contact with the substrate. As there was an oxide layer all over this had to be removed through scratching and then bonding with Ag paint. It is possible that electrical contact was not always established as a result the majority of the electrostatic field may have come from the wire contacting the substrate and the Ag paint attaching it to the substrate, this does not invalidate the results but may be the cause in the range of DC-EFM signals seen. As the voltages used were in the range of 0-10 V one would expect to observe the electrostatic breakdown of the SiO_2 layer as the breakdown voltage is approximately 15 MV m^{-1} for thick SiO_2 however this was found to increase for thinner films between a few hundred nm to μm thickness' to a value of 0.5 GV m^{-1} [157]. This would give an expected breakdown voltage of 150 V, much higher than used experimentally. The dielectric field strength of air is 3 MV m^{-1}[158] giving a much lower breakdown voltage of 0.9 V beneath the graphene. The fact that we do not knowingly observe any static discharge may either indicate that we are not always contacting the underlying silicon directly or that there is still a small portion of thermal oxide present at the bottom of the trenches etched into the substrate.

6.2 Electrostatic Heterodyne Force Microscopy (E-HFM)

In the previous section we were able to probe the electromechanical properties of some resonator-type graphene samples with DC-EFM, deducing the charge trapped beneath the conductive graphene layer. Whilst we are indeed studying the electromechanical properties with DC-EFM we are limited to relatively low frequencies by various mechanisms such as the speed of the detection system (photodiode, lockin amplifier etc.). This is a fundamental problem if we are to understand the dynamic electromechanical phenomena of future graphene resonators which will be operating in high frequency regimes 50 MHz-1+GHz. To be able to probe the sample properties at such high frequency we turn to the already established method of heterodyne force microscopy (HFM)[23, 106, 108, 159].

Heterodyne force microscopy has been used for a long time to probe the dynamic mechanical phenomena over very short time scales down to ns as described in section 2.3.4.1. This is due to the heterodyne principle which preserves the phase and amplitude of some high frequency action on the cantilever down to a much lower (typically kHz) difference frequency. Here we modify the traditional mechanical HFM setup by replacing one of the mechanical actions with one that is electrical in its origin, calling it electrostatic heterodyne force microscopy (E-HFM). In this particular case a custom piezoelectric transducer with a thickness resonant frequency of around 4 MHz was used, see section 3.2.2 for details. An illustration of the experimental setup of E-HFM is seen in Fig. 6.6.

As shown in Fig. 6.6 we apply an AC+DC electrostatic potential between the probe and the back of the substrate constituting doped Si. The setup used for E-HFM is distinctly similar to that of DC-EFM in the previous section with the addition of the high-frequency piezo transducer mounted beneath the tip. In the case of E-HFM we also use a slightly different conductive cantilever than the Cr-Pt/Ir coated cantilevers for E-HFM. In this case we use Nanosensors® PtSi-CONT cantilevers. The force constant was typically in the range of 0.02-0.77 Nm^{-1}. The reason for using PtSi cantilevers is that PtSi is known to be more

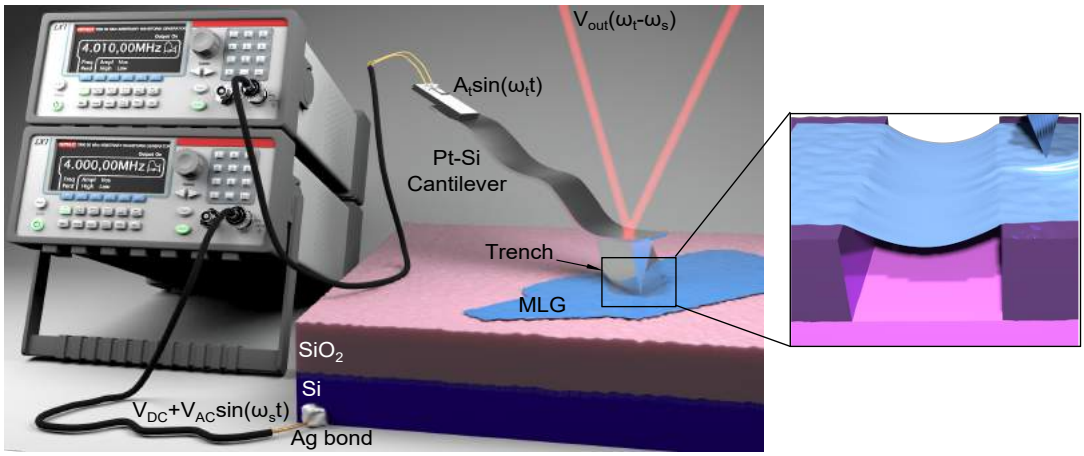

Figure 6.6: The setup for E-HFM with two identical function generators are used with internal clocks synchronised that provide an electrical bias between the probe and the sample/source exciting oscillations of the cantilever. Inset shows the typical type of graphene-resonator device studied

durable than Pt/Ir and therefore less likely to wear away the material at the tip during experiments.

Unlike DC-EFM, a 'low' frequency technique, E-HFM works in the frequency space far beyond the fundamental resonance of the cantilever. For this reason a full theoretical understanding of the mechanism of E-HFM would require a solution the dynamic Euler-beam equation and would have to be solved numerically. Here we consider the simplest case of the factors contributing to E-HFM signal. As shown with the interpretation of conventional HFM[23] we can approximate the tip-surface interaction as quadratic in nature as seen in Eq. 6.6.

$$F = kz_0 + \chi z_0^2 \tag{6.6}$$

Where z_0 is the distance between tip and sample, k is the coefficient for the linear part of the surface interaction and χ is the non-linear coefficient associated with the attractive van der Waal's forces. During E-HFM operation we have several actions that will affect the tip-sample separation, firstly is the vibration of the piezo which oscillates the cantilever at $z_t(t)$

$$z_t(t) = A_t \sin(2\pi f_t t + \phi_t) \tag{6.7}$$

then the motion of the sample e.g. a resonator type device, is given by

$$z_s(t) = A_s \sin(2\pi f_s t + \phi_s) \tag{6.8}$$

where $A_{t/s}$ denotes the amplitude of the vibration of tip or sample, f the frequency and ϕ the phase of the vibration. There is however in our case an additional contribution to the tip-surface separation that is not present in conventional HFM, this is the electrostatic action on the cantilever which we call z_E. Therefore inserting Eq's. 6.7 and 6.8 in Eq. 6.6 we obtain

$$F = k(z_e q - z_E - z_t + z_s) + \chi(z_e q - z_E - z_t + z_s)^2 \tag{6.9}$$

Where $z_e q$ is the equilibrium distance between tip and sample which depends on the set force chosen. By applying 6.9 and assuming a state of equilibrium with the capacitive forces acting on the cantilever we obtain, after some manipulation, the following

$$F_{\Delta f} = \chi A_s A_t \cos(2\pi \Delta f t + \phi_s - \phi_t) - \frac{3A_t L w \epsilon_0 \chi}{2k(h_t + d_1)^2} V_{AC} V_{DC} \cos(2\pi \Delta f t + \phi_c - \phi_t) \tag{6.10}$$

Where Δf is the difference between the tip and the sample drive frequencies, $(h_t + d_1)$ is the separation between the cantilever and the back-gate written as the sum of the oxide layer thickness plus the cone height, l and w are the length and width of the cantilever and ϕ_c is the phase associated with the electrostatic actuation of the cantilever. In Eq. 6.10 we see that force on the cantilever is linear with the tip and sample amplitude as well as with an increase in V_{DC} and V_{AC}. One mechanism which we do not account for is the non-linearity of the electrostatic field, the use of which has been reported elsewhere as the sole source of mixing in a method non-contact electrostatic heterodyne force microscopy[109]. The reason we do not consider the non-linear electrostatic effect is that the amplitude of vibration of the cantilever in contact is much less than in non-contact. Therefore to further understand this we varied both the tip piezo amplitude and the applied AC voltage and measured the response, the results of which can be seen in Fig. 6.7.

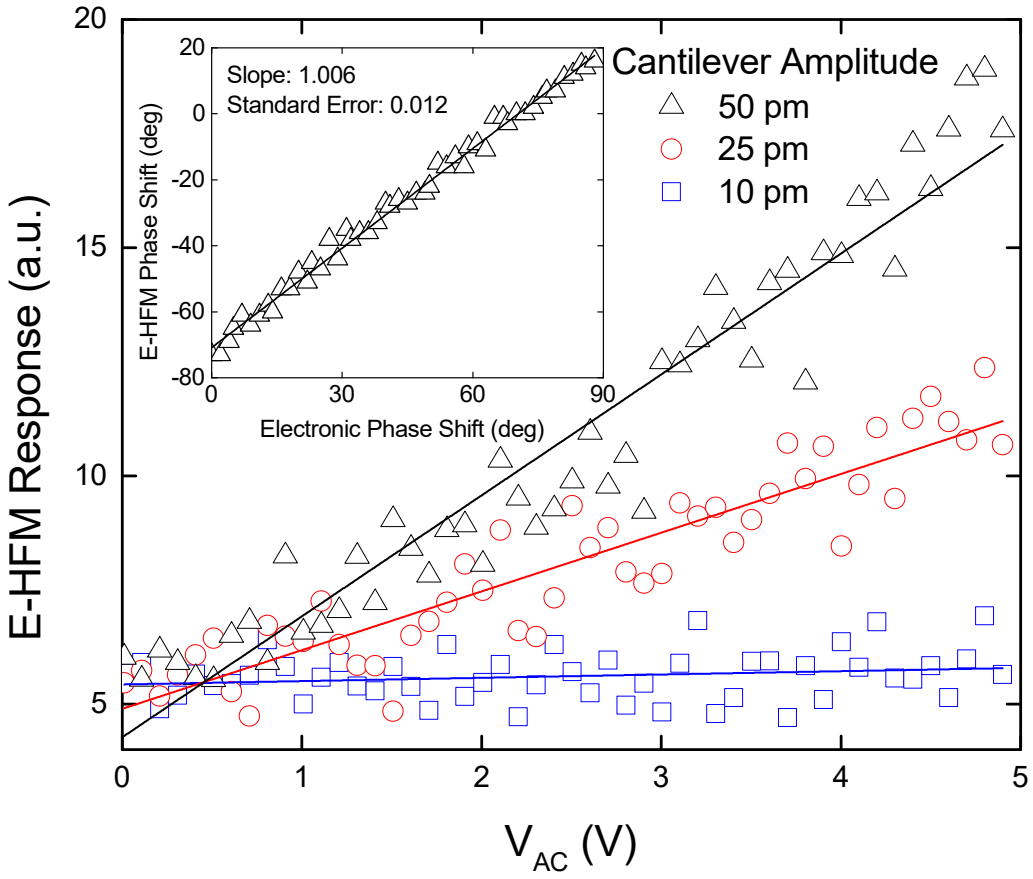

Figure 6.7: In the main figure we drive the tip piezo at 3 different amplitudes: 10, 25, and 50 pm (All peak amplitudes determined by Laser Doppler Vibrometry Polytec (OFV-534/2500)) whilst increasing V_{AC}, V_{DC}=5 V. Inset we sweep the phase of the output of one of the driving forces with respect to the other and measure the resultant change in the E-HFM signal. The tip piezo is operated close to its thickness resonant frequency of 4 MHz whilst the tip is actuated electrostatically at a frequency of 4.01 MHz whilst we detect at the difference frequency.

In Fig. 6.7 we observe that the response of the E-HFM signal is linear to both changes in the tip vibration amplitude and the applied AC bias, this is evidence demonstrating that heterodyne mixing is taking place. A majority of the mixing will have its origins in the non-linear tip-surface interaction however it is expected that there will be a degree of mixing taking place from the non-linear electrostatic field. In Fig. 6.7 we also see that, at a driving amplitude of 10 pm, no signal is observed. This is believed to be because the total combined amplitude of vibration is not sufficient to overcome the sample non-linear regime required for frequency mixing, typically on the order of the interatomic spacing (100-200 pm).

Whilst we have chosen the thickness resonance of the tip piezo so far to increase the strength of the E-HFM signal, it is not known if there are any other resonances present in the system, such as cantilever contact resonances. To understand how the behaviour of E-HFM responds to a wider range of drive and difference frequencies, we produced a map of the E-HFM response as can be seen in Fig. 6.8.

From Fig. 6.8 we see a clear increase in the signal whilst working at both the cantilever contact resonance (f_0 ≈65 kHz) and at the various resonances of the piezo transducers. It would make sense that to maximise the E-HFM signal one should work at both the cantilever resonance and simultaneously one of the piezo resonances, however this can be detrimental to the phase measurements. Whilst working at the cantilever resonance the E-HFM phase is prone to being unstable due to its sensitivity to the tip-surface properties[93]. It may be possible to modify the E-HFM to always work slightly off the cantilever resonance through a feedback system to increase both the phase and amplitude sensitivity however we do not consider this approach yet.

Having demonstrated the heterodyne mixing in E-HFM we needed to understand how E-HFM behaves in characterising NEMS. For this we fabricated a series of graphene resonator-type devices. For this we followed the procedure given in appendix section A.1 whereby trenches were etched into a Si/SiO_2 substrate and graphite was exfoliated on top over a trench. One of the devices that we now study is seen in Fig. 6.9

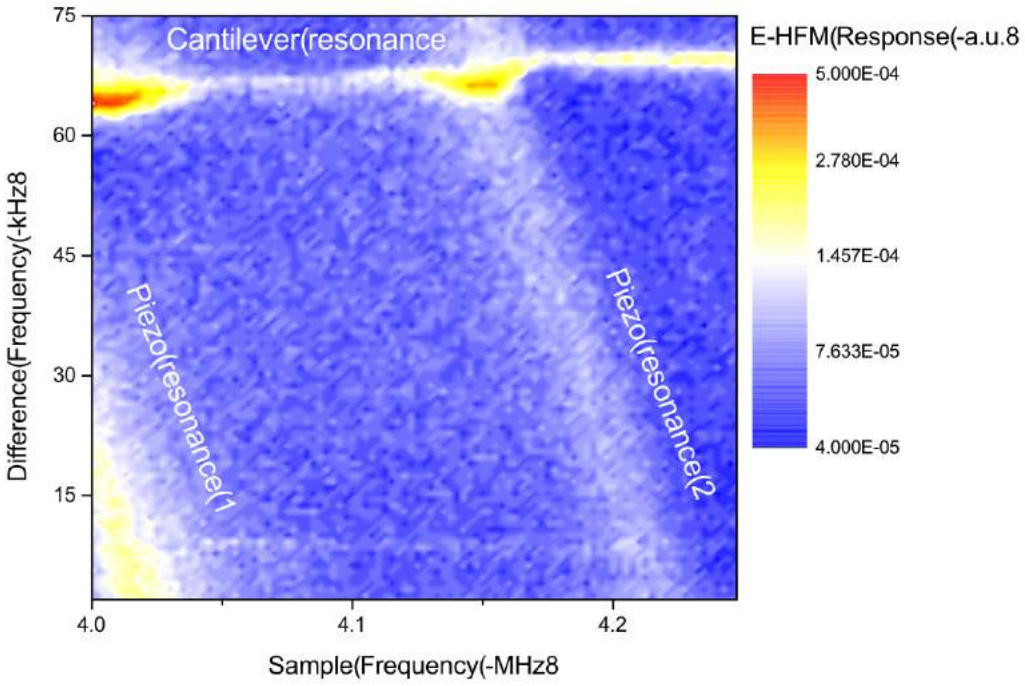

Figure 6.8: E-HFM response as we drive the sample frequency between 4 and 4.25 MHz whilst the tip is driven at a frequency of Δf below this. As a result we see several features such as two of the main piezo resonances as diagonal lines, demonstrating that they are attributed to a certain frequency of the tip piezo. In addition to this the main cantilever contact resonance is seen as an increase in the E-HFM amplitude. At the crossover points there is a two-fold increase in the E-HFM signal at approximately 65-70 kHz. For the purpose of this map the tip was stationary on an SiO_2 surface.

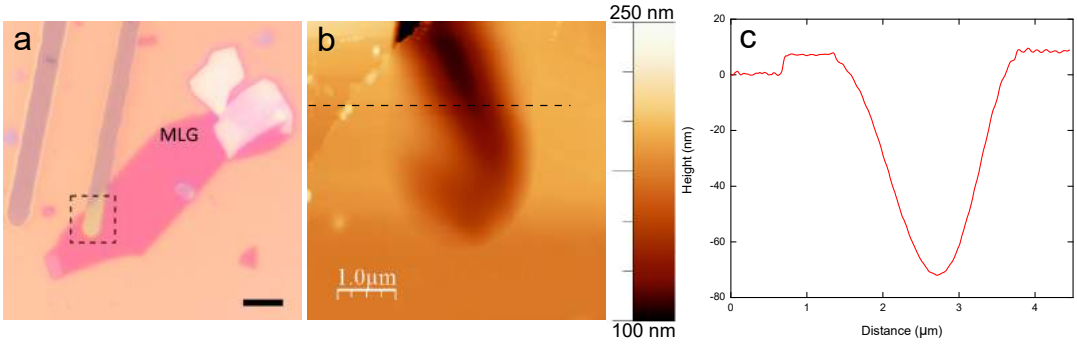

Figure 6.9: Analysis of the MLG flake used predominantly in this study. Image a) shows an optical image of the flake on a Si/SiO_2 flake (300 nm oxide layer) with a 5 μm scale bar. Image b) shows the contact AFM topography map of the dotted region in image a) where in turn the dashed line is the height trace shown in image c). From c) we clearly see the step from SiO_2 to MLG on the left and the region where the material is suspended.

The device shown in Fig. 6.9 was found to be approximately 7 nm thick suspended over the end of a trench which is 2.5 μm in width. To approximate the vibration amplitude one would, expect we again turn to section 2.2.1 where we obtain a figure of 7.5 nm. This number in reality is expected to be much lower due to various damping effects which will increase as the device's operating frequency increases. We then employ E-HFM and HFM to study the flake in Fig. 6.9. The results of which can be seen below in Fig. 6.10.

In Fig. 6.10 we observe that in HFM the amplitude response is extremely small, indicating a very soft material as one would expect for thin MLG suspended over a 2.5 μm gap. We also observe that the HFM phase response is extremely noisy whilst on the suspended material. This may indicate that the sample is too soft and that the amplitude of vibration is too small to overcome the tip-sample non-linearity. The fact that both that HFM amplitude and phase response is stable whilst the tip is on the supported material is further evidence to support this claim. There is however some degree of contrast seen on the suspended material, this may indicate that there are some local variations in the sample mechanical properties allowing mixing to occur. As we look at the E-HFM response we observe that the signal is stable in both amplitude and phase whilst the tip is in contact with both the supported and suspended regions. This may

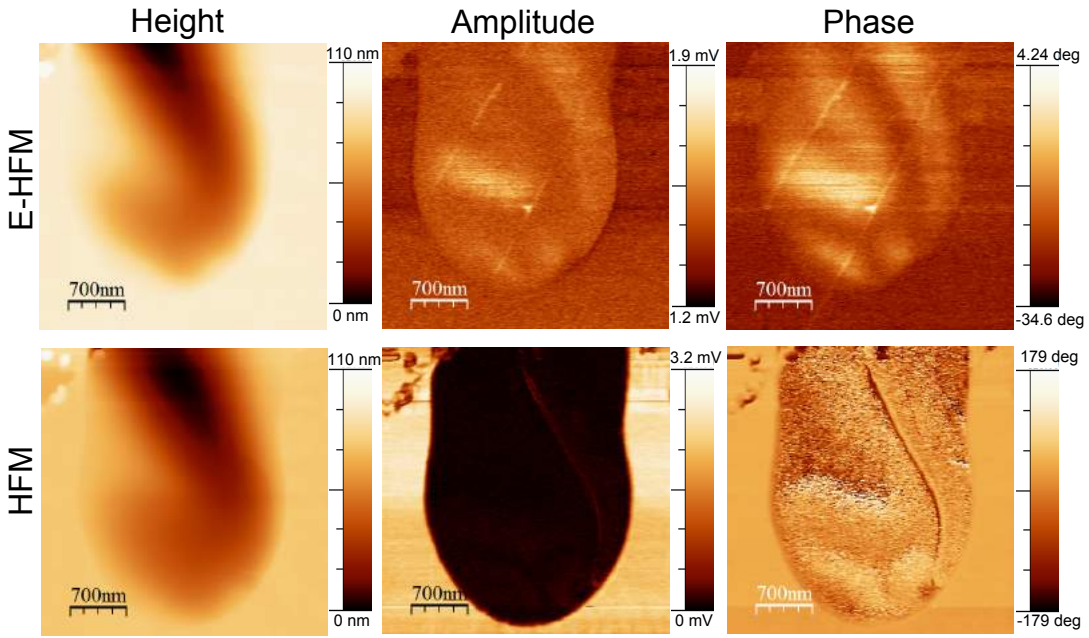

Figure 6.10: A comparison of the E-HFM technique of MLG suspended over a trench with conventional HFM. Topography, amplitude and phase images are all shown. The contact force used in E-HFM images was $F \approx 0$ nN, f_t=4.01 MHz, f_s=4 MHz, V_{AC}=5 V, V_DC=-5 V and tip piezo amplitude=250 mV. For HFM we use the following settings F=3.5 nN, f_t=4.01 MHz, f_s=4 MHz, tip amplitude 350 mV and sample piezo drive amplitude 3 V.

suggest one of two things: Firstly that the graphene is oscillating itself due to the electrostatic forces present thus providing additional amplitude which overcomes the tip-sample interaction and mixes. The second case may be that the electrostatic vibration amplitude may be considerably higher than that of conventional HFM allowing it to overcome the tip-sample non-linearity.

We do not consider the mixing through the electrostatic field as the cause for the E-HFM contrast on the suspended MLG, because if it was purely the mixing due to the non-linear electrostatic interaction we would see no nanoscale variations in the signal. We may also rule out that the vibration amplitude of both tip and sample being higher in E-HFM than HFM leading to absence of mixing on the suspended region in HFM, because on the supported material next to the trench we see a higher signal in HFM than E-HFM. Therefore we propose that the contrast on the suspended region of MLG is observed in E-HFM due predominantly to the electrostatic actuation of the membrane itself. One additional possibility that we propose for the high signal on the suspended MLG for E-HFM is the non-linearity of the vibration of the graphene itself.

6.3 Differential Interferometry of Graphene Resonators

Using a system devised by den Boeff [26] but similar to those used in other studies[160, 161], we use the setup seen in Fig. 6.11. Here a low-noise 5 mW laser where λ=635 nm, is used as the power source. The light from the laser is initially incident on a linear polarizer (LP), which is oriented at 45°. Upon passing the linear polariser the beam passes through a non-polarising beam-splitter (NPBS) and on to the first Wollaston prism (WP1). Here WP1 spatially splits two equal components of the polarised light at an angle of almost 9 degrees whilst introducing a phase difference between the two polarisations of ϕ. Both beams are then incident on a lens with focal length of 10 mm where both beams are then focused on to the sample with a separation of approximately 500 μm. Once the beams have been recombined by WP1 they pass back through the NPBS and

through a $\lambda/4$ plate. The purpose of this quarter wave-plate is to ensure that the optimal phase between the object and reference beams is such that when the beam goes back towards the laser it is completely blocked by the LP. Next the laser beam reaches the second Wollaston prism (WP2) which is rotated by 45 degrees about the optical axis. The purpose of this is to provide the mixing of the two beams. It is important to note that the distance between WP1 and the lens should be equal to the focal length of the lens. This is so that maximum overlap between the beams is achieved and therefore greater interference obtained. To illustrate the operating principle we have shown the phases of the two orthogonally polarised beams at various stages of the interferometer in Fig. 6.11.

As Fig. 6.11 demonstrates we can tune the relative phase between the object and reference beams by shifting WP1, this is done through the use of a piezo transducer (PI Ceramics). By shifting the relative phases between the two beams we can ensure that the power on each photodiode is the same which is the ideal condition where a shift of the phase between object and reference is detected most readily. This ideal phase difference between the object and reference beams is given as$(2n+1)\pi/2$, $n = 0, 1, 2....$ By meeting this condition the total power on PD1 and PD2 are identical and are cancelled out through the use of a differential amplifier along with any amplitude noise in the laser signal. Any change in the phase of the object beam will lead to equal and opposite changes in amplitude at each photodiode segment arising from the additional shift of π produced at WP2. By shifting WP1 over relatively large distances ($\approx$25 μm) we see this sensitivity of the system is sinusoidal in nature as shown in Fig. 6.12 and reported elsewhere[26, 161], therefore for prolonged experiments it may be necessary to include a feedback loop to ensure that piezo drift is not affecting the system sensitivity.

In Fig. 6.12 we see the sinusoidal relationship. This peak to peak value of this sinusoidal relationship can be used to calibrate the whole system as the absolute peak to peak amplitude represents a shift of $\pi/2$ or $\lambda/4$=159.25 nm. However the response of the system is not linear for these very high amplitudes so it is necessary to only consider the linear region of the sine graph and calibrate the amplifier output from here. To understand the sensitivity of the system we

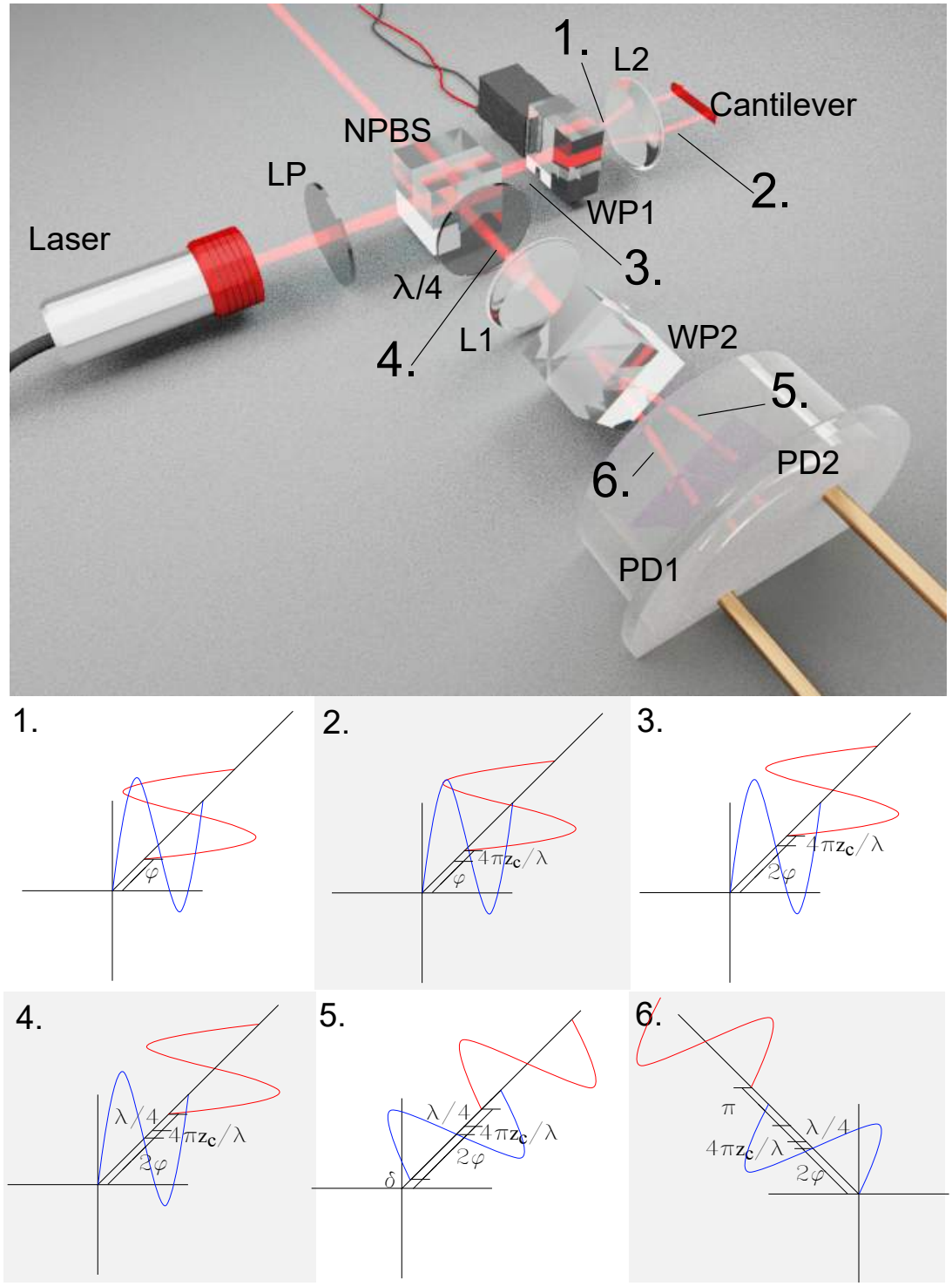

Figure 6.11: Illustration of the operating principles of the differential interferometer. Sub-figures 1-6 showing the relative phase between the object and reference beams correspond to the numbers in the main figure. Here the polarised light is split into a vertically polarised beam (blue) and a horizontally polarised beam (red), one of which is incident on the end of the cantilever, the other on the base.

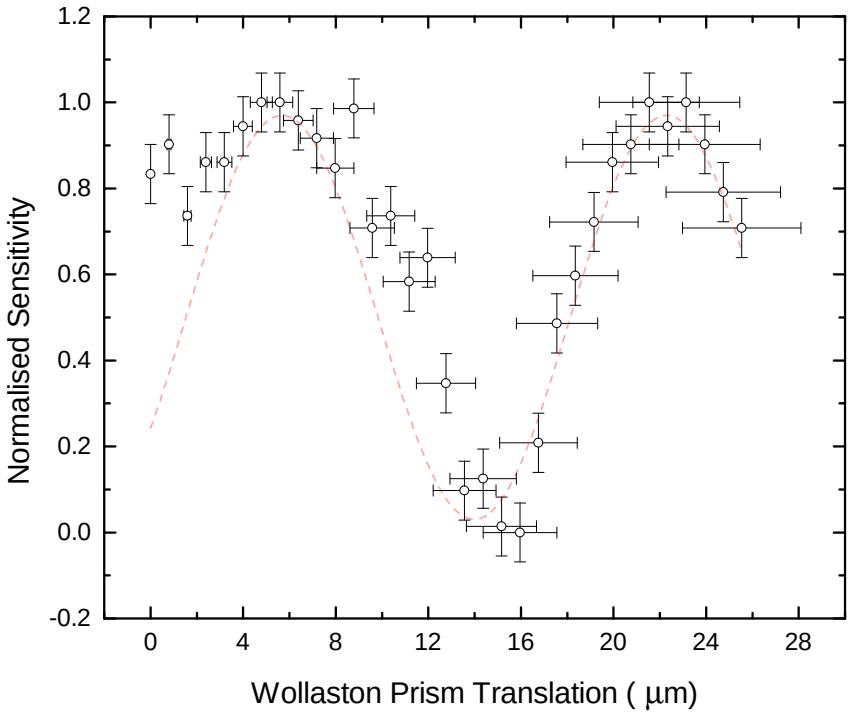

Figure 6.12: Here we show the height of the fundamental thermal resonance peak of a cantilever as a function of the distance moved orthogonally to the beam by WP1. The peak height is normalised to the highest level of sensitivity. A sinusoidal fit is applied to the data (red dash).

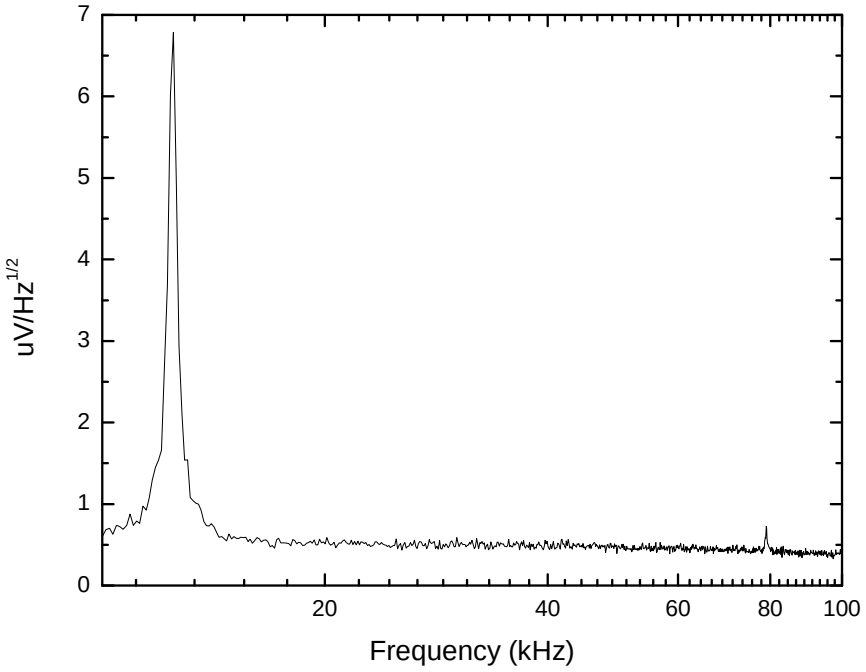

Figure 6.13: Power spectral density of the system when measuring the thermal resonance of a contact mode cantilver (BudgetSensors®, ContAl-G) in air at room temperature. The first primary resonance is seen at $f \approx$13 kHz and the second resonant mode seen at $f \approx$80 kHz.

employ it to study the thermal resonance of the cantilever, that is the excitation of the resonance modes due to thermal energy present $k_B T$. For this we use a simple contact mode cantilever with the object beam focused on the end and the reference beam focused at the base of the cantilever. The resulting power spectral density measured is seen in Fig. 6.13 where we observe the first and second thermal vibrational modes of the cantilever.

In Fig. 6.13 we observe that the electronic noise floor of the system in the low-frequency regime is of the order of 400 nV/Hz$^{1/2}$. Thus far we have only considered the case where the object beam is incident on a completely reflective sample which therefore introduces an additional phase of $4\pi z/\lambda$. For the application to graphene and other 2D-materials, where the thickness is of the order of

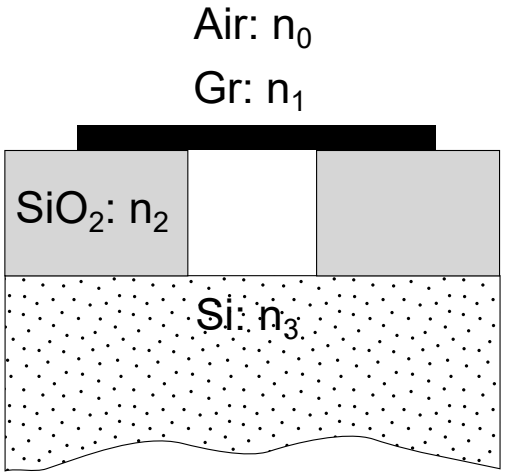

Figure 6.14: Schematic showing the ordering of materials and their refractive indeces for graphene suspended over a trench. In the case of the object beam the laser is incident on the graphene over the trench and the reference beam is incident on plain SiO_2 on Si.

1 nm, a few atomic layers, the mechanism for this additional phase on the object beam is different. As has been studied both theoretically and experimentally in other works [66, 67, 68] the visibility of graphene on a substrate depends on the thickness of the underlying SiO_2. To generate a theoretical basis for predicting the behaviour of the interferometer when measuring the resonances of graphene and other 2D materials on SiO_2 we turn to the work of H. Anders [69]. Firstly we must consider the system and the all of the refractive indices involved, see Fig. 6.14.

With Fig. 6.14 in mind we consider a beam of coherent light incident on the substrate as

$$A(x,t) = A_0 e^{i(kx-\omega t+\phi)} \tag{6.11}$$

This is either incident on the SiO_2/Si substrate or graphene suspended over a trench etched into the substrate. Here a portion of the beam will be reflected, absorbed or transmitted. The reflection coefficients are given below where r_1 is the reflection coefficient for the graphene/air interface, r_2 graphene/SiO_2, r_3 SiO_2/Si, r_4 air/SiO_2 and finally r_5 for the air/Si interface

$$r_1 = \frac{n_0 - n_1}{n_0 + n_1} \tag{6.12}$$

$$r_2(\lambda) = \frac{n_1 - n_2(\lambda)}{n_1 + n_2(\lambda)} \tag{6.13}$$

$$r_3(\lambda) = \frac{n_2(\lambda) - n_3(\lambda)}{n_2(\lambda) + n_3(\lambda)} \tag{6.14}$$

$$r_4(\lambda) = \frac{n_0 - n_2(\lambda)}{n_0 + n_2(\lambda)} \tag{6.15}$$

$$r_5(\lambda) = \frac{n_0 - n_3(\lambda)}{n_0 + n_3(\lambda)} \tag{6.16}$$

The reflectance of the reference beam of the laser incident on SiO_2/Si ($r_r e^{i\epsilon_r}$) shown by H. Anders [69] and the reflectance of the object beam ($r_o e^{i\epsilon_o}$) incident on the graphene suspended over an air gap, derived by similar methods, are shown below

$$r_r e^{i\epsilon_r} = \frac{r_4 + r_3 e^{-i\Delta_2}}{1 + r_4 r_3 e^{-i\Delta_2}} \tag{6.17}$$

$$r_o e^{i\epsilon_o} = \frac{r_1 - r_1 e^{-i\Delta_1} + r_5 e^{-i(\Delta_1+\Delta_0)} - r_1^2 r_5 e^{-i\Delta_0}}{-1 + r_1^2 e^{-i\Delta_1} + r_1 r_5 e^{-i\Delta_0} - r_1 r_5 e^{-i(\Delta_0+\Delta_1)}} e^{i(4\pi n_0/\lambda)\delta \sin(\omega t)} \tag{6.18}$$

Where Δ_i is the phase picked up by passing through a medium of refractive index n_i and of thickness d_i and is given by

$$\Delta_i = \frac{4\pi}{\lambda} d_i n_i \tag{6.19}$$

To understand what happens to the object beam in Eq. 6.18 when we oscillate the graphene membrane we modulate sinusoidally the air gap between the graphene and the Si as follows

$$d_0 = d + \delta \sin(\omega t) \tag{6.20}$$

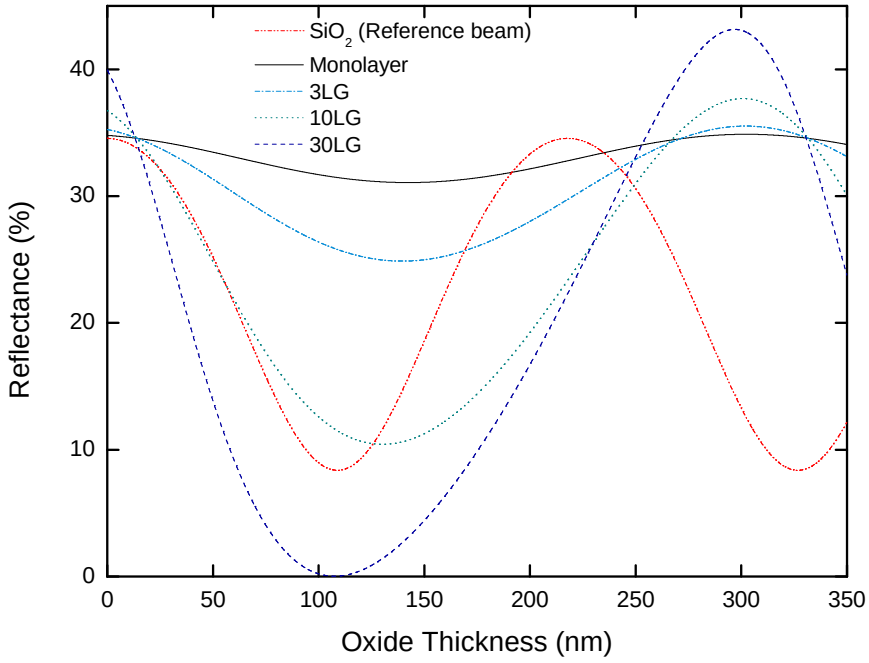

Figure 6.15: Reflectance of a coherent 635 nm source of light on a system of SiO_2 on Si for varying oxide thickness (red) and for the system where graphene of varying thickness is suspended over an air gap equal to the oxide thickness on Si. Thicknesses shown are monolayer (black), tri-layer (blue dot/dash), 10-layer (green dots) and 30-layer thick graphene (purple dash).

Where δ is the amplitude of the graphene resonator and ω the frequency whilst d is simply the oxide layer thickness. In addition to this we have an additional term of $e^{i(4\pi n_0/\lambda)\delta\sin(\omega t)}$ which corresponds the extra distance the beam travels to hit the graphene resonator. To understand how the reflected intensity of the beams will be affected by a) the oxide thickness and b) the thickness of the suspended graphene we plot the reflected intensity of Eq's. 6.17 and 6.18 in Fig. 6.15.

To consider the signal that one will observe from the differential amplifier we subtract the intensities of the object and reference beams, 6.17 and 6.18 where the difference is that there is an additional phase shift of π radians between the two mixed beams of light split by WP2. To incorporate this we add an extra $e^{i\pi}$

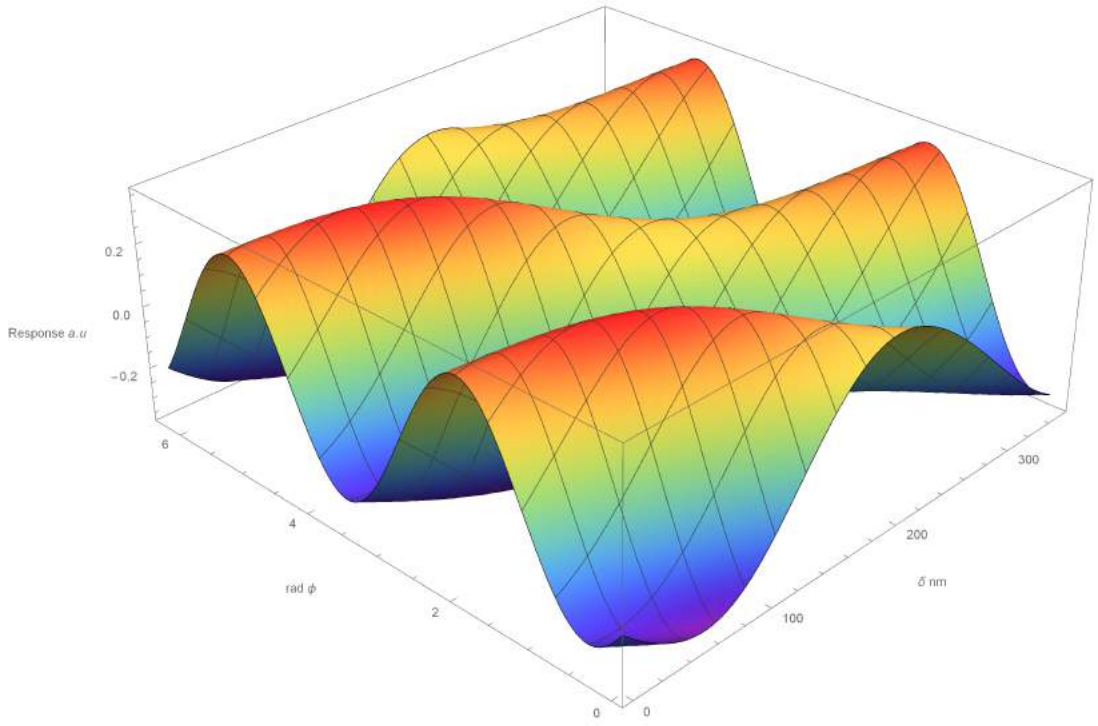

Figure 6.16: Simulation of Eq. 6.21 where we assume an ideal case of 220 nm of oxide/air gap for a 635 nm laser incident on 10LG. Where ϕ is the shift of one polarisation with respect to the other from WP1 and δ is the additional motion from the suspended MLG.

term as shown in Eq. 6.21.

$$PD_{1-2} = \left|\frac{1}{2}E_r(r_0 e^{i(\epsilon_0+2\phi+\frac{\pi}{4})} + r_r e^{i\epsilon_r})\right|^2 - \left|-\frac{1}{2}E_0(r_0 e^{i(\epsilon_0+2\phi+\frac{5\pi}{4})} + r_r e^{i\epsilon_r})\right|^2 \quad (6.21)$$

Where plotting Eq. 6.21 as a function of ϕ and δ in Fig. 6.16 we see that it is beneficial in terms of sensitivity for ϕ to be a value such that the total response is 0 and also that any change in δ will result in a linear increase of the output signal. This is displayed in Fig. 6.16.

From Fig. 6.16 we see that for large amplitudes of vibration the response of the interferometer becomes non-linear due to the large additional phase shift introduced by the graphene membrane. This amplitude is typically on the order of 50 nm which is well above the typical operating amplitudes of the graphene

NEMS studied here.

From Fig. 6.15 we see that we must pick a thickness of the oxide layer such that the slope of the line in Fig. 6.15 is greatest. This corresponds to the responsivity of the system to the motion of the graphene. This presents a difficult challenge to conventional methods of optical detection for graphene resonators as the region of highest slope does not always correspond to the region where there is zero or minimal refletance, espescially when one considers the sagging of the graphene down into the trench. This failure to cancel out the power from the object and allows any laser amplitude noise or drift to be present in the measurement. The method of differential interferometry presented here provides a solution to this problem as the linear polarising filter seen in Fig. 6.11 can be tuned so that the relative intensities between the object and the reference beams are identical, regardless of what the oxide thickness is. From here one would only need to select the oxide thickness which gives the maximum responsiveness to the desired thickness, since any laser noise can be cancelled out through adjustment of the rotation angle of the polarising filter.

6.4 Summary

In this chapter on the electromechanical properties of devices made from 2D materials we have introduced several new experimental methods. The first of which is direct contact electrostatic force microscopy (DC-EFM), a method previously developed [105], where we have demonstrated the unique ability of this technique to probe charge trapped beneath 2D materials, an otherwise hidden quantity. Using DC-EFM to study resonator-type devices fabricated from few-layer graphene we have established that in order to measure the charge density beneath the material one must be able to detect the electrostatic actuation of the device. Given this we have detected actuations on the order of a few hundred pico metres and successfully inferred the trapped charge density.

In building on the electromechanical nature of DC-EFM measurements we merge it with another established technique of heterodyne force microscopy (HFM) [162]. In doing so we mate the electromechanical nature of DC-EFM with the

sensitivity to time-dependant phenomena from the heterodyning technique to give electrostatic heterodyne force microscopy (E-HFM). We first study the nature of this technique and proceed to apply it to suspended few-layer graphene resonators. It is in doing this and comparing with traditional heterodyne force microscopy (HFM) that we are able to probe the time-dependant electromechanical properties of the device on a nano second and nano metre scale. From studying simple electromechanical systems made from few-layer graphene we show that there is a high level of non-uniformity, believed to be largely due to complicated stress distributions in the sample.

Finally we apply a little known method of optical interferometry capable of 25 fm$\sqrt{Hz}$ sensitivity to resonators from 2D materials. Here we lay down the experimental procedure and theoretical framework to understand the behaviour of such an interferometer to resonator-type devices deposited on a traditional Si/SiO_2 substrate. We demonstrate the sensitivity experimentally by measuring the first two thermal resonant modes of a contact mode cantilever under ambient conditions, where amplitudes were expected to be in the pico metre regime. This method is presented as an improvement on conventional optical techniques due to the ability to tune to a variety of samples in such a way as to completely remove laser amplitude noise, important for probing such devices at low temperature.

Chapter 7

Further Work and Future Directions

In this chapter we bring together the work that was performed towards the end of the project and that was not fully completed but nonetheless gives a future direction for the research into 2D materials based NEMS and related scanning probe methods. In this chapter we both show the development of a new avenue of research as well show and suggest improvements made to some of the techniques developed in this thesis.

7.1 Interaction of 2D materials with Surface Acoustic Waves

Whilst in the majority of this thesis we have actuated the graphene resonator type devices electrostatically, by contacting the flake directly and applying a voltage to the back-gate, we can not apply this to resonators fabricated from insulating materials such as h-BN. It was therefore initially proposed to excite the suspended membranes with surface acoustic waves (SAW). However the application was not limited to this, as one could measure the electromechanical response of materials simply placed on the substrate subjected to the SAW's. To produce SAW's

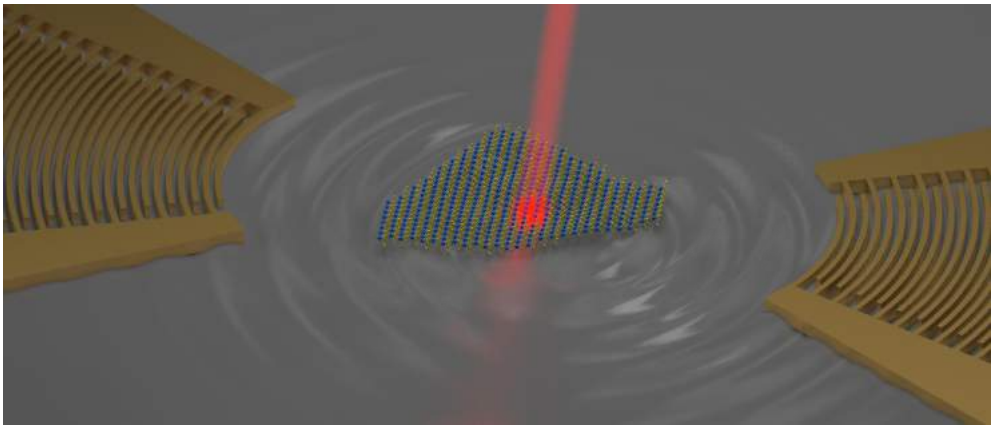

Figure 7.1: Illustration of surface acoustic waves interacting with an MoS_2 flake upon which a laser is incident, changing the electrical boundary conditions of the SAW through photo-excited carriers.

one would have to deposit interdigitated transducers (IDT's) on a piezoelectric substrate, then either etch a tench into the surface and deposit a flake of h-BN or deposit a 2D-material of choice in the immedaite path of the IDT's. Traditional IDT's are rectangular in geometry however it was found that by changing this to a circular or elliptic profile one was able to focus the surface acoustic waves into a rather small area [163, 164]. To understand the affect of the geometry of the IDT's we employed finite element analysis (FEA) software (COMSOL) to simulate the dynamics of SAW on a $LiNbO_3$ substrate in the X crystallographic orientation. The results of one of these simulations is seen in Fig. 7.3.

Here we find that the focused interdigitated transducers(FIDTs) are effective at focusing the surface acoustic waves and there is a preferential curvature at which the beam is most narrow and parallel, which can be found through simulation, thus greatly aiding the operating efficiency of the devices produced. Once the optimal shape of the IDT's has been determined one must decide the spacing period between the individual fingers, that is the frequency at which the SAW's should be excited. For this study we chose a frequency of 433 MHz to give a short wavelength as the SAW velocity in $LiNbO_3$ in the X-direction was approximately 3870 ms^{-1} [165] giving a wavelength of approximately 9 μm. The reason for wanting a wavelength of this order was that it was comparable to the exfoliated flakes studied and also comparable in length to twice the approximated

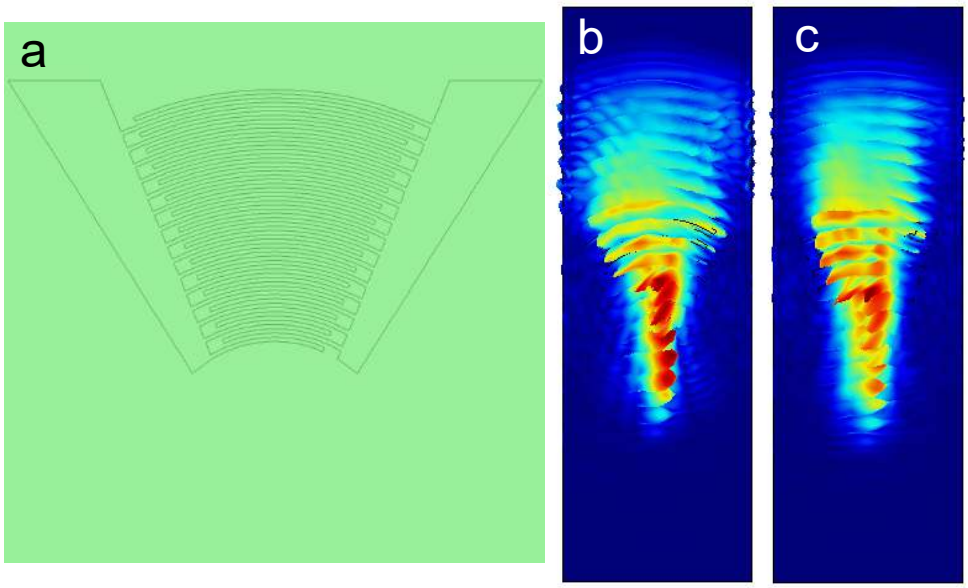

Figure 7.2: FEA results on the simulation of FIDT. Image a) shows the setup of the curved IDT fingers used in the simulation whereas b) and c) show the focusing of the SAW beam for the case where the ratio fo the radii in the x and y directions R_y/R_x is given as b) 0.89 and c) 0.7. The simulated inbut voltage was 0.1 mV.

suspended region of h-BN beam resonators. Choosing the frequency such that the individual finger width was not less than 1 μm greatly aided in the fabrication of devices as it was within the capabilities of optical lithography. A series of test devices were fabricated using optical lithography, one of which is seen in Fig. 7.3.

None of the devices shown similar to that in Fig. 7.3 were tested due to experimental difficulties with the adhesion of the Ti/Au contacts to the substrate. Instead future devices will use Al contacts as these are both lighter and will not dampen the SAW's to the same extent but also the adhesion is found to be better.

7.1.1 Bilayer h-BN Resonators, Interaction with Surface Acoustic Waves and Flexoelectricity

The use of h-BN as a material in the use of NEMS is expected to bring with it a series of new phenomena that will alter the device performance. One such effect is the phenomena of flexoelectricity[166, 167]. This is the effect by which

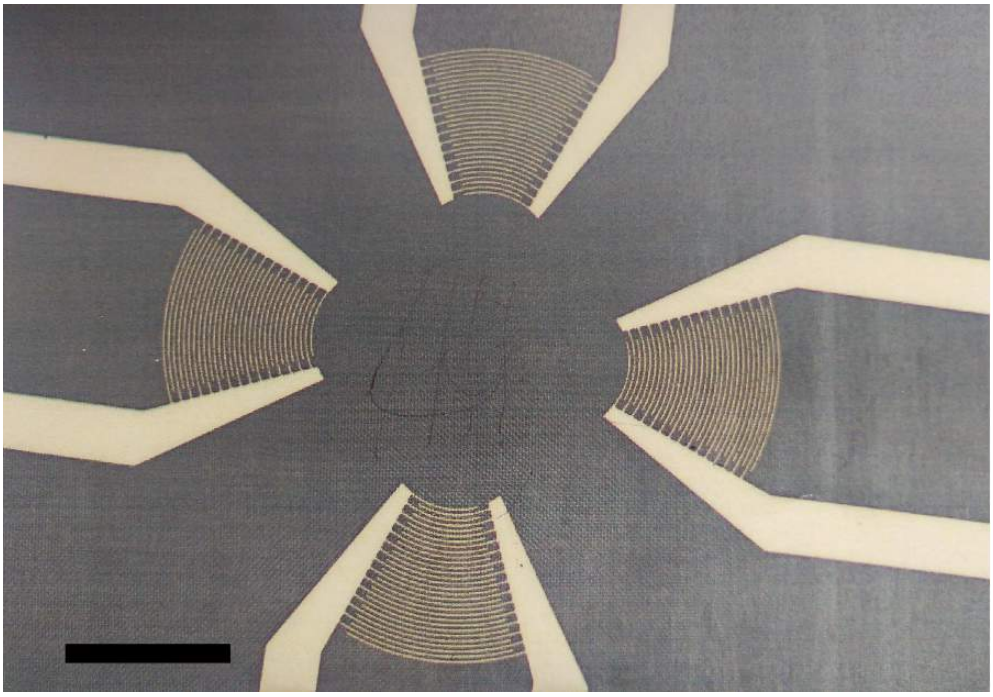

Figure 7.3: Optical microscope image of FIDT's on $LiNbO_3$. Scale bar in lower left corresponds approximately to 100 μm. Contacts are deposited with a Ti adhesion layer (30 nm) and Au (150 nm).

dielectric materials exposed to high levels of non-linear stress exhibit an electrical polarisation. The flexoelectric effect becomes more prominent in the thin limit of materials where strain gradients are highest. With 2D-materials being the thinnest by nature one would expect to be able to easily observe any flexoelectric effects.

In addition to this, h-BN has been predicted to exhibit piezoelectric properties when stacked in an odd number of layers[168], assuming that the layers are stacked in an AA' fashion (i.e. each boron atom has a nitrogen atom directly above and below and vice versa) [43]. This piezoelectricity has its origins in the noncentrosymmetric nature of the odd layered crystals. If one were to use bi-layer h-BN the electrical polarisation observed due to mechanical strain would solely be due to the flexoelectric effect.

We are therefore interested in observing the interaction of the surface acoustic waves with suspended bilayer h-BN to observe the electromechanical effect that is flexoelectricity. To try to gain a theoretical understanding and even predict the behaviour of such a system we attempt to simulate elastic waves in the bilayer h-BN. Elastic waves such as SAW's travelling along the surface in a traditional medium are typically called Rayleigh waves however once the medium in which the wave is travelling becomes suitably thin, the depth at which the wave penetrates normally interacts significantly with bottom surface. Waves of these nature are known as Lamb waves and can take two forms; firstly where the motion of the top and bottom surfaces is symmetric about the mid-plane and secondly where they are anti-symmetric about the mid-plane. It is therefore expected that SAW incident on bilayer h-BN will produce Lamb waves in the ultrathin limit. The presence of Lamb waves in bilayer graphene has already been studied theoretically where the dispersion curves of the various modes are predicted[169]. We therefore use this approach in calculating the dispersion curves of bilayer h-BN without considering flexoelectricity, the results of which are seen in Fig. 7.4.

From Fig. 7.4 we observe that in the 'low' frequency regime we should observe the first three antisymmetric modes (A_0, A_1, A_2) and the second symmetric mode (S_1). To understand further the behaviour of these modes and the dispersion relation one would have to include the theory of flexoelectricity.

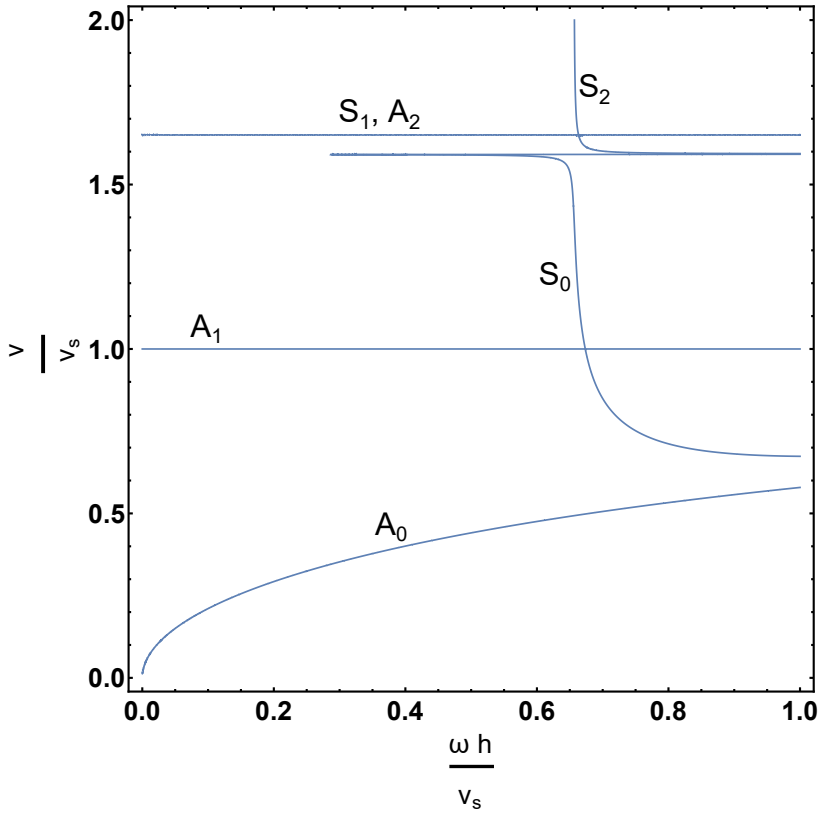

Figure 7.4: The Lamb wave dispersion curves calculated for bilayer h-BN showing the dimensionless velocity as a function of dimensionless frequency where v_s is the shear wave velocity in the material and h is the bilayer thickness. The types and orders of vibrational modes are shown where A_n corresponds to antisymmetric and S_n symmetric of order n.

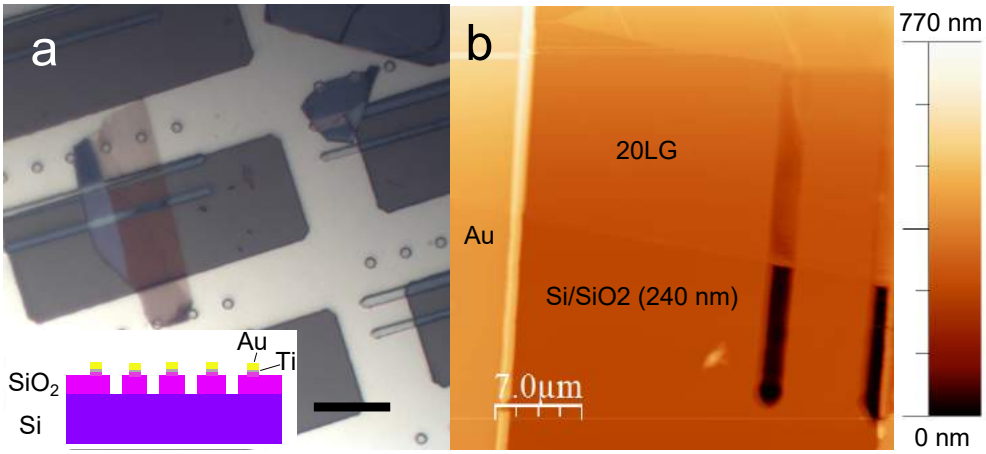

Figure 7.5: The resonator type device fabricated from MLG suspended over a series of trenches. The image in a) shows the MLG flake suspended over one and partially two trenches whilst electrically contacting the Au contacts. Inset we have the side schematic of the sample layers. Trenches are etched into the Si/SiO_2 substrate to a depth of 300 nm. A grid is then laid over the top of these trenches where a layer of SiO_2 (50 nm) is first deposited to prevent any contact from the Ti/Au with the underlying Si. Ti is of thickness 20 nm and Au 100 nm. The MLG of varying thickness is then transferred as the final stage. Image b) shows the AFM topographical image of the suspended flake.

7.2 High-Frequency Electrostatic heterodyne force Microscopy

To understand further the mechanism by which E-HFM images graphene and other 2D-material based NEMS it is important to decouple the electrostatic effects on the cantilever due to the back-gate from the interaction with the device itself. For this it will be important to use both stand-alone graphene resonators, which do not rely on an electrically conductive tip to be grounded, combined with an electrically insulating tip, which should not interact detectably with the electrostatic field. Towards the end of this study a series of devices were fabricated for this purpose such as the one seen in Fig. 7.5

Imaging such a device both in vacuum with E-HFM will allow one to decouple the electrostatic interaction of the cantilever from that of the device itself. This would need to be done under vacuum to ensure that there was a high Q-factor

associated with the resonator.

Chapter 8

Conclusion

In conclusion we have studied the morphological, mechanical and electromechanical properties of 2D materials and their heterostructures. By studying the morphology of graphene on h-BN and the resulting Moirè pattern we have elucidated that the sample adhesion over the period of the Moirè superlattice varies detectably. We propose that the origin of the observed UFM contrast of these samples is largely due to the variation in sample adhesion, where for the incommensurate regions (i.e. a carbon atom does not sit directly on a boron or nitrogen atom benath) the adhesion is higher. We also observe an increase in the friction present at the AFM tip in these regions, providing further evidence to support the claim. Having probed the small scale (in the range of a few tens of nanometres) morphological properties of graphene on h-BN in the Moirè superlattices, we then turned our attention briefly to the larger scale morphological properties. By probing the large scale structure, typically on the μm scale, with both contact mode AFM and UFM we are able to observe delaminations in the graphene, these delaminations were elongated and non-uniform eluding to the claim that there is a complicated stress distribution in the system. What is more is that we were able measure the mechanical integrity of these delaminations for graphene on SiO_2 and on an h-BN substrate, where we find that in the latter case the delaminations are more rigid. The implications of which may suggest that the stress distributions of graphene on h-BN are largely non-unifrom on the micrometre scale but on a scale of tens to hundreds of nanometres form regular periodic structures indicative of

a regular stress pattern. These findings may help to understand future electronic device performance of graphene on insualting h-BN.

Having used force modulation microscopy (FMM) and ultrasonic force microscopy (UFM) to image morphological structures we then turn our attention to the capabilities for such techniques to probe the subsurface structure of thick stacks of 2D materials or heterostructures. To do this we initially use a theoretical approach to understand the role of the material anisotropy in the lateral resolution of UFM but also the depth at which one is able to probe. From this we find that the weak interlayer van der Waals bonding and therefore low out of plane elastic modulus E_3 and weak interlayer shear modulus G_{23} allow the stess field beneath the AFM probe to become 'focused' almost entirely underneath the tip. We demonstrate this effect of the focusing of the stress field by imaging MoS_2 and MLG of thickness between 10-120 nm on trenched substrates where we can clearly see the trench beneath the thick material. We confirm that the UFM contrast is due to both the flexing and the contact stiffness from the applied load and that in the case of large defects such as the trench beneath the material we see that the flexing of the sample dominates the UFM contrast. However when we remove the effect of large-scale sample flexing we were able to observe the substrate interaction with the bottom layer through flake thickness' of over 15 nm. Therefore the ability for ultrasonic techniques of UFM and HFM to probe the subsurface structure of layered 2D materials and heterostructures is greatly enhanced by the high level of anisotropy inherent in the materials. This therefore makes these techniques a valuable tool in characterising heterostructures of ever increasing complexity and layer numbers. It also allows one to non-destructively probe the subsurface properties of such a system, an ability which is not currently possessed by any other known technique.

With our understanding of the subsurface contrast provided by UFM and the role in which sample anisotropy plays we turn our attention to the mechanical properties of graphene grown on $4H$-SiC. The growth of graphene on SiC provides a possible solution to the problem of high quality and large-scale growth of graphene films. There is however an isssue with the interaction of the SiC substrate affecting the electronic properties of the graphene layer. One effective solution proposed in literature was to intercalate the substrate with hydrogen,

effectively removing the interaction the graphene layer and thereby improving the electronic properties, however it was not know to what extent this decoupled gaphene from substrate. We employ UFM to study the mechanical properties and therefore the interaction that the graphene layer/s have with the substrate. From this we report that there is a significant decrease in the measured sample stiffness indicating that the graphene layer is largely decoupled from the substrate. However we also state that the layer is inherently stable as we not observe the tearing or breaking of the graphene layer/s. This is important as it means that the substrate provides adequate support, an ideal case for the manufacturing of electronic or other such devices from graphene. Whilst studying the mechanical stiffness of graphene on $4H$-SiC intercalated with hydrogen we also observe several other phenomena, the first of which are irregular pockets or regions where the mechanical stiffness is greatly reduced. By observing these structures over a period of time we notice that they are not always stable and appear to change in size/shape therefore indicating that these may well be pockets of H_2 gas left over from the intercalation process. Another phenomena that we observe, and something that has been reported elsewhere in literature, is the presence of triangular depressions. We probe the frictional and mechanical properties of these where upon analysis we deduce that the depressions themselves, especially in intercalated samples, are regions where the graphene is both thinner and may be covalently bound to the substrate. We also observe that due to the weak interaction with the intercalated substrate it may be possible to lift up the graphene partially with the AFM tip. The outcome of this research on graphene grown on $4H$-SiC may provide an insight into the electrical behaviour observed elsewhere as we identify several unusual phenomena such as pockets of trapped hydrogen and triangular depression. This may help in the development of new growth procedures aimed at improving the uniformity of the sample as a whole.

We also report on electrostatic phenomena observed in graphene resonator type devices. We have observed, through the detection of the electrostatic actuation of the graphene membranes with an AFM probe, the charge trapped beneath the MLG flake. We present this as a new use of the already existing technique of direct contact electrostatic force microscopy (DC-EFM) as a way of characterising the local charges present within the vicinity of the graphene

NEMS, an important property that can adversely affect device performance. We propose that this method may be used to probe the electrostatic environment, something that is highly dependant on the temperature and humidity, beneath indeed any conductive material where the charges are effectively screened. This is provided that there is a detectable electrostatic actuation of the material by the AFM, typically above 50 pm. Finally we devise a new sub-method of AFM called electrostatic heterodyne force microscopy (E-HFM), this method draws on the heterodyne mixing principle widely used in RF electronics but also in SPM to deduce time-dependant mechanical phenomena. By mixing the mechanical vibration of the tip with an electrostatic field we are able to probe the electromechanical properties of graphene resonators with a time resolution of $\approx$1 ns. This method opens the door to mapping with a nm and ns resolution the time-dependant properties of graphene NEMS, something that has not yet been achieved to date. The described method of E-HFM was demonstrated at relatively low operating frequencies, however as devices decrease in size and increase in frequency this can be scaled up to higher frequencies (>GHz) whilst maintaining a nanometre resolution.

Going forward we now show some of the preliminary work that has been carried out in order to further develop the method of E-HFM. We also present some of research carried out into the development of a new hybrid type of device which combines h-BN resonators with surface acoustic wave devices. Here one expects to be able to probe the behaviour of Lamb waves in the ultrathin limit where we expect nanoscale phenomena such as flexoelectricity to play a role.

Appendix A

Materials and Methods

A.1 Substrate SiO_2 Etching

Throughout this thesis we have made use of Si/SiO_2 substrate with trenches of various widths etched into them. Whilst the trenches of width 300 nm were fabricated by collaborators at Durham[144] all other trenches etched into the substrate were manufactured in house through the use of reactive ion etching (RIE). All etching was performed with an Oxford Instruments PlasmaPro®NGP80. To setup the substrate for etching we used a single layer of S1813 photo resist spun at 3000-4000 rpm for a total of 30-60 seconds, this gave a thickness of approximately 1.3-1.6 μm. The resist was then baked at 115 ^{o}C for 60s. To expose the trench areas we placed the mask containing the features on the substrate and illuminated with UV light (mercury lamp at 280 W power) for 2 seconds. The resist was then developed in the developer MF-319 for a total of 45 seconds after which we baked the sample once more at 90 ^{o}C for 90 s.

The gas mixture for etching was CHF_3:- 35sccm and 0_2:- 15 sccm with an RF power of 80 W. The time given for the etching process can be calculated from Fig. A.1. This etch process was relatively slow but allowed for a precisely controlled thickness.

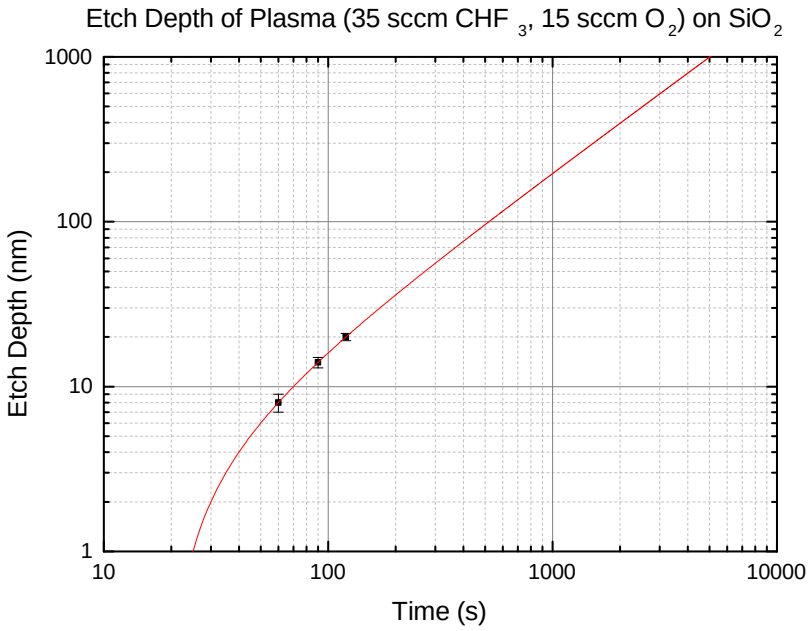

Figure A.1: The etch rate for the perscribed method of RIE

Appendix B

Nanomechanical Phenomena in 2D Materials

B.1 Growth of Graphene on SiC

The 4H-SiC samples grown for the use in this study were produced by initially heating the SiC sample at 1600^{o}C in the presence of an argon laminar flow, the pressure of which was used to determine the thickness of the graphene grown. The intercalation process was performed afterwards and separately from the growth stage. To intercalate with hydrogen samples were heated to temperatures between 1100-1200^{o}C in an H_2 environment at a pressure of 900 mbar, the samples were then cooled whilst maintaining a hydrogen atmosphere to prevent the deintercalation of the substrate.

B.2 Piezo Calibration for Differential UFM

As the amplitude of the piezoelectric transducer can vary measurably over the distance of tens of μm[99] it is difficult to calibrate this amplitude accurately using methods such as laser vibrometry where the precise location of the sample has to be found and measured every time a measurement is made. One solution

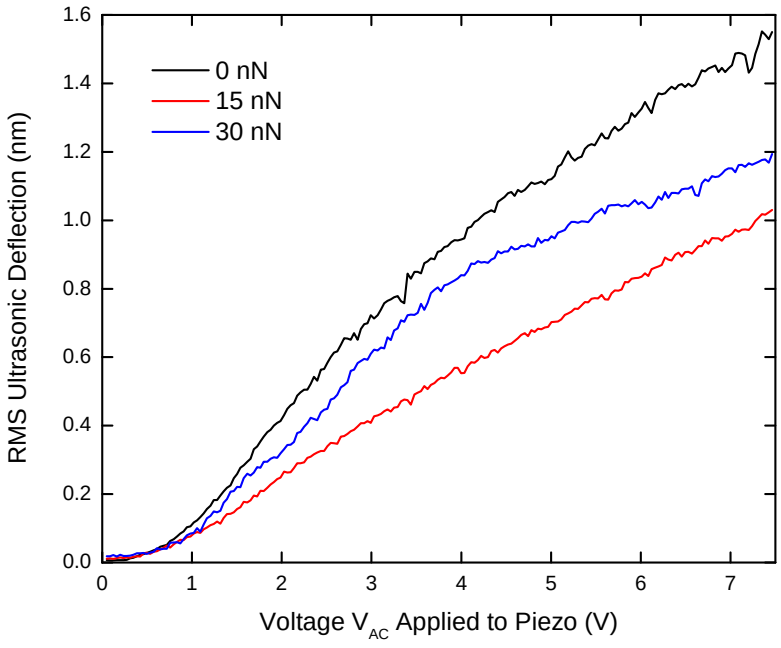

Figure B.1: The piezo calibration curves for one location on the as-grown sample for set forces of 0 nN (black), 15 nN (red) and 30 nN (blue). The rms ultrasonic vibration is shown as a function of the amplitude of the voltage applied to the piezo.

to this was proposed[100] whereby the amplitude of vibration is increased well beyond the point at which the ultrasonic deflection is observed. The principle by which one can calculate the piezo amplitude is that in the high amplitude regime an increase in the piezo amplitude will result in an equal change in the ultrasonic deflection, the ultrasonic deflection (measured as the rms voltage from the lockin amplifier) can then be calculated if the deflection constant of the cantilever is known. To perform this calibration we used a LabView program to sweep the piezo drive amplitude whilst measuring the lockin amplifier response, the results of such a sweep can be seen in Fig's. B.1 and B.2.

Here we observe that as the applied voltage to the piezo increases the UFM response or amplitude plateaus. The slope of this line is to be taken as the constant associated with the piezo at this particular point. As one can see these

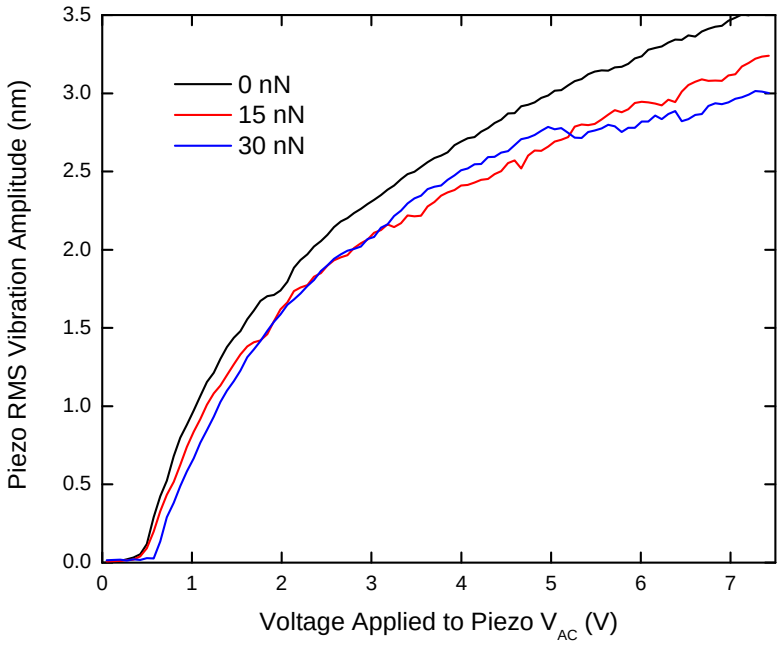

Figure B.2: The piezo calibration curves for one location on a Si_3N_4 sample for set forces of 0 nN (black), 15 nN (red) and 30 nN (blue). The rms ultrasonic vibration is shown as a function of the amplitude of the voltage applied to the piezo.

curves are not always in agreement with each other as we show the UFM response at several set forces. The voltages at which we drive the piezos are perhaps in the region at which there are additional non-linear effects from the PZT material. It is clear that this method does produce exact results however the variation is minimal and it is, to a good approximation valid.

Appendix C

Nanoelectromechanical Phenomena

C.1 Electronic Detection of the Differential Interferometer Signal

As the interferometer used in section 6.3 is to be used for the high frequency detection of graphene and other 2D materials resonators we need to employ suitably fast electronic detection systems. In the detection of light we employ a split-segment photodiode with a response time of 13 ns under a 10 V reverse bias, this was adequate to detect at frequencies up to approximately 75 MHz. To detect the resulting photo current an instrumental amplifier, seen in Fig. A was used.

C.2 Alignment in Differential interferometer

To be able to align the sample with the two laser spots in the differential interferometer with sub-μm precision we employ an additional beam splitter along with a CCD camera. To implement this we employ a band-pass filter to remove

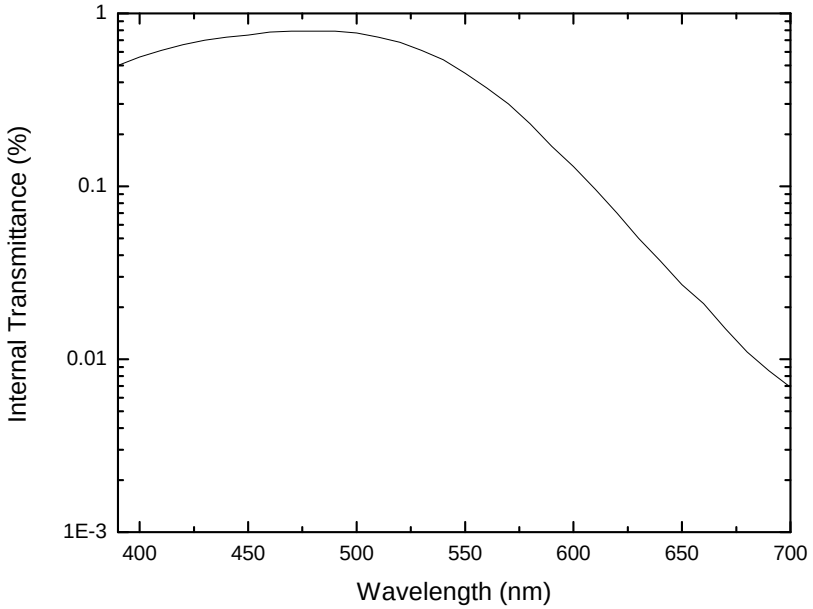

Figure C.1: Internal transmittance characteristics of the filter used in front of the CCD system.

a large portion of the laser light, without this the image on the CCD would be saturated. In addition to this the filter prevents any light from the illumination from affecting the system. The filter manufactured by Schott has the following characteristics for a reference of 1 mm thickness, the component used in these studies was however of 3 mm thickness.

Once the laser light was reduced in intensity so that it did not oversaturate the image on the CMOS camera it was possible to view the sample. As the image viewed by the camera was seen through WP1 and illuminated with unpolarised light two images could be seen on the screen of different areas of the sample. Assuming the system had been properly aligned such that both laser beams perfectly recombined upon passing through the WP1 a second time the image seen by the camera would be of one bright spot corresponding to the recombined laser beam and two images overlapped as seen in Fig. C.2

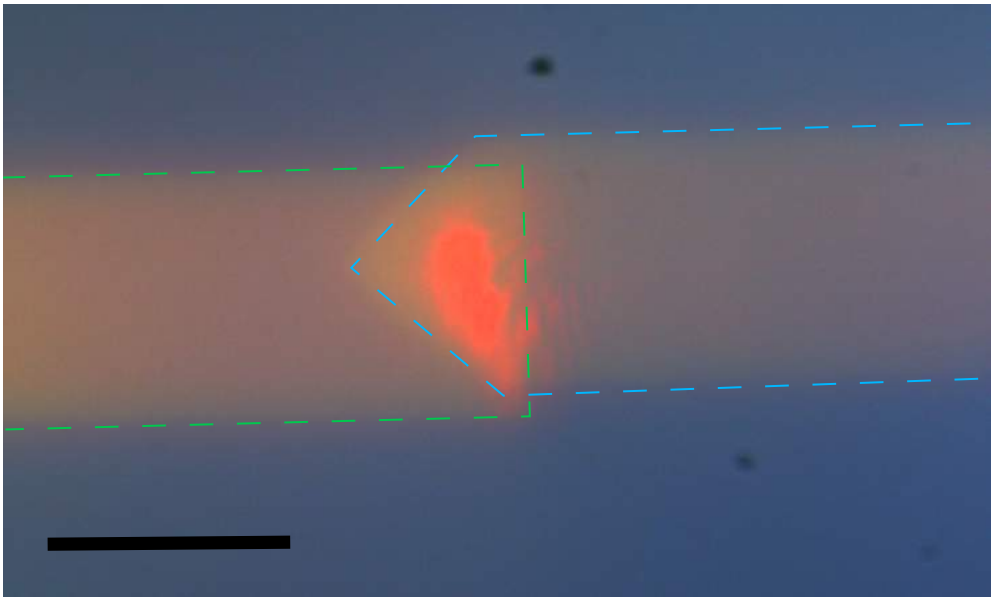

Figure C.2: Image seen at the camera (scale bar 50 μm)in the interferometer where light from both polarisations recombine and overlap. The recombined laser beam can be seen in the centre of the image where it corresponds to different positions on either image; at the base of the cantilever for one image (outlined in dotted green line) and at the tip of the cantilever for the other image (outlined in blue).

Publications

[1] Del Pozo-Zamudio O, Schwarz S, Sich M, Akimov I, Bayer M, Schofield R, et al. Photoluminescence of two-dimensional GaTe and GaSe films. 2D Materials. 2015;2(3):035010.

[2] Dinelli F, Pingue P, Kay ND, Kolosov OV. Subsurface Imaging of Two-Dimensional Materials on the Nanoscale;. Submitted to NanoLetters (09/09/2016).

[3] Kay ND, Robinson BJ, Falko VI, Novoselov KS, Kolosov OV. Electromechanical sensing of substrate charge hidden under atomic 2D crystals. Nano letters. 2014;14(6):3400–3404. 94, 98

[4] Kay ND, Tovee PD, Robinson BJ, Novoselov KS, Kolosov OV. Nanoscale Mapping of Nanosecond Time-scale Electro-Mechanical Phenomena in Graphene NEMS. arXiv preprint arXiv:150900804. 2015;.

[5] Robinson BJ, Giusca CE, Gonzalez YT, Kay ND, Kazakova O, Kolosov OV. Structural, optical and electrostatic properties of single and few-layers MoS2: effect of substrate. 2D Materials. 2015;2(1):015005.

[6] Robinson BJ, Kay ND, Kolosov OV. Nanoscale interfacial interactions of graphene with polar and nonpolar liquids. Langmuir. 2013;29(25):7735–7742. 56, 99

Talks & Presentations

[1] Conference LUFC. Sensing Substrate Charge Beneath 2D Crystals; 2014. .

[2] Graphene, 2D Materials U NPL. Subsurface Imaging of 2D Materials on the Nanoscale; 2014. .

[3] JSAP-MRS Conference J Kyoto. Ultrasonic Force Microscopy (UFM), Heterodyne Force Microscopy (HFM) and Force Modulation Microscopy (FMM) Studies of 2D Materials; 2013. .

[4] MRS Fall Meeting U Boston. How Deep Ultrasonic and Heterodyne Force Microscopies Can Look at the Nanostructure of 2D Materials; 2014. .

Conference Proceedings

[1] Kay N, Robinson B, Novoselov K, Kolosov O. Time-dependant electrostatic and electro-mechanical phenomena in Graphene NEMS. Graphene Week 2015. 2015;.

[2] Kolosov O, Kay N, Dinelli F, Pingue P. How Deep Ultrasonic and Heterodyne Force Microscopies Can Look at the Nanostructure of 2D Materials? In: MRS 2014 Fall Meeting; 2014. .

[3] Kolosov O, Kay N, Dinelli F, Robinson B, Falko V, Pingue P. Exploring buried interfaces and nanoelectromechanical devices in 2D materials–effects of elastic anisotropy. Graphene Week 2015. 2015;.

[4] Kolosov O, Kay N, Robinson B, Rosamond MC, Zeze DA, Falko V, et al. Mapping nanomechanical phenomena in graphene nanostructures using force modulation and ultrasonic force microscopy. 2012;.

[5] Robinson B, Kay N, Kolosov O. Adhesion and dynamic nanotribology of graphene in polar and non-polar liquid environments studied with ultrasonic force microscopy. 2012;.

[6] Robinson B, Kay N, Mazzocco R, Kolosov O. Nanomechanics and interfacial properties of supported and suspended graphene layers. NanoteC13 Carbon Nanoscience and Nanotechnology. 2013;.

[7] Robinson B, Kay N, Rosamond MC, Zeze DA, Dinelli F, Kolosov O. Ambient and underliquid nanomechanical properties of suspended and supported graphene at wide range of range of stiffnesses. Seeing at the Nanoscale 2012. 2012;.

References

[1] Landau L. Zur Theorie der phasenumwandlungen II. Phys Z Sowjetunion. 1937;11:26–35. 1

[2] Bernal J. The structure of graphite. Proceedings of the Royal Society of London Series A, Containing Papers of a Mathematical and Physical Character. 1924;106(740):749–773. 1

[3] Lennard-Jones J. Discussion on graphite. Trans Faraday Soc. 1934;30:58. 1

[4] Verble J, Wietling T, Reed P. Rigid-layer lattice vibrations and van der waals bonding in hexagonal MoS2. Solid State Communications. 1972;11(8):941–944. 1

[5] Novoselov KS, Geim AK, Morozov SV, Jiang D, Zhang Y, Dubonos SV, et al. Electric field effect in atomically thin carbon films. science. 2004;306(5696):666–669. 1, 10

[6] Hunt B, Sanchez-Yamagishi J, Young A, Yankowitz M, LeRoy BJ, Watanabe K, et al. Massive Dirac fermions and Hofstadter butterfly in a van der Waals heterostructure. Science. 2013;340(6139):1427–1430. 2

[7] Ponomarenko L, Gorbachev R, Yu G, Elias D, Jalil R, Patel A, et al. Cloning of Dirac fermions in graphene superlattices. Nature. 2013;497(7451):594–597. 2

[8] Britnell L, Gorbachev R, Geim A, Ponomarenko L, Mishchenko A, Greenaway M, et al. Resonant tunnelling and negative differential conductance in graphene transistors. Nature communications. 2013;4:1794. 2

[9] Ponomarenko L, Geim A, Zhukov A, Jalil R, Morozov S, Novoselov K, et al. Tunable metal-insulator transition in double-layer graphene heterostructures. Nature Physics. 2011;7(12):958–961. 2

[10] Obraztsov AN. Chemical vapour deposition: making graphene on a large scale. Nature nanotechnology. 2009;4(4):212–213. 2

[11] Wang M, Jang SK, Jang WJ, Kim M, Park SY, Kim SW, et al. A Platform for Large-Scale Graphene Electronics–CVD Growth of Single-Layer Graphene on CVD-Grown Hexagonal Boron Nitride. Advanced Materials. 2013;25(19):2746–2752. 2

[12] Emtsev K, Speck F, Seyller T, Ley L, Riley JD. Interaction, growth, and ordering of epitaxial graphene on SiC {0001} surfaces: A comparative photoelectron spectroscopy study. Physical Review B. 2008;77(15):155303. 2

[13] Riedl C, Coletti C, Starke U. Structural and electronic properties of epitaxial graphene on SiC (0 0 0 1): a review of growth, characterization, transfer doping and hydrogen intercalation. Journal of Physics D: Applied Physics. 2010;43(37):374009. 2, 75

[14] Withers F, Del Pozo-Zamudio O, Mishchenko A, Rooney A, Gholinia A, Watanabe K, et al. Light-emitting diodes by band-structure engineering in van der Waals heterostructures. Nature materials. 2015;14(3):301–306. 3

[15] Yamanaka K, Ogiso H, Kolosov O. Ultrasonic force microscopy for nanometer resolution subsurface imaging. Applied Physics Letters. 1994;64(2):178–180. 3, 30

[16] Striegler A, Pathuri N, Köhler B, Bendjus B. Visibility of Buried Structures in Atomic Force Acoustic Microscopy. In: Review of Progress in Quantitative Nondestructive Evaluation. vol. 894. AIP Publishing; 2007. p. 1572–1576. 3

[17] Kolosov O, Grishin I, Jones R. Material sensitive scanning probe microscopy of subsurface semiconductor nanostructures via beam exit Ar ion polishing. Nanotechnology. 2011;22(18):185702. 3

[18] Lee C, Wei X, Kysar JW, Hone J. Measurement of the elastic properties and intrinsic strength of monolayer graphene. science. 2008;321(5887):385–388. 3, 9

[19] Ekinci K, Huang X, Roukes M. Ultrasensitive nanoelectromechanical mass detection. Applied Physics Letters. 2004;84(22):4469–4471. 4

[20] Lee HL, Yang YC, Chang WJ. Mass detection using a graphene-based nanomechanical resonator. Japanese Journal of Applied Physics. 2013;52(2R):025101. 4

[21] Garcia-Sanchez D, van der Zande AM, Paulo AS, Lassagne B, McEuen PL, Bachtold A. Imaging mechanical vibrations in suspended graphene sheets. Nano letters. 2008;8(5):1399–1403. 4, 26, 27

[22] Rivas M, Vyas V, Carter A, Veronick J, Khan Y, Kolosov OV, et al. Nanoscale mapping of in situ actuating microelectromechanical systems with AFM. Journal of Materials Research. 2015;30(03):429–441. 4, 27

[23] Cuberes MT, Assender H, Briggs GAD, Kolosov O. Heterodyne force microscopy of PMMA/rubber nanocomposites: nanomapping of viscoelastic response at ultrasonic frequencies. Journal of Physics D: Applied Physics. 2000;33(19):2347. 4, 38, 39, 104, 105

[24] Bunch JS, Van Der Zande AM, Verbridge SS, Frank IW, Tanenbaum DM, Parpia JM, et al. Electromechanical resonators from graphene sheets. Science. 2007;315(5811):490–493. 5, 18, 20, 25

[25] Cole RM, Brawley GA, Adiga VP, De Alba R, Parpia JM, Ilic B, et al. Evanescent-Field Optical Readout of Graphene Mechanical Motion at Room Temperature. Phys Rev Applied. 2015 Feb;3:024004. Available from: http://link.aps.org/doi/10.1103/PhysRevApplied.3.024004. 5, 25

[26] Denboef AJ. Scanning force microscopy using optical interferometry. 1991;. 5, 112, 113

[27] Li C, Chou TW. A structural mechanics approach for the analysis of carbon nanotubes. International Journal of Solids and Structures. 2003;40(10):2487–2499. 9

[28] Van Lier G, Van Alsenoy C, Van Doren V, Geerlings P. Ab initio study of the elastic properties of single-walled carbon nanotubes and graphene. Chemical Physics Letters. 2000;326(1):181–185. 9

[29] Reddy C, Rajendran S, Liew K. Equivalent continuum modeling of graphene sheets. International Journal of Nanoscience. 2005;4(04):631–636. 9

[30] Lee JU, Yoon D, Cheong H. Estimation of Youngs modulus of graphene by Raman spectroscopy. Nano letters. 2012;12(9):4444–4448. 9

[31] Blakslee O, Proctor D, Seldin E, Spence G, Weng T. Elastic constants of compression-annealed pyrolytic graphite. Journal of Applied Physics. 1970;41(8):3373–3382. 9

[32] Frank I, Tanenbaum DM, Van der Zande A, McEuen PL. Mechanical properties of suspended graphene sheets. Journal of Vacuum Science & Technology B. 2007;25(6):2558–2561. 9

[33] Zhao S, Xue J. Mechanical properties of hybrid graphene and hexagonal boron nitride sheets as revealed by molecular dynamic simulations. Journal of Physics D: Applied Physics. 2013;46(13):135303. 9, 11

[34] Liu F, Ming P, Li J. Ab initio calculation of ideal strength and phonon instability of graphene under tension. Physical Review B. 2007;76(6):064120. 9

[35] Nair RR, Blake P, Grigorenko AN, Novoselov KS, Booth TJ, Stauber T, et al. Fine structure constant defines visual transparency of graphene. Science. 2008;320(5881):1308–1308. 9

[36] Zhu SE, Yuan S, Janssen G. Optical transmittance of multilayer graphene. EPL (Europhysics Letters). 2014;108(1):17007. 9

[37] Bao Q, Zhang H, Ni Z, Wang Y, Polavarapu L, Shen Z, et al. Monolayer graphene as a saturable absorber in a mode-locked laser. Nano Research. 2011;4(3):297–307. 9

[38] Miller JM. Optimizing and Applying Graphene as a Saturable Absorber for Generating Ultrashort Pulses. 2011;. 9

[39] Weber J, Calado V, Van de Sanden M. Optical constants of graphene measured by spectroscopic ellipsometry. Applied Physics Letters, 97 (9), 2010. 2010;. 10, 16

[40] Wang WE, Balooch M, Claypool C, Zawaideh M, Farnaam K. Combined reflectometry-ellipsometry technique to measure graphite down to monolayer thickness. Solid State Technology. 2009;52(6):18–22. 10

[41] Liu L, Feng Y, Shen Z. Structural and electronic properties of h-BN. Physical Review B. 2003;68(10):104102. 10

[42] Pauling L. The structure and properties of graphite and boron nitride. Proceedings of the National Academy of Sciences. 1966;56(6):1646–1652. 10

[43] Pease RS. An X-ray study of boron nitride. Acta Crystallographica. 1952;5(3):356–361. 11, 127

[44] Bosak A, Serrano J, Krisch M, Watanabe K, Taniguchi T, Kanda H. Elasticity of hexagonal boron nitride: Inelastic x-ray scattering measurements. Physical Review B. 2006;73(4):041402. 11, 66

[45] Woo S, Park HC, Son YW. Poisson's ratio in layered two-dimensional crystals. Physical Review B. 2016;93(7):075420. 11, 12, 14, 66

[46] Cho J, Luo J, Daniel I. Mechanical characterization of graphite/epoxy nanocomposites by multi-scale analysis. Composites science and technology. 2007;67(11):2399–2407. 11, 19, 20, 66

[47] Wu J, Wang B, Wei Y, Yang R, Dresselhaus M. Mechanics and Mechanically Tunable Band Gap in Single-Layer Hexagonal Boron-Nitride. Materials Research Letters. 2013;1(4):200–206. 11

[48] Cassabois G, Valvin P, Gil B. Hexagonal boron nitride is an indirect bandgap semiconductor. Nature Photonics. 2016;. 12

[49] Dean CR, Young AF, Meric I, Lee C, Wang L, Sorgenfrei S, et al. Boron nitride substrates for high-quality graphene electronics. Nature nanotechnology. 2010;5(10):722–726. 12, 52

[50] Lee J, Wang Z, He K, Shan J, Feng PXL. High frequency MoS2 nanomechanical resonators. ACS nano. 2013;7(7):6086–6091. 12, 25

[51] Avsar A, Vera-Marun IJ, Tan JY, Watanabe K, Taniguchi T, Castro Neto AH, et al. Air-stable transport in graphene-contacted, fully encapsulated ultrathin black phosphorus-based field-effect transistors. ACS nano. 2015;9(4):4138–4145. 12, 48

[52] Gorbachev RV, Riaz I, Nair RR, Jalil R, Britnell L, Belle BD, et al. Hunting for monolayer boron nitride: optical and Raman signatures. Small. 2011;7(4):465–468. 12

[53] Gatesman A, Giles R, Waldman J. Submillimeter optical properties of hexagonal boron nitride. Journal of applied physics. 1993;73(8):3962–3966. 12

[54] Beiranvand R, Valedbagi S. Electronic and optical properties of h-BN nanosheet: a first principles calculation. Diamond and Related Materials. 2015;58:190–195. 12

[55] Stenzel O, Hahn J, Röder M, Ehrlich A, Prause S, Richter F. The optical constants of cubic and hexagonal boron nitride thin films and their relation to the bulk optical constants. Physica status solidi A Applied research. 1996;158(1):281–287. 12

[56] Godfrey D, Nelson EC. Oxidation Characteristics of Molybdenum Disulfide and Effect of Such Oxidation on Its Role as a Solid-Film Lubricant. 1949;. 12

[57] Kappera R, Voiry D, Yalcin SE, Branch B, Gupta G, Mohite AD, et al. Phase-engineered low-resistance contacts for ultrathin MoS2 transistors. Nature materials. 2014;13(12):1128–1134. 13

[58] Castellanos-Gomez A, Poot M, Steele GA, van der Zant HS, Agraït N, Rubio-Bollinger G. Elastic properties of freely suspended MoS2 nanosheets. Advanced Materials. 2012;24(6):772–775. 13, 66

[59] Bertolazzi S, Brivio J, Kis A. Stretching and breaking of ultrathin MoS2. ACS nano. 2011;5(12):9703–9709. 13, 14

[60] Cooper RC, Lee C, Marianetti CA, Wei X, Hone J, Kysar JW. Nonlinear elastic behavior of two-dimensional molybdenum disulfide. Physical Review B. 2013;87(3):035423. 13

[61] Jiang JW, Park HS. Mechanical properties of MoS2/graphene heterostructures. Applied Physics Letters. 2014;105(3):033108. 13

[62] Mak KF, Lee C, Hone J, Shan J, Heinz TF. Atomically thin MoS 2: a new direct-gap semiconductor. Physical Review Letters. 2010;105(13):136805. 14

[63] Parthé E, Gmelin L. Gmelin Handbook of inorganic and organometallic chemistry: TYPIX.. Standardized data and crystal chemical characterization of inorganic structure types. vol. 1. Springer; 1993. 14

[64] Castellanos-Gomez A, Agraït N, Rubio-Bollinger G. Optical identification of atomically thin dichalcogenide crystals. Applied Physics Letters. 2010;96(21):213116. 14, 15

[65] Benameur M, Radisavljevic B, Heron J, Sahoo S, Berger H, Kis A. Visibility of dichalcogenide nanolayers. Nanotechnology. 2011;22(12):125706. 15

[66] Roddaro S, Pingue P, Piazza V, Pellegrini V, Beltram F. The optical visibility of graphene: interference colors of ultrathin graphite on SiO2. Nano letters. 2007;7(9):2707–2710. 15, 43, 117

[67] Abergel D, Russell A, Fal'ko VI. Visibility of graphene flakes on a dielectric substrate. arXiv preprint arXiv:07050091. 2007;. 15, 43, 117

[68] Blake P, Hill E, Neto AC, Novoselov K, Jiang D, Yang R, et al. Making graphene visible. Applied Physics Letters. 2007;91(6):063124. 15, 43, 117

[69] Anders H. Thin films in optics. London: Focal Press, 1967. 1967;1. 15, 117, 118

[70] Polster HD. Reflection from a multilayer filter. JOSA. 1949;39(12):1038–1041. 15

[71] Schroder G. Z. angew. Phys. 1951;3:53. 15

[72] Judd DB. Basic correlates of the visual stimulus. 1951;. 16

[73] Vos JJ. Colorimetric and photometric properties of a 2 fundamental observer. Color Research & Application. 1978;3(3):125–128. 16

[74] Weaver Jr W, Timoshenko SP, Young DH. Vibration problems in engineering. John Wiley & Sons; 1990. 20

[75] Kelly BT. Physics of graphite. 1981;. 20

[76] Lee J, Wang Z, He K, Shan J, Feng PXL. Air damping of atomically thin MoS2 nanomechanical resonators. Applied Physics Letters. 2014;105(2):023104. 21, 22, 25

[77] Newell WE. Miniaturization of tuning forks. Science. 1968;161:1320–1326. 21

[78] Karabacak D, Yakhot V, Ekinci K. High-frequency nanofluidics: An experimental study using nanomechanical resonators. Physical review letters. 2007;98(25):254505. 22

[79] Bianco S, Cocuzza M, Ferrero S, Giuri E, Piacenza G, Pirri C, et al. Silicon resonant microcantilevers for absolute pressure measurement. Journal of Vacuum Science & Technology B. 2006;24(4):1803–1809. 22

[80] Svitelskiy O, Sauer V, Liu N, Cheng KM, Finley E, Freeman MR, et al. Pressurized fluid damping of nanoelectromechanical systems. Physical review letters. 2009;103(24):244501. 22

[81] Bhiladvala RB, Wang ZJ. Effect of fluids on the Q factor and resonance frequency of oscillating micrometer and nanometer scale beams. Physical review E. 2004;69(3):036307. 22

[82] Zande AMvd, Barton RA, Alden JS, Ruiz-Vargas CS, Whitney WS, Pham PH, et al. Large-scale arrays of single-layer graphene resonators. Nano letters. 2010;10(12):4869–4873. 22, 25

[83] Lu Z, Dunn ML. van der Waals adhesion of graphene membranes. Journal of Applied Physics. 2010;107(4):044301. 22

[84] Begley MR, Mackin TJ. Spherical indentation of freestanding circular thin films in the membrane regime. Journal of the Mechanics and Physics of Solids. 2004;52(9):2005–2023. 23

[85] Shivaraman S, Barton RA, Yu X, Alden J, Herman L, Chandrashekhar M, et al. Free-standing epitaxial graphene. Nano letters. 2009;9(9):3100–3105. 25

[86] Barton RA, Ilic B, Van Der Zande AM, Whitney WS, McEuen PL, Parpia JM, et al. High, size-dependent quality factor in an array of graphene mechanical resonators. Nano letters. 2011;11(3):1232–1236. 25

[87] Robinson JT, Zalalutdinov M, Baldwin JW, Snow ES, Wei Z, Sheehan P, et al. Wafer-scale reduced graphene oxide films for nanomechanical devices. Nano letters. 2008;8(10):3441–3445. 25

[88] Castellanos-Gomez A, van Leeuwen R, Buscema M, van der Zant HS, Steele GA, Venstra WJ. Single-Layer MoS2 Mechanical Resonators. Advanced Materials. 2013;25(46):6719–6723. 25

[89] Karabacak D, Kouh T, Ekinci K. Analysis of optical interferometric displacement detection in nanoelectromechanical systems. Journal of applied physics. 2005;98(12):124309. 25

[90] Witkamp B, Poot M, van der Zant HS. Bending-mode vibration of a suspended nanotube resonator. Nano letters. 2006;6(12):2904–2908. 28

[91] Sazonova V, Yaish Y, Üstünel H, Roundy D, Arias TA, McEuen PL. A tunable carbon nanotube electromechanical oscillator. Nature. 2004;431(7006):284–287. 28

[92] Chen C, Rosenblatt S, Bolotin KI, Kalb W, Kim P, Kymissis I, et al. Performance of monolayer graphene nanomechanical resonators with electrical readout. Nature nanotechnology. 2009;4(12):861–867. 28

[93] Verbiest G, Rost M. Resonance frequencies of AFM cantilevers in contact with a surface. Ultramicroscopy. 2016;171:70–76. 29, 108

[94] Maivald P, Butt H, Gould S, Prater C, Drake B, Gurley J, et al. Using force modulation to image surface elasticities with the atomic force microscope. Nanotechnology. 1991;2(2):103. 29

[95] Günther P, Fischer UC, Dransfeld K. Scanning near-field acoustic microscopy. Applied Physics B. 1989;48(1):89–92. 30

[96] Inagaki K, Kolosov O, Briggs G, Muto S, Horisaki Y, Wright O. Ultrasonic force microscopy in waveguide mode up to 100 MHz. In: Ultrasonics Symposium, 1998. Proceedings., 1998 IEEE. vol. 2. IEEE; 1998. p. 1255–1259. 30

[97] Inagaki K, Kolosov O, Briggs GAD, Wright O. Waveguide ultrasonic force microscopy at 60 MHz. Applied Physics Letters. 2000;76(14):1836–1838. 30

[98] Dinelli F, Biswas S, Briggs GAD, Kolosov O. Measurements of stiff-material compliance on the nanoscale using ultrasonic force microscopy. Physical Review B. 2000;61(20):13995. 31

[99] Bosse J, Tovee P, Huey B, Kolosov O. Physical mechanisms of megahertz vibrations and nonlinear detection in ultrasonic force and related microscopies. Journal of Applied Physics. 2014;115(14):144304. 31, 66, 137

[100] Kolosov O, Yamanaka K. Nonlinear detection of ultrasonic vibrations in an atomic force microscope. Japanese journal of applied physics. 1993;32(8A):L1095. 33, 138

[101] Hudlet S, Saint Jean M, Guthmann C, Berger J. Evaluation of the capacitive force between an atomic force microscopy tip and a metallic surface. The European Physical Journal B-Condensed Matter and Complex Systems. 1998;2(1):5–10. 34

[102] Belaidi S, Girard P, Leveque G. Electrostatic forces acting on the tip in atomic force microscopy: Modelization and comparison with analytic expressions. Journal of Applied Physics. 1997;81(3):1023–1030. 34

[103] Girard P. Electrostatic force microscopy: principles and some applications to semiconductors. Nanotechnology. 2001;12(4):485. 37

[104] Hong J, Noh K, Park Si, Kwun S, Khim Z. Surface charge density and evolution of domain structure in triglycine sulfate determined by electrostatic-force microscopy. Physical Review B. 1998;58(8):5078. 38, 94

[105] Hong J, Park Si, Khim Z. Measurement of hardness, surface potential, and charge distribution with dynamic contact mode electrostatic force microscope. Review of Scientific Instruments. 1999;70(3):1735–1739. 38, 94, 101, 121

[106] Verbiest G, Rost M. Beating beats mixing in heterodyne detection schemes. Nature communications. 2015;6. 41, 104

[107] Verbiest G, Simon J, Oosterkamp T, Rost M. Subsurface atomic force microscopy: towards a quantitative understanding. Nanotechnology. 2012;23(14):145704. 41

[108] Verbiest G, Oosterkamp T, Rost M. Contrast Mechanism in Heterodyne Force Microscopy: Friction at Shaking Nanoparticles; 2013. 41, 104

[109] Bridges G, Said R, Mittal M, Thomson D. Sampled waveform measurement in integrated circuits using heterodyne electrostatic force microscopy. Review of scientific instruments. 1994;65(11):3378–3381. 41, 42, 106

[110] Yokoyama H, Jeffery MJ, Inoue T. Heterodyne force-detection for high frequency local dielectric spectroscopy by scanning Maxwell stress microscopy. Japanese journal of applied physics. 1993;32(12B):L1845. 41, 42

[111] Kang YJ, Kang J, Chang KJ. Electronic structure of graphene and doping effect on SiO_2. Phys Rev B. 2008 Sep;78:115404. Available from: `http://link.aps.org/doi/10.1103/PhysRevB.78.115404`. 43

[112] Rudenko AN, Keil FJ, Katsnelson MI, Lichtenstein AI. Interfacial interactions between local defects in amorphous SiO_2 and supported graphene. Phys Rev B. 2011 Aug;84:085438. Available from: `http://link.aps.org/doi/10.1103/PhysRevB.84.085438`. 43

[113] Ryu S, Liu L, Berciaud S, Yu YJ, Liu H, Kim P, et al. Atmospheric oxygen binding and hole doping in deformed graphene on a SiO2 substrate. Nano letters. 2010;10(12):4944–4951. 43

[114] Yang Y, Murali R. Binding mechanisms of molecular oxygen and moisture to graphene. Applied Physics Letters. 2011;98(9). Available from: `http://scitation.aip.org/content/aip/journal/apl/98/9/10.1063/1.3562317`. 44

[115] Castellanos-Gomez A, Buscema M, Molenaar R, Singh V, Janssen L, van der Zant HS, et al. Deterministic transfer of two-dimensional materials by all-dry viscoelastic stamping. 2D Materials. 2014;1(1):011002. 44

[116] Goossens A, Calado V, Barreiro A, Watanabe K, Taniguchi T, Vandersypen L. Mechanical cleaning of graphene. Applied Physics Letters. 2012;100(7):073110. 46

[117] Ataca C, Sahin H, Ciraci S. Stable, single-layer MX2 transition-metal oxides and dichalcogenides in a honeycomb-like structure. The Journal of Physical Chemistry C. 2012;116(16):8983–8999. 46

[118] Lee CH, Silva EC, Calderin L, Nguyen MAT, Hollander MJ, Bersch B, et al. Tungsten Ditelluride: a layered semimetal. Scientific reports. 2015;5. 48

[119] Yang R, Zheng X, Wang Z, Miller CJ, Feng PXL. Multilayer MoS2 transistors enabled by a facile dry-transfer technique and thermal annealing. Journal of Vacuum Science & Technology B. 2014;32(6):061203. 48

[120] Chen Y, Zou J, Campbell SJ, Le Caer G. Boron nitride nanotubes: pronounced resistance to oxidation. Applied physics letters. 2004;84(13):2430–2432. 48

[121] Tsang S, Harris P, Green M, et al. Thinning and opening of carbon nanotubes by oxidation using carbon dioxide. NATURE-LONDON-. 1993;362:520–520. 48

[122] Ajayan P, Ebbesen T, Ichihashi T, Iijima S, Tanigaki K, Hiura H. Opening carbon nanotubes with oxygen and implications for filling. Nature. 1993;362(6420):522–525. 48

[123] Liu L, Ryu S, Tomasik MR, Stolyarova E, Jung N, Hybertsen MS, et al. Graphene oxidation: thickness-dependent etching and strong chemical doping. Nano letters. 2008;8(7):1965–1970. 48

[124] Nan HY, Ni ZH, Wang J, Zafar Z, Shi ZX, Wang YY. The thermal stability of graphene in air investigated by Raman spectroscopy. Journal of Raman Spectroscopy. 2013;44(7):1018–1021. 48

[125] Liu Z, Gong Y, Zhou W, Ma L, Yu J, Idrobo JC, et al. Ultrathin high-temperature oxidation-resistant coatings of hexagonal boron nitride. Nature communications. 2013;4. 48

[126] El-Barbary A, Telling R, Ewels C, Heggie M, Briddon P. Structure and energetics of the vacancy in graphite. Physical Review B. 2003;68(14):144107. 48

[127] Castellanos-Gomez A, Vicarelli L, Prada E, Island JO, Narasimha-Acharya K, Blanter SI, et al. Isolation and characterization of few-layer black phosphorus. 2D Materials. 2014;1(2):025001. 48

[128] Mayorov AS, Gorbachev RV, Morozov SV, Britnell L, Jalil R, Ponomarenko LA, et al. Micrometer-scale ballistic transport in encapsulated graphene at room temperature. Nano letters. 2011;11(6):2396–2399. 48

[129] Kim KK, Hsu A, Jia X, Kim SM, Shi Y, Dresselhaus M, et al. Synthesis and characterization of hexagonal boron nitride film as a dielectric layer for graphene devices. ACS nano. 2012;6(10):8583–8590. 53

[130] Lee GH, Yu YJ, Cui X, Petrone N, Lee CH, Choi MS, et al. Flexible and transparent MoS2 field-effect transistors on hexagonal boron nitride-graphene heterostructures. ACS nano. 2013;7(9):7931–7936. 53

[131] Britnell L, Gorbachev RV, Jalil R, Belle BD, Schedin F, Katsnelson MI, et al. Electron tunneling through ultrathin boron nitride crystalline barriers. Nano letters. 2012;12(3):1707–1710. 53

[132] Britnell L, Gorbachev R, Jalil R, Belle B, Schedin F, Mishchenko A, et al. Field-effect tunneling transistor based on vertical graphene heterostructures. Science. 2012;335(6071):947–950. 53

[133] Woods C, Britnell L, Eckmann A, Ma R, Lu J, Guo H, et al. Commensurate-incommensurate transition in graphene on hexagonal boron nitride. Nature physics. 2014;10(6):451–456. 53, 55, 56, 58, 60

[134] Yankowitz M, Xue J, Cormode D, Sanchez-Yamagishi JD, Watanabe K, Taniguchi T, et al. Emergence of superlattice Dirac points in graphene on hexagonal boron nitride. Nature Physics. 2012;8(5):382–386. 55

[135] Xue J, Sanchez-Yamagishi J, Bulmash D, Jacquod P, Deshpande A, Watanabe K, et al. Scanning tunnelling microscopy and spectroscopy of ultra-flat graphene on hexagonal boron nitride. Nature materials. 2011;10(4):282–285. 55

[136] Robinson BJ, Kay ND, Kolosov OV. Nanoscale interfacial interactions of graphene with polar and nonpolar liquids. Langmuir. 2013;29(25):7735–7742. 56, 99

[137] Sachs B, Wehling T, Katsnelson M, Lichtenstein A. Adhesion and electronic structure of graphene on hexagonal boron nitride substrates. Physical Review B. 2011;84(19):195414. 58, 60

[138] Blakemore J. Semiconducting and other major properties of gallium arsenide. Journal of Applied Physics. 1982;53(10):R123–R181. 62

[139] Korneev VA, Johnson LR. Scattering ofP andS waves by a spherically symmetric inclusion. Pure and applied geophysics. 1996;147(4):675–718. 63

[140] Korneev VA, Johnson LR. Scattering of elastic waves by a spherical inclusionI. Theory and numerical results. Geophysical Journal International. 1993;115(1):230–250. 63

[141] Dahan M, Zarka J. Elastic contact between a sphere and a semi infinite transversely isotropic body. International Journal of Solids and Structures. 1977;13(3):229–238. 64

[142] Liu K, Yan Q, Chen M, Fan W, Sun Y, Suh J, et al. Elastic properties of chemical-vapor-deposited monolayer MoS2, WS2, and their bilayer heterostructures. Nano letters. 2014;14(9):5097–5103. 66

[143] Feldman J. Elastic constants of 2H-MoS 2 and 2H-NbSe 2 extracted from measured dispersion curves and linear compressibilities. Journal of Physics and Chemistry of Solids. 1976;37(12):1141–1144. 66

[144] Rosamond MC, Gallant AJ, Petty MC, Kolosov O, Zeze DA. A versatile nanopatterning technique based on controlled undercutting and liftoff. Advanced Materials. 2011;23(43):5039–5044. 70, 135

[145] Riedl C, Coletti C, Iwasaki T, Zakharov A, Starke U. Quasi-free-standing epitaxial graphene on SiC obtained by hydrogen intercalation. Physical review letters. 2009;103(24):246804. 75

[146] Watcharinyanon S, Virojanadara C, Osiecki J, Zakharov A, Yakimova R, Uhrberg R, et al. Hydrogen intercalation of graphene grown on 6H-SiC (0001). Surface Science. 2011;605(17):1662–1668. 75

[147] Guisinger NP, Rutter GM, Crain JN, First PN, Stroscio JA. Exposure of epitaxial graphene on SiC (0001) to atomic hydrogen. Nano letters. 2009;9(4):1462–1466. 75

[148] Melios C, Panchal V, Giusca CE, Strupiński W, Silva SRP, Kazakova O. Carrier type inversion in quasi-free standing graphene: studies of local electronic and structural properties. Scientific reports. 2015;5. 75

[149] Hass JR. Structural characterization of epitaxial graphene on silicon carbide. Georgia Institute of Technology; 2008. 76

[150] Melios C, Spencer S, Shard A, Strupiński W, Silva S, Kazakova O. Surface and interface structure of quasi-free standing graphene on SiC. 2D Materials. 2016;3(2):025023. 76

[151] Dinelli F, Biswas S, Briggs G, Kolosov O. Ultrasound induced lubricity in microscopic contact. Applied Physics Letters. 1997;71(9):1177–1179. 89

[152] Tu Q, Lange B, Parlak Z, Lopes JMJ, Blum V, Zauscher S. Quantitative Subsurface Atomic Structure Fingerprint for 2D Materials and Heterostructures by First-Principles Calibrated Contact-Resonance Atomic Force Microscopy. ACS nano. 2016;. 92

[153] Kay ND, Robinson BJ, Falko VI, Novoselov KS, Kolosov OV. Electromechanical sensing of substrate charge hidden under atomic 2D crystals. Nano letters. 2014;14(6):3400–3404. 94, 98

[154] Bonnell DA. Scanning tunneling microscopy and spectroscopy: theory, techniques, and applications. VCH New York; 1993. 98

[155] Gere J, Gere JM, Goodno BJ. Mechanics of materials. Nelson Education; 2012. 99

[156] Troyon M, Wang Z, Pastre D, Lei H, Hazotte A. Force modulation microscopy for the study of stiff materials. Nanotechnology. 1997;8(4):163. 99

[157] Bartzsch H, Glöß D, Frach P, Gittner M, Schultheiß E, Brode W, et al. Electrical insulation properties of sputter-deposited SiO2, Si3N4 and Al2O3 films at room temperature and 400 C. physica status solidi (a). 2009;206(3):514–519. 103

[158] Tipler PA, Llewellyn R. Modern physics. Macmillan; 2003. 103

[159] Tetard L, Passian A, Thundat T. New modes for subsurface atomic force microscopy through nanomechanical coupling. Nature Nanotechnology. 2010;5(2):105–109. 104

[160] Schönenberger C, Alvarado S. A differential interferometer for force microscopy. Review of Scientific Instruments. 1989;60(10):3131–3134. 112

[161] Paolino P, Sandoval FAA, Bellon L. Quadrature phase interferometer for high resolution force spectroscopy. Review of Scientific Instruments. 2013;84(9):095001. 112, 113

[162] Cuberes MT, Assender H, Briggs GAD, Kolosov O. Heterodyne force microscopy of PMMA/rubber nanocomposites: nanomapping of viscoelastic response at ultrasonic frequencies. Journal of Physics D: Applied Physics. 2000;33(19):2347. 121

[163] Kar-Roy A, Tsai CS. Low-sidelobe weighted-coupled integrated acoustooptic tunable filter using focused surface acoustic waves. IEEE photonics technology letters. 1992;4(10):1132–1135. 124

[164] Wu TT, Tang HT, Chen YY, Liu PL. Analysis and design of focused interdigital transducers. IEEE transactions on ultrasonics, ferroelectrics, and frequency control. 2005;52(8):1384–1392. 124

[165] Kovacs G, Anhorn M, Engan H, Visintini G, Ruppel C. Improved material constants for LiNbO 3 and LiTaO 3. In: Ultrasonics Symposium, 1990. Proceedings., IEEE 1990. IEEE; 1990. p. 435–438. 124

[166] Tagantsev A. Piezoelectricity and flexoelectricity in crystalline dielectrics. Physical Review B. 1986;34(8):5883. 125

[167] Prost J, Marcerou J. On the microscopic interpretation of flexoelectricity. Journal de Physique. 1977;38(3):315–324. 125

[168] Duerloo KAN, Ong MT, Reed EJ. Intrinsic piezoelectricity in two-dimensional materials. The Journal of Physical Chemistry Letters. 2012;3(19):2871–2876. 127

[169] Liu H, Yang J. Lamb waves in double-layered nanoplates. Journal of Applied Physics. 2012;111(11):113525. 127